Land surface modelling and Earth Observation of land/atmosphere interactions in African savannahs

Thesis submitted to the University of Leicester for the degree of Doctor of Philosophy

by

Darren John Ghent
Department of Geography

October 2010

Abstract

Land/atmosphere feedback processes play a significant role in determining climate forcing on monthly to decadal timescales. Considerable uncertainty however exists in land surface model representation of these processes. This investigation represents an innovative approach to understanding key land surface processes in African savannahs in the framework of the UK's most important land surface model – the Joint UK Land Environment Simulator (JULES).

Findings from an investigation into the carbon balance of Africa for a 25-year period from 1982 to 2006 inclusive show that JULES estimated Africa to behave as a carbon sink for most of the 1980's and 1990's punctuated by three periods as a carbon source, which coincided with the three strongest El Niño events of the period. From 2002 until 2006 the continent was also estimated to be a source of carbon. Overall, the JULES simulation suggests a weakening of the African terrestrial carbon sink during this period primarily caused by hot and dry conditions in savannahs.

Applying the model further, land surface temperature (LST) displayed large uncertainty with respect to savannah field measurements from Kruger National Park, South Africa, and JULES systematically underestimated LST with respect to Earth Observation data continent-wide. The postulation was that a reduction in the uncertainty of surface-to-atmosphere heat and water fluxes could be achieved by constraining JULES simulations with satellite-derived LST using an Ensemble Kalman Filter. Findings show statistically significant reductions in root mean square errors with data assimilation than without; for heat flux simulations when compared with Eddy Covariance measurements, and surface soil moisture when compared with derivations from microwave scatterometers. The improved representation of LST was applied to map daily fuel moisture content – one of the most important wildfire determinants - over the mixed tree/grass landscapes of Africa, whereby values were strongly correlated with field measurements acquired from three savannah locations.

Acknowledgements

I would like to express my gratitude to my three supervisors who have provided fantastic support throughout the past three years – Heiko Balzter, Jörg Kaduk and John Remedios. Since this research has been funded by the NERC Climate and Land Surface Systems Interactions Centre (CLASSIC), I would also like to acknowledge the Natural Environment Research Council for their financial support. There are many other people to thank, firstly Bob Scholes and his team at the Council for Scientific and Industrial Research (CSIR), South Africa - Sally Archibald, Alecia Nickless, Kathleen Mennell, Moses Cho and Walter Khubeka - for their logistical support during the field campaign and for providing data from the Skukuza Flux Tower. In addition, I would like to thank Agata Hoscilo and Mpho Ratschivhadelo for their assistance in the collection of field measurements; and Velley Ndlovu for providing protection in a landscape with abundant wild animals. I would also like to thank staff at Scientific Services, Kruger National Park, for their support; in particular, Navashni Govender for several years of fuel moisture content data together with metadata on the experimental burn plots, Izak Smit for the provision of the IKONOS imagery, and Sandra MacFadyen for GIS data of the Park. With regards to the processing of land surface temperature data, I wish to thank Elizabeth Good at the UK Met Office, Exeter, for advice regarding the retrieval and processing of AATSR and SEVIRI data, Tim Trent for providing assistance during the blackbody calibration experiments, and the Rutherford Appleton Laboratory, Oxford, for the loan of the thermometry. I also wish to acknowledge Phil Harris at the Centre for Ecology and Hydrology, Wallingford, for the provision of the soil albedo dataset, and Stefan Hasenauer at the Vienna University of Technology, for providing me with ERS scatterometer surface soil moisture data. Finally, a special thanks to Aimée for all her love and support throughout the duration of my research.

Contents

List of abbreviations

AATSR	Advanced along-track scanning radiometer
AIC	Akaike Information Criterion
ASTER	Advanced spaceborne thermal emission and reflection radiometer
ATSR	Along-track scanning radiometer
CAM	Crassulacean acid metabolism
CAMIC	CarboAfrica Modelling InterComparison
CO_2	Carbon dioxide
CRU	Climate research unit
DGVM	Dynamic global vegetation model
EBP	Experimental burn plot
ED	Ecosystem Demography
EKF	Extended Kalman Filter
EnKF	Ensemble Kalman Filter
ENSO	El Niño Southern Oscillation
EO	Earth Observation
ERS	European remote sensing satellite
ET	Evapotranspiration
FMC	Fuel moisture content
FOV	Field-of-view
GCM	General circulation model
GLACE	Global Land-Atmosphere Coupling Experiment
GPP	Gross primary productivity
H	Sensible heat flux

IAV	Interannual variability
IGBP	International Geosphere-Biosphere Programme
IPCC	Intergovernmental Panel on Climate Change
ISLSCP	International Satellite Land Surface Climatology Project
JULES	Joint UK Land Environment Simulator
KNP	Kruger National Park
LandSAF	Satellite Application Facility on Land Surface Analysis
LE	Latent heat flux
LST	Land surface temperature
MDI	Meteorological danger index
MEI	Multivariate ENSO Index
MODIS	Moderate resolution imaging spectroradiometer
MOSES	Met Office Surface Exchange Scheme
MSG	Meteosat Second Generation
NBP	Net biome productivity
NCEP	National Centers for Environmental Prediction
NDVI	Normalised difference vegetation index
NEP	Net ecosystem productivity
NIR	Near-infrared
NPP	Net primary productivity
PAR	Photosynthetically active radiation
PCA	Principal component analysis
PFT	Plant functional type
PRT	Platinum resistance thermometer
R_a	Autotrophic respiration

R_h	Heterotrophic respiration
RMSE	Root mean square error
R_s	Soil respiration
Rubisco	Ribulase-1,5-biphosphate carboxylase oxygenase
SANParks	South African National Parks Authority
SEVIRI	Spinning enhanced visible and infrared imager
SPITFIRE	SPread and InTensity of FIRE
SSM	Surface soil moisture
TIR	Thermal infrared
TOA	Top-of-atmosphere
TRIFFID	Top-down Representation of Interactive Foliage and Flora Including Dynamics
TRMM	Tropical Rainfall Measuring Mission
UNFCCC	United Nations Framework Convention on Climate Change
WUE	Water use efficiency

Chapter 1

Introduction

1.1. Research rationale

Currently, there is growing public and scientific concern regarding the potential impacts of climate change induced by increasing emissions of greenhouse gases. Quantifying land/climate feedbacks though is subject to great uncertainty, with inadequate representation in climate scenarios – this is motivating the development of better representations of the land surface in coupled land/climate models. However land surface models, which simulate the surface and subsurface processes of the terrestrial biosphere, show considerable uncertainty in process representation (Bombelli *et al.*, 2009). The motivation behind this research is both to better understand the limitations of these tools, and to investigate whether an improvement in the capability of a selected model to simulate key properties is feasible. This is carried out in the context of the UK's most important land surface scheme - the Joint UK Land Environment Simulator (JULES).

The purpose of this research project is to examine firstly whether JULES is comparable with other land surface models in terms of carbon fluxes; and secondly, whether the simulation of energy and water fluxes can be improved by assimilating a land surface parameter retrieved from remote sensing into the model. The result is to be tested in respect of an important fuel determinant of the fire regime; the rationale here, is that biomass burning significantly contributes to the large uncertainty regarding the terrestrial biosphere feedback, and any potential optimisation in the derivation of fuel properties is a prerequisite for reducing uncertainty (van der Werf *et al.*, 2006; Lehsten *et al.*, 2009).

Although JULES facilitates *ad hoc* model development within the UK research community, this study offers an original approach into its evaluation - in which the surface energy balance and biogeochemical cycling is assessed in the context of its primary controls and parameterisation over Africa. This involved participation in the CarboAfrica Modelling InterComparison (CAMIC) Project (Weber *et al.*, 2009), including an investigation into the drivers of variability in terrestrial carbon fluxes; with the specific findings of this contribution relating the recent trend in continental carbon fluxes. A subsequent development is carried out in which a key surface energy component is integrated into the model by way of a data assimilation scheme with the purpose of eliciting an improved representation. While the precise scheme is not novel, this is the first known instance of its application with the JULES model. Furthermore, the uniqueness of the research extends to the production of a first known mapping over Africa, using modelling techniques, of one the most important fuel characteristics of wildfires. As such, the importance of this study is reflected in the potential to reduce uncertainty in land surface modelling in two distinct ways: firstly, to improve the prediction of land/atmosphere fluxes of heat and water; and secondly, to provide a key input for current fire models to utilise in their predictions of fire dynamics and emissions.

Africa is under-represented in climate modelling research (IPCC, 2007), yet is a key component in the terrestrial carbon cycle (Williams *et al.*, 2007). Most models have been developed and parameterised for use in northern latitudes, so the research findings described in this study represent a significant contribution to the emerging literature on land/atmosphere interactions over Africa. Indeed, this investigation represents an innovative approach to understanding key land surface processes in African savannahs in the framework of an important and well established land surface model. With current

political inertia, and uncertainties in climate processes causing controversy and hindering clear conclusions, any process to reduce these uncertainties is a timely and pertinent objective.

1.2. Land/atmosphere interactions

Climate change, in response to increased greenhouse gases, alters the patterns of precipitation, temperature and humidity; affecting the growth, composition and distribution of vegetation, which itself influences climate since land surface processes regulate the land/atmosphere exchanges of heat, water, momentum and carbon. Numerous studies (Zeng *et al.*, 1999; Friedlingstein *et al.*, 2001; Los *et al.*, 2006), which began with the pioneering work of Charney *et al*. (1975) on the link between African vegetation loss and drought persistence, have illustrated how land surface properties change in response to climatic forcing, and the role land/atmosphere feedback mechanisms play in determining climate.

Vegetation change for instance, is accompanied by soil moisture change. This can lead to changes in evaporation and surface albedo, resulting in an eventual change in the precipitation regime through the soil moisture – climate feedback (Koster *et al.*, 2004; Seneviratne *et al.*, 2006; Zhang *et al.*, 2008). Indeed, soil moisture – climate feedbacks can regulate climate change, increasing our ability to predict seasonal climate; the strength and regional significance of this important feedback though remains poorly understood (Zhang *et al.*, 2008).

Soil moisture is a characteristic which demonstrates a significant memory which can persist for months, with the potential to prolong and intensify incidents of pluvial and drought conditions (Notaro, 2008). High soil moisture will support enhanced evaporation, leading to an increase in atmospheric water content and eventually rainfall (Koster *et al.*, 2004). Transition zones between dry and wet climates, where soil

moisture exerts substantial control on evaporation have been identified as regions of strong land/atmosphere coupling; hotspots include the northern United States, southern Europe, and the Sahel (Koster *et al.*, 2004; Seneviratne *et al.*, 2006). Figure 1.1 shows the land/atmosphere coupling strength from the most extensive study on soil moisture – climate feedbacks, the Global Land-Atmosphere Coupling Experiment (GLACE; Koster *et al.*, 2004).

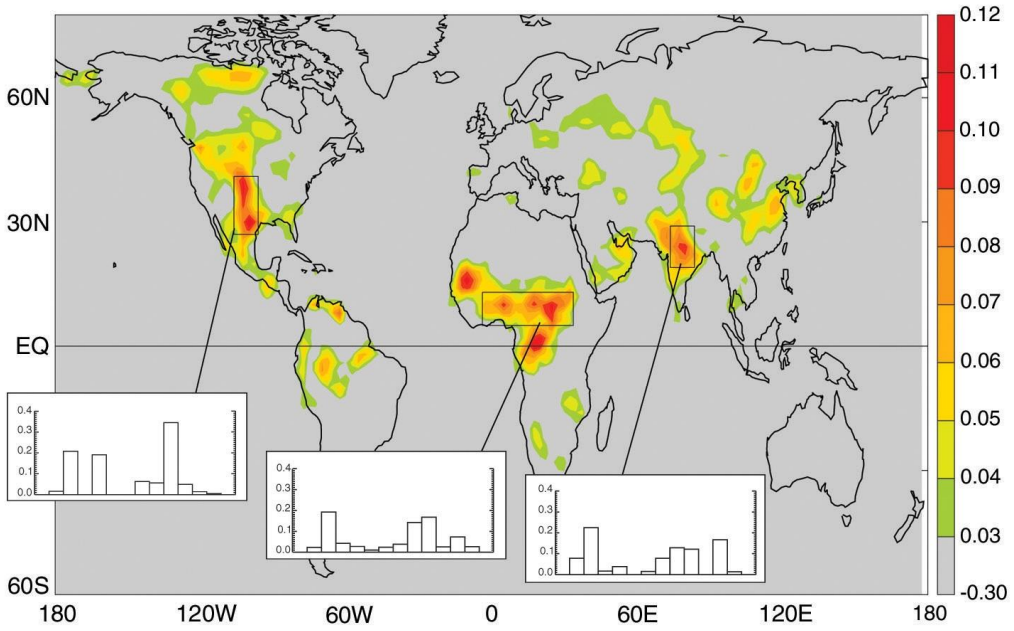

Figure 1.1: The mean strength of land/atmosphere coupling from an ensemble of twelve atmospheric general circulation models participating in the Global Land-Atmosphere Coupling Experiment. The strength of the coupling is indicated by the scale on the right, which is a measure of the ratio between the ensemble mean variance and the intra-ensemble variance. The insets illustrate average coupling strengths for each of the twelve participating models over the outlined hotspot regions of the United States, the Sahel, and India. Reproduced from Koster et al. (2004).

Climatic conditions influence the physiological and phenological processes in plants, including the uptake of carbon. Precipitation, temperature and relative humidity (Collatz *et al.*, 1992), plus radiation and carbon dioxide (CO_2) concentration (Hely *et al.*, 2006) all govern the physiological processes related to the three photosynthetic

biochemical mechanisms in plants – the C_3 and C_4 pathways, and crassulacean acid metabolism (CAM) - such as stomatal conductance, the absorption of photosynthetically active radiation (PAR), and the associated fixation of CO_2 into biomass. Stomatal conductance, for example, is sensitive to light and humidity, but also to the concentration of CO_2 in the atmosphere (Collatz *et al.*, 1992). In the transition zones between dry and wet climates, such as savannah landscapes of the Sahel, increasing atmospheric CO_2 is expected to elicit a reduction in stomatal conductance, leading to a reduction in evapotranspiration and a more efficient use of the available soil water (Drake *et al.*, 1997).

In these transition zones in the tropics species exploiting the C_4 photosynthetic pathway are widespread, whereas most terrestrial ecosystems, such as rainforests, are dominated by C_3 species (Collatz *et al.*, 1992), with CAM most common in succulents of arid regions (Keeley and Rundel, 2003). C_4 and CAM plants both concentrate CO_2 around the enzyme ribulose-1,5-bisphosphate carboxylase oxygenase (Rubisco), which catalyses the main photosynthetic step. Improved water use efficiency (WUE) results from their higher photosynthetic capacity coupled with lower stomatal conductance (Collatz *et al.*, 1992; Keeley and Rundel, 2003) which generally leads to increased primary production (Melillo *et al.*, 1993). In grassland and semi-arid regions, the major effect of elevated atmospheric CO_2 is improved efficiency; whereas over tropical forests increased primary production results from direct CO_2 'fertilisation' in which the increased CO_2 enhances carbon fixation by Rubisco (Nemani *et al.*, 2003). Most of the increased carbon is expected to be allocated to storage tissues such as wood or roots (Drake *et al.*, 1997). Although there is considerable evidence that rising atmospheric CO_2 concentrations stimulate photosynthesis, acclimation to elevated CO_2 means

photosynthetic capacity will reach saturation (Drake *et al.*, 1997; Schaphoff *et al.*, 2006).

Experiments such as those of Cox *et al*. (2000), in which climate change was predicted to cause a drying of the Amazon basin, and resultant forest dieback, infer that feedbacks in the global carbon cycle could be important to future climate change. Even if atmospheric greenhouse gas concentrations were stabilised, the climate system has a long-memory; anthropogenic warming and its impacts would continue for the foreseeable future (Melillo *et al.*, 2002). Large uncertainties though remain with respect to our understanding of biogeochemical cycle feedbacks, which diminishes our ability to accurately predict climate forcing. Coupled general circulation models (GCMs), in which the land surface scheme forms an important component, are the tools we use for predicting climate change and for assessing land/atmosphere feedbacks over future decades and centuries.

1.3. Land surface modelling

The objective of land surface models is to represent all the biophysical and biogeochemical processes that constitute the terrestrial biosphere. They can be defined as complex frameworks of mathematical expressions representing the underlying surface and subsurface ecosystem processes - such as photosynthesis, respiration, decomposition, and nutrient cycling - which explain the surface-to-atmosphere fluxes of heat, water and carbon (Melillo *et al.*, 1993). They determine surface radiative properties, and as important components of climate models can influence atmospheric processes such as radiative fluxes, cloud cover, precipitation, and atmospheric chemistry. These coupled systems are key tools in climate science for predicting likely future states of the Earth system subject to anthropogenic forcing (IPCC, 2007). To

dynamically model the distribution of vegetation over the Earth's surface, land surface models are often coupled to dynamic global vegetation models (DGVMs).

These components, which dynamically model vegetation cover in response to climatic and atmospheric changes, and can be used to understand past and future drivers of vegetation change, represent vegetation cover as a collection of different plant functional types (PFTs); each of which constitute a fraction of the total vegetative cover of the land. These PFTs can be characterised through key attributes of physiology, such as carbon metabolism; physiognomy; and phenology. In this respect, the complexity of species diversity can be rationalised into a few PFTs, and is a fundamental assumption in DGVMs; necessary intricacy is added by including factors such as soil fertility, and disturbance - the most important being fire and herbivory (Cramer *et al.*, 2001). Indeed, in some models (Smith *et al.*, 2001) mortality, succession, and disturbance have been factored in to the extent that PFTs have been grouped into age-related cohorts.

To facilitate a balanced view of the effects of climate related changes to the land surface an ensemble of models are often run under a standardised modelling protocol. Net primary productivity (NPP) has been a conventional output (Cramer *et al.*, 1999; Schloss *et al.*, 1999; Alo and Wang, 2008) in which to compare the predictions of the individual models. For example, in the eight-model intercomparison by Alo and Wang (2008) an increase in NPP was predicted over the majority of the globe under most Intergovernmental Panel on Climate Change (IPCC) emission scenarios. Sensitivity is generally greater under conditions where nutrient constraints are present (Cramer *et al.*, 1999) or where temperature and precipitation are limiting (Schloss *et al.*, 1999). Indeed, over semi-arid regions an increase in CO_2 resulted in an increase in NPP (Cramer *et al.*, 1999). However, much uncertainty exists between the different models. As such, in order to understand the effects of future climate change on terrestrial ecosystems, the

ongoing assessment of the climate sensitivity of models remains a priority. This provides the motivation for participation in an NPP intercomparison exercise detailed in chapter 2.

There are a number of reasons for substantial variability in model predictions. Most revolve around their approximate representation of biophysical processes, climate sensitivity of key parameters, and the heterogeneity of the land surface (Schaphoff *et al.*, 2006; Alton *et al.*, 2007a). Of key significance here is the ability to accurately determine the surface energy balance of the land; and the estimation of land surface temperature (LST) is central to this premise (Kustas and Norman, 1996; Jin *et al.*, 1997; Rhoads *et al.*, 2001; Ge *et al.*, 2008). This justifies a concerted effort to evaluate this key variable, and to attempt to reduce uncertainty in its quantification, as described in chapters 3 and 4 respectively.

Disturbance regimes are also overlooked in many models. Herbivory is almost universally neglected, whereas fire has progressively been incorporated into current land surface schemes. However, most of these fire routines are based around prescribed vegetation mortality or rely on simple empirical algorithms; as a consequence, realistic estimates of emissions from biomass burning have not been modelled (Williams *et al.*, 2007; Thonicke *et al.*, 2010). Part of the motivation for the investigation described in chapter 5 is to ascertain whether an optimised quantification of the surface energy balance could improve the derivation of one of the most important determinants of the fire regime.

In summary, deficiencies in fuel estimation for disturbance modelling (van der Werf *et al.*, 2006) and the variability between different models (Alo and Wang, 2008) compound the uncertainty in how the terrestrial biosphere may evolve in the future

under climate change scenarios. This encapsulates the motivation for the focus of the whole research project.

1.4. Africa

In few places is this uncertainty greater than for Africa, which was described as a weak link by Williams *et al*. (2007) in the understanding of the global carbon cycle. Most research has instead been concentrated on quantification of the carbon cycle in regions of the world with a highly developed infrastructure such as North America and Europe. Yet, Africa is the second largest continent occupying about 20% of global land mass, with a population of nearly 15% of the global total. It is also home to wide variety of ecosystems which range from deserts, through arid and semi-arid mixed tree and grass communities, to humid tropical forests.

With this continent remaining the least studied (IPCC, 2007), little is known about its carbon balance; it remains unknown whether Africa is a source or sink of carbon (Williams *et al.*, 2007). Fossil fuel emissions are still relatively low – although these are increasing dramatically (Boden *et al.*, 2009) - in comparison with carbon uptake and release from the myriad of ecosystems. These fluxes are strongly linked to climate fluctuations, and in recent years a concerted effort has been undertaken to quantify the carbon balance of the continent. Lewis *et al*. (2009) for example, suggested aboveground carbon stocks have increased in the tropical forests, but did not draw any conclusion as to the cause. Leading the effort though has been the CARBOAFRICA project, under the Sixth Framework Programme of the European Commission (http://www.carboafrica.net). A contribution to this research endeavour is outlined in chapter 2.

Despite such efforts climate scenarios remain uncertain, most notably for the vast savannah landscapes (Bombelli *et al.*, 2009). These systems cover approximately 15

million km^2, equivalent to 50% of the area of the continent. They can range from savannah grasslands where woody cover is widely scattered to woody savannah, although a precise definition in terms of the percentage of tree cover may be ambiguous. It is the coexistence of woody and herbaceous vegetation regulated by a distinct wet/dry seasonality however, which is the common characteristic classifying such systems (Scholes and Archer, 1997; Sankaran *et al.*, 2005; Bucini and Hanan, 2007). Of the world's savannah biome 70% is located in Africa - with this being responsible for between 10% and 15% of global NPP (Ciais *et al.*, 2009). The co-existence of trees and grass are a feature of these highly heterogeneous systems, in which production, hydrology, and nutrient cycling are primarily determined by woody cover (Sankaran *et al.*, 2005), which itself is regulated by climate, anthropogenic land use, soil characteristics, fire, and herbivory (Sankaran *et al.*, 2008). The latter of which comprises grazing and browsing by both vertebrates and invertebrates. Savannahs are complex elements within the global carbon cycle exhibiting strong wet and dry seasonality, and are particularly vulnerable to climate change (Sankaran *et al.*, 2005). The seasonal responses of trees and grasses are closely linked to their structure and function. For example, many species of trees green-up prior to the first rainfall of the season, whereas grasses tend to be water limited; the principal cues for leaf flush are temperature, humidity, soil moisture and day length (Archibald and Scholes, 2007). Savannahs are also some of the most frequently burnt landscapes (Bowman *et al.*, 2009).

In a recent review by Schultz *et al.* (2008), Africa contributed approximately 70% to the global burned area and almost 50% of the global fire emissions between 1960 and 2000. Widespread burning in the savannahs (Figure 1.2) is responsible for most of the continent's biomass burning. Drivers of fire here include the presence of ignition

sources, the characteristics of the fuel – the amount, type, density, and moisture content - and the underlying weather conditions (Archibald *et al.*, 2009) - particularly antecedent precipitation (Archibald *et al.*, 2010). The majority of these fires are thought to be anthropogenic in origin, driven by socio-economic reasons including land clearance and pasture maintenance (Roy *et al.*, 2008). To better understand the structure and function of these fire dominated savannah systems land surface models need to incorporate dynamic disturbance mechanisms which are driven by realistic representations of the fuel components and ignition sources.

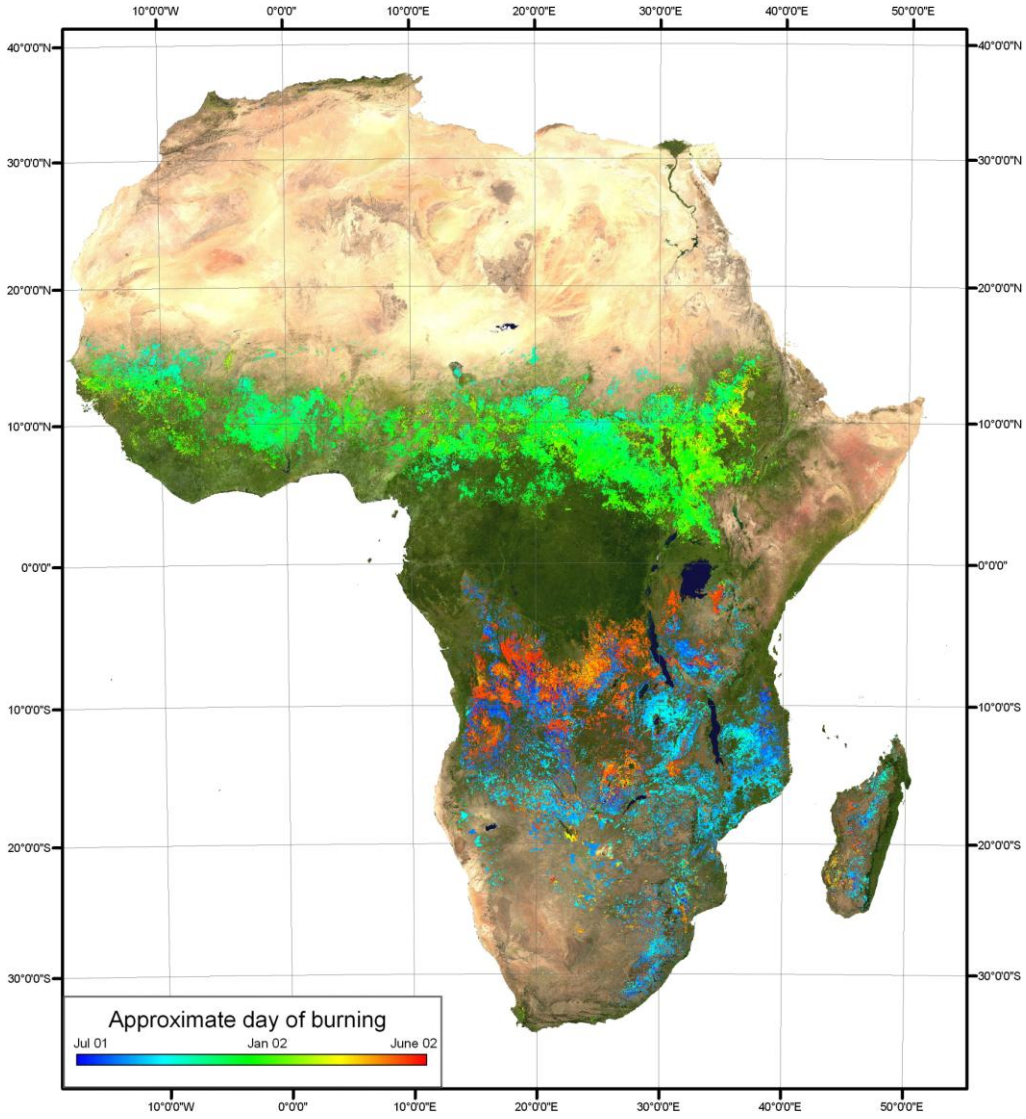

Figure 1.2: Burned area displayed according to detection date in a rainbow scale, as derived from the MODIS collection-5 product from July 2001 to July 2002. Reproduced from Roy et al. (2008).

Considering climate models have produced substantial differences in potential scenarios for Africa (Williams *et al.*, 2007), the continent is an appropriate choice for the research discussed in this study. During the 20th Century Africa experienced an overall warming, and in most scenarios this warming is expected to continue and accelerate, to between 2°C and 6°C warmer by the end of the 21st Century (Hulme *et al.*, 2001). Since the African observation network is relatively sparse, the use of land surface models coupled with remotely sensed data represents the most feasible option for predicting the effects of climate change over this region. An evaluation, and an attempt to improve quantification, of the surface-to-atmosphere fluxes of heat and water for one of the most important land surface models, is thus an important undertaking.

1.5. Summary

This thesis is divided into several self-contained chapters which describe a particular aspect of the research study. Taking the most important land surface model in the UK as an appropriate benchmark, the overall research question asks "**can land-surface modelling accurately simulate land/atmosphere interactions in African savannahs given the highly heterogeneous nature of these landscapes?**" This can be broken down into more specific research questions applicable to each chapter.

Chapter 2 focuses on analysing the behaviour of the JULES model with respect to other important land surface models of the European Community, in terms of the variability of key carbon fluxes in response to climatic and atmospheric CO_2 changes. The methodology incorporates a standardised modelling protocol and a uniform suite of climate forcing data, which is a common approach in understanding such model sensitivity. Four research questions are posed here:

i) Are JULES NPP estimates comparable with those of other land surface models?

ii) Which climate variables produce the strongest correlations with NPP?

iii) Is NPP growth rate significantly related to increasing atmospheric CO_2?

iv) Is NPP variability the main driver of net ecosystem productivity variability?

Following this intercomparison with respect to key carbon fluxes which was undertaken to ascertain model credibility, **chapter 3** investigates how accurately the model is able to simulate the radiative properties of the land surface in terms of LST – a key component of the surface energy balance. This is achieved by way of an *in situ* study over a field site representative of the mixed tree/grass landscape of African savannahs, and a continental intercomparison with remotely sensed LST from Earth Observation (EO) satellites. The two research questions posed are:

i) How accurately is LST simulated by JULES and retrieved from EO satellites for a mixed tree/grass landscape of Africa?

ii) How comparable is LST simulated by JULES over continental Africa with respect to satellite-derived LST products?

Having identified the uncertainties in modelling this key boundary condition **chapter 4** focuses on analysing the behaviour of the JULES model when instantaneous LST observations from EO satellites are integrated into the model. The aim is to investigate whether a reduction in uncertainty can be achieved when modelling important fluxes of heat and water between the land and the atmosphere. The two research questions posed are:

i) Can a reduction in the uncertainty of surface energy fluxes be achieved by constraining simulations of LST with observation data?

ii) How does the assimilation of satellite-derived LST affect the quantification of soil moisture?

Chapter 5 investigates whether the model skill developed in previous chapters can be applied to improve the capability to model the fire regime. In this respect, the derivation of a first modelled dataset of one of the most important drivers of fire occurrence and propagation - fuel moisture content - over the mixed tree/grass environments of the African continent. The two research questions posed are:

i) Can fuel moisture content be satisfactorily estimated across the savannah landscapes of Africa using a land surface modelling approach?

ii) Can this approach be enhanced by utilising data assimilation of satellite-derived LST?

Finally, **chapter 6** will summarise the key findings of the research study. Whether these successfully resolve the scientific questions postulated, and how they relate to the overarching research question will be discussed. To conclude, any limitations of this undertaking will be examined, and potential prospects for further research highlighted.

Chapter 2

Interannual variability of terrestrial carbon fluxes for Africa

All biogeochemical models are subject to inherent uncertainties in their representation of physical processes. A common approach in understanding such uncertainties is through systematic comparison of a model with similar models using a standardised modelling protocol and a uniform suite of climate forcing data. As such, modelling changes in key carbon flux variables such as NPP, in response to climatic and atmospheric CO_2 variability, represents a pertinent objective of any intercomparison study.

This chapter focuses on analysing the behaviour of the JULES land surface model, with respect to other important land surface models of the European Community. It will briefly describe the JULES model, and justify participation in the international CAMIC Project. Model estimates of the interannual variability in continental NPP will be presented, with particular emphasis on analysing the factors responsible for the patterns obtained.

2.1. Introduction

The uptake of carbon by plants during photosynthesis is defined as gross primary productivity (GPP), with the respiratory loss for plant growth and maintenance defined as autotrophic respiration (R_a) (Randerson *et al.*, 2002); the difference between these is NPP. The flux of ecosystem carbon between the land surface and the atmosphere is defined as net ecosystem productivity (NEP), and is a measure of whether the terrestrial ecosystem is acting as a source or sink of carbon. This quantity is simply NPP minus the respiratory loss from non-photosynthetic organisms – known as heterotrophic

respiration (R_h). Utilising models to understand the land/atmosphere flux of carbon and its variability is important for understanding carbon cycle feedbacks in the climate system.

Systematic comparisons of seasonal and interannual flux measurements are a priority to reduce uncertainties in terrestrial carbon modelling (IPCC, 2007), with current land surface models showing conflicting responses in primary productivity. For instance, in the intercomparison between six land surface models by Cramer *et al*. (2001) estimates of global NPP differed by as much as 30%. This is considerable, given that annual anthropogenic carbon emissions to the atmosphere, which account for less than 10% of global NPP (Campbell and Norman, 1998), have had a measurable effect on climate during the course of the 20th Century (Knorr and Heimann, 2001). Indeed, even 5% variability in the prediction of primary productivity over decadal timescales is significant in the context of the carbon cycle (Alton *et al.*, 2007a). NPP has increased in recent years, particularly in tropical ecosystems, with 1982 to 1999 experiencing an increase of 6% in global NPP at a mean rate of 0.19 Pg Cyr^{-1} (Nemani *et al.*, 2003), but with substantial interannual variability (IAV). The variability in NPP together with that of R_h, which is principally sensitive to temperature (Hashimoto *et al.*, 2004), determines whether the terrestrial biosphere is acting as a source or sink of carbon.

With regards to the carbon balance of the African continent; although this appears to be approximately neutral on a decadal scale, Africa contributes nearly half of the IAV in NEP on global scale (Williams *et al.*, 2007). This large variability results primarily from climatic induced response in NPP, which is controlled by factors such as the El Niño Southern Oscillation (ENSO) - an oceanic-atmospheric phenomenon in the tropical Pacific – and carbon release from biomass burning (Anyamba *et al.*, 2002; Hashimoto *et al.*, 2004; Le Page *et al.*, 2008). Indeed, tropical NPP variability is

dominated by El Niño events (Nemani *et al.*, 2003), which are characterised by warmer than average conditions in the eastern tropical Pacific, and lead to drier than average conditions during the main November to February wet season in southern Africa and above-average rainfall in equatorial eastern Africa (Nicholson and Kim, 1997). In contrast, La Niña events, which are characterised by colder than average conditions in the eastern tropical Pacific, lead in general to the reverse conditions in eastern and southern Africa (Nicholson and Selato, 2000). During the three major El Niño events in the last two decades of the 20th Century - 1982/1983, 1987/1988 and 1997/1998 - NPP declined globally, albeit with a 6-month lag, in conjunction with increases in global atmospheric CO_2 growth rate; with a similar reduction in NPP being experienced in Africa (Nemani *et al.*, 2003; Hashimoto *et al.*, 2004). Moreover, the impact on the carbon balance during El Niño years can be further intensified, as these events are often associated with increased biomass burning (Hashimoto *et al.*, 2004).

What is more, variability in NPP to some extent drives variability in fire emissions, although with a lag of several months to a year (Williams *et al.*, 2007), through the accumulation of fuel load. Quantifying trends in NPP is thus a prerequisite for understanding the carbon balance of the terrestrial biosphere; and as such, accurate representation of ecosystem seasonality in land surface models, including ENSO effects, is essential for such predictions. Different models predict considerable differences in future climate scenarios, due to the sensitivity in their parameterisation and their approximate representation of biophysical processes (Alton *et al.*, 2007a). With this mind, the thorough testing of biogeochemical models with recent climate data is an important objective to better understand their climate sensitivity, which is crucial for meaningful future predictions.

In this study, the accuracy of NPP and NEP modelled by JULES was assessed as part of an international study to compare the simulations from land surface models over Africa. In addition to the intercomparison, the primary drivers of NPP IAV were investigated; and a comparison was made between this IAV and the strength of El Niño and La Niña events. Finally, the carbon balance of the continent over several years was assessed, and the principal reasons for variability are discussed. To summarise then, the aim of this investigation was to answer the four research questions: i) are JULES NPP estimates comparable with those of other land surface models; ii) which climate variables produce the strongest correlations with NPP; iii) is NPP growth rate significantly related to increasing atmospheric CO_2; iv) is NPP variability the main driver of net ecosystem productivity variability.

2.2. Materials and methods

2.2.1. CarboAfrica Modelling InterComparison (CAMIC) Project

The CARBOAFRICA project has invested much research into a more detailed analysis of the carbon cycle of Africa and its drivers. For instance, a better understanding of the biophysical processes in selected locations across different biomes has been the result of a concerted effort to increase the collection and analysis of ground measurements (Papale *et al.*, 2006; Kutsch *et al.*, 2008). Unfortunately, the scarcity of these locations and the dearth of high quality datasets remains an obstacle to a comprehensive understanding of the carbon balance of the African continent. Instead, modelling studies offer the most feasible alternative, and as such the CAMIC Project was commissioned.

The purpose of such an undertaking was to identify the main drivers determining IAV of terrestrial CO_2 fluxes for Africa, with a reduction in uncertainties a stated priority (Weber *et al.*, 2009). Simulations with four terrestrial biosphere models: LPJ-

DGVM (Sitch *et al.*, 2003), LPJ-GUESS (Smith *et al.*, 2001), ORCHIDEE (Krinner *et al.*, 2005), and JULES were performed using a uniform set of corrected climate forcing data following a standardised modelling protocol. The rationale behind participation in this venture centred on the opportunity to calibrate the parameterisation of JULES for Africa and to compare subsequent model output with that from similar process-based land surface models.

2.2.2. Model description

The JULES land surface model is based on MOSES (Met Office Surface Exchange Scheme), which was developed to calculate surface-to-atmosphere fluxes of carbon, water, and heat when coupled to the UK Hadley Centre's Unified Model. Although the model has been described elsewhere (Cox *et al.*, 1999) in considerable detail, it is pertinent to this investigation to briefly summarise the relevant key aspects. Further particulars will be presented in subsequent chapters corresponding to the theme of those respective chapters, but here we will concentrate on an overview of the NPP derivation.

JULES is a terrestrial grid-box model which is coupled to the TRIFFID (Top-down Representation of Interactive Foliage and Flora Including Dynamics) DGVM, and can be run at a single 'point' or over a gridded surface, and features a fine temporal resolution of typically 30 or 60 minutes. This enforces a requirement for sufficiently frequent meteorological forcing data, which itself imposes a constraint on the spatial resolution of the available forcing data - since only coarse scale sub-daily datasets are currently available. The advantage though with such an approach is the capability to characterise the diurnal cycle. State variables are updated each time-step, though all biophysical parameters remain constant over the duration of any model run. For runs that are not single 'points' the input grid is defined by the dimensions of the driving meteorological data; with the model grid being a subset of the input grid defined by a

given land mask and/or specified latitude and longitude coordinates. Output profiles for any number of a broad set of state variables define the output grid.

Each grid-box is represented as a composite of nine surface fractions or 'tiles'. Five PFTs are defined: broadleaf trees, needleleaf trees, C_3 grasses, C_4 grasses, and shrubs; together with four non-vegetation types: urban, inland water, bare soil and ice. With the exception of ice, which cannot exist in conjunction with any other tile, any combination of surface types is permitted. Although a grid-box may have coordinates in space, the tiles have no spatial location within a grid-box. The subsurface of each grid-box is horizontally homogeneous within a grid-box, but is profiled into four vertical soil layers; with diffusive heat and water exchanges between layers (Figure 2.1) and prognostic soil fields updated from values for the previous time-step using the mean heat and water fluxes over the current time-step (Cox *et al.*, 1999; Smith *et al.*, 2006).

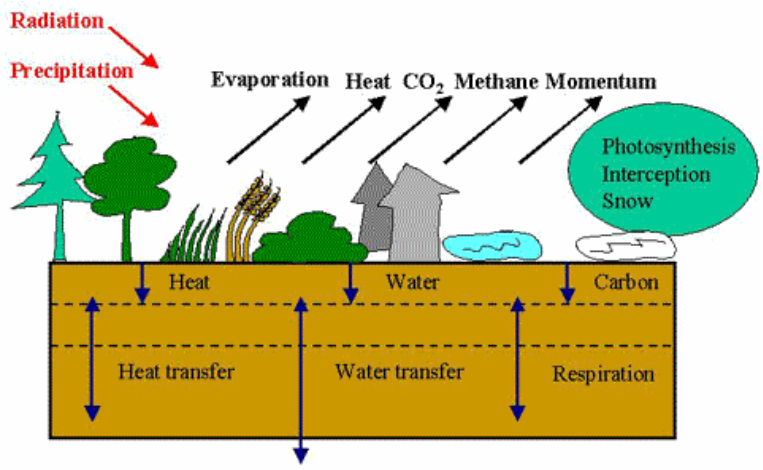

Figure 2.1: Diagrammatic representation of the heat, water, and carbon fluxes between the soil layers, land surface, and atmosphere as modelled by JULES. Figure reproduced from http://www.jchmr.org/jules.

TRIFFID adopts a heuristic modelling approach whereby solving the modified first-order Lotka-Volterra differential equations (1) and (2) determines the density of

carbon C_v and fractional cover v of the five PFTs from the competitive advantages between them (Hughes *et al.*, 2006).

$$\frac{dC_v}{dt} = (1 - \lambda)\, NPP - \Lambda_l \tag{1}$$

$$C_v \frac{dv}{dt} = \lambda\, NPP\, v_* \left(1 - \sum_j c_{ij}\, v_j \right) - \gamma_v\, v_*\, C_v \tag{2}$$

Where v_* is the maximum of v and the constant 0.01, Λ_l is the local litterfall rate, and the fraction λ of NPP is dedicated to increasing v, with the remainder assigned to increasing C_v. The fractional coverage of each PFT i is influenced by the fractional coverage of each PFT j governed by each competition coefficient c_{ij}, with γ_v being the turnover rate.

With regards to NPP, this is expressed in the model as one would expect: GPP minus R_a. Derivations of primary production and respiration are comprehensively described in Cox (2001), with GPP calculated as follows:

$$GPP = 0.012\, (\, A_p\, f_{par}\, \beta \;+\; R_{dc}\, \beta\,) \tag{3}$$

Where 0.012 is a constant to convert from units of mol CO_2 $m^{-2}s^{-1}$ to kg C $m^{-2}s^{-1}$, A_p is the potential rate of net canopy photosynthesis, f_{par} is the fraction of photosynthetically active radiation, R_{dc} is the canopy dark respiration, and β is the soil moisture availability factor. Canopy photosynthesis and dark respiration are determined from scaling-up the leaf photosynthesis models for C_3 and C_4 plants, based on the work of Collatz *et al*. (1991) and Collatz *et al*. (1992) respectively, to the canopy scale following the approach of Sellers *et al*. (1992); which assumes both the maximum rate of carboxylation of Rubisco, and the mean incident PAR are proportional throughout the canopy.

Total R_a is a combination of maintenance respiration (R_{am}) and growth respiration (R_{ag}), whereby R_{am} and R_{ag} are expressed as:

$$R_{am} = 0.012 \; R_{dc} \left(\beta + \frac{(N_r + N_s)}{N_l} \right) \tag{4}$$

$$R_{ag} = r_g \, (GPP - R_{am}) \tag{5}$$

Where N_r, N_s, and N_l are the respective root, stem, and leaf nitrogen contents. R_{ag} is assumed to be a fixed proportion of GPP and the plant maintenance respiration, factored by a growth respiration coefficient r_g, which is identically set for all PFTs.

In the JULES model a total R_h term is absent. Instead, soil respiration (R_s) incorporates belowground microbial respiration, and is expressed as:

$$R_s = \kappa_s \, C_s \, f_\Theta \, q_{10}^{\,0.1 \, (T_s \, - \, 25)} \tag{6}$$

Where κ_s is the specific soil respiration rate at 25°C, C_s is the soil carbon content, q_{10} is a coefficient representing the rate of change as a consequence of a 10°C rise in temperature, T_s is the soil temperature, and f_Θ is a moisture dependent function based on the model of McGuire *et al*. (1992). Aboveground litter respiration is absent in the JULES model, since litterfall from the leaf, wood, and root vegetation carbon pools goes directly into the soil carbon pool with no litter pool existing. This rate of litterfall is determined by PFT-dependent parameters which remain constant over time. Only when the ambient temperature falls below a PFT-dependent threshold level is additional leaf litterfall brought about. However, a similar dependence on soil moisture availability is absent in the model.

2.2.3. Experimental setup

Findings presented here are based on model runs at 1° × 1° spatial resolution, with a 60 minute time-step covering the period 1982-2006. Input and output grids were defined as a rectangle of 77 × 76 grid-boxes, covering the region 21.0°W – 56.0°E longitude, 37.0°S – 39.0°N latitude. In most cases, driving datasets (Table 2.1) were provided by the CAMIC management team to ensure, as much as possible, a uniform set of corrected climate forcing data. Where the requirements of JULES were unique, additional forcing data was acquired from the same original sources if possible.

Table 2.1: Minimum datasets required to drive the JULES model.

Variable	Dataset	Temporal Frequency	Spatial Resolution	Reference
Downward long-wave radiation Downward short-wave radiation Air temperature at 2m Wind speed at 2m Surface pressure Specific humidity	NCEP Reanalysis II	6-hourly	T62 Gaussian	Kalnay *et al*. (1996)
Precipitation	NCEP Reanalysis II	6-hourly	T62 Gaussian	Kalnay *et al*. (1996)
	TRMM 3B43	Monthly	0.25°	Kummerow *et al*. (1998)
	CRU TR 2.1	Monthly	0.5°	Mitchell and Jones (2005)
Soil parameters	ISLSCP I	-	1.0°	Sellers *et al*. (1986)
Soil texture	IGBP-DIS	-	1.0°	Tempel *et al*. (1996)
Land cover classes	ISLSCP II	-	1.0°	Loveland *et al*. (2001)
C_4 fraction	ISLSCP II	-	1.0°	Still *et al*. (2003)
Atmospheric CO_2	Mauna Loa Record	Monthly	-	www.esrl.noaa.gov/gmd/ccgg/trends/

Meteorological forcing data was primarily acquired from the 6-hourly National Centers for Environmental Prediction (NCEP) Reanalysis II data sets. Although in the case of precipitation data, calibration following the method of Sheffield *et al*. (2006) and Williams *et al*. (2008) was carried out to scale the 6-hourly NCEP values to match the monthly Climate Research Unit (CRU) TS 2.1 values (1982-1997) (equation (7)) and the monthly Tropical Rainfall Measuring Mission (TRMM) 3B43 values (1998-2006) (equation (8)). The rationale here was that bias exists between NCEP precipitation data and independent precipitation datasets (Fekete *et al.*, 2004; Ichii *et al.*, 2005).

$$Calibrated\ NCEP_{6hr} = \frac{CRU_{monthly}}{NCEP_{monthly}} \ x\ NCEP_{6hr} \quad (7)$$

$$Calibrated\ NCEP_{6hr} = \frac{TRMM_{monthly}}{NCEP_{monthly}} \ x\ NCEP_{6hr} \quad (8)$$

Since this study was carried out at 1.0° bilinear interpolation was used to re-grid the NCEP datasets, which are projected in T62 Gaussian, to the appropriate spatial resolution. Both CRU and TRMM precipitation data were averaged over 1.0° grid-boxes prior to the aforementioned calibration processing. Resultant 6-hourly values were internally time-interpolated within JULES to the model time-step. In the absence of regional vegetation and non-vegetation parameters, time invariant biophysical parameters were set according to the Hadley Centre's Technical Note 24 (Cox, 2001) and Technical Note 30 (Essery *et al.*, 2001).

A land mask, supplied by the CAMIC management team, was applied to differentiate between the African continent and surrounding water and land-masses. Whether or not the model is coupled to the DGVM fractional distributions of surface

types are required, and in this case were determined (Table 2.2) by applying the linear mapping algorithm of Dunderdale *et al*. (1999) - which was developed for the purpose of producing realistic land surface property variability - to the International Geosphere-Biosphere Programme (IGBP) land-cover classes distribution (Figure 2.2).

An overall grass fraction was acquired from the mapping procedure, which was subsequently differentiated into its C_3 and C_4 components through the application of the International Satellite Land Surface Climatology Project (ISLSCP) II dataset of C_4 fractions. For IGBP land classes composed of cropland, the corresponding percentage of grass PFTs in JULES were designated as agricultural land. With a modelling period of 25 years vegetation-climate feedbacks - as a result of changes to vegetation distribution - were assumed to be significant, and as such land cover change was modelled through TRIFFID with a daily time-step; with the IGBP mapped land cover fractions representing the initial condition.

The model requires nine time invariant soil parameters to be specified for each grid-box, with the option of differentiating each soil layer within a grid-box. Here, soil parameters from the ISLSCP I soil dataset - based on the work by Sellers *et al*. (1986) – was used in conjunction with soil texture, specifically sand and clay fractions, from the Data and Information Systems of the IGBP. These parameters were set as homogeneous across the four soil depths in this study.

Table 2.2: Mapping based on the algorithm developed by Dunderdale et al. (1999) from IGBP land cover classes to JULES surface types: Broadleaf Trees (BT); Needleleaf Trees (NT); C_3 Grasses / C_4 Grasses (Gr); Shrubs (Sh); Urban(Ur); Inland Water (IW); Bare Soil (BS); and Ice (Ic). The C_3 / C_4 grasses are differentiated into their respective components using the ISLSCP II C_4 fractional coverage dataset.

IGBP Code	IGBP Name	JULES Tile Percentages							
		BT	**NT**	**Gr**	**Sh**	**Ur**	**IW**	**BS**	**Ic**
0	Water Bodies	0.0	0.0	0.0	0.0	0.0	100.0	0.0	0.0
1	Evergreen Needleleaf Forest	0.0	69.3	22.2	0.0	0.0	0.0	8.5	0.0
2	Evergreen Broadleaf Forest	85.9	0.0	7.9	0.0	0.0	0.0	6.2	0.0
3	Deciduous Needleleaf Forest	0.0	65.3	25.6	0.0	0.0	0.0	9.1	0.0
4	Deciduous Broadleaf Forest	62.4	0.0	15.9	3.7	0.0	0.0	18.0	0.0
5	Mixed Forest	35.5	35.5	20.9	0.0	0.0	0.0	8.1	0.0
6	Closed Shrublands	0.0	0.0	25.0	60.0	0.0	0.0	15.0	0.0
7	Open Shrublands	0.9	0.0	17.8	34.2	0.0	0.0	47.1	0.0
8	Woody Savannas	50.0	0.0	15.0	25.0	0.0	0.0	10.0	0.0
9	Savannas	20.0	0.0	75.0	0.0	0.0	0.0	5.0	0.0
10	Grasslands	0.0	0.0	81.7	4.9	0.0	0.0	13.4	0.0
11	Permanent Wetlands	2.2	0.0	80.9	1.4	0.0	15.0	0.5	0.0
12	Croplands	0.0	0.0	79.6	0.0	0.0	0.0	20.4	0.0
13	Urban and Built-Up	0.0	0.0	0.0	0.0	100.0	0.0	0.0	0.0
14	Cropland / Natural Vegetation Mosaic	2.5	2.5	80.0	5.0	0.0	0.0	10.0	0.0
15	Snow and Ice	0.0	0.0	0.0	0.0	0.0	0.0	0.0	100.0
16	Barren or Sparsely Vegetated	0.0	0.0	0.0	0.0	0.0	0.0	100.0	0.0

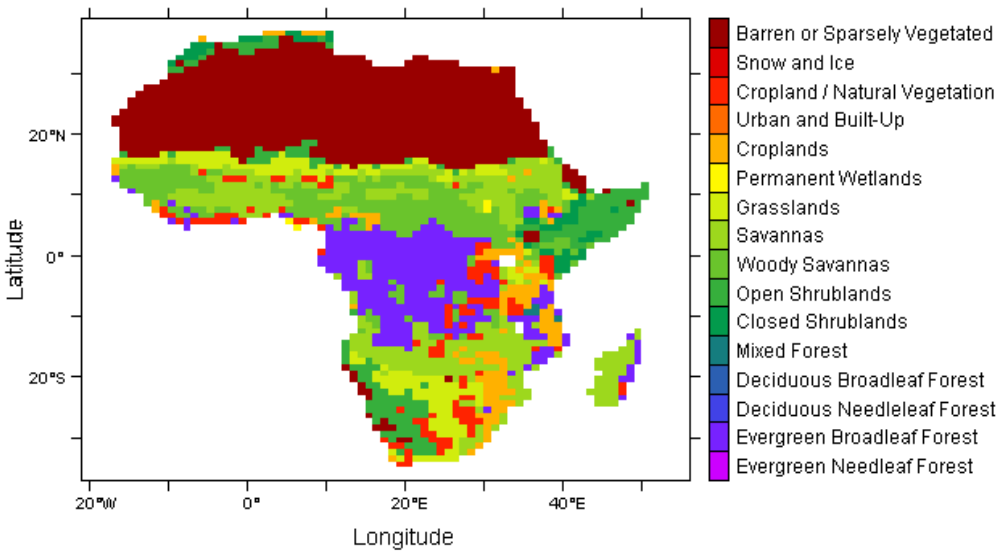

Figure 2.2: IGBP land-cover classes for Africa at 1.0° spatial resolution.

Prior to a main run, JULES should be spun-up to equilibrate the soil conditions, whereby the model is forced with climate data over a set time window - called the spin-up cycle - with this cycle repeated until equilibrium is reached in the soil thermal and hydrologic properties. More specifically, until the change in both soil moisture and soil temperature for each grid-box is less than a specified percentage between subsequent spin-up cycles. Although only changes in these physical properties of the soil are measured, this has an indirect effect on the carbon stocks. This is because both soil moisture and soil temperature are primary determinants of soil carbon loss through the process of soil respiration. This equilibrium state is used as the initial condition for the main run, the purpose being to limit anomalous responses at the beginning of the simulation. In this case, the spin-up cycle was designated as the 10-year period 1982-1991; and this was repeated until changes in soil moisture and soil temperature between consecutive cycles were less than 1% for every grid-box. A single atmospheric CO_2 concentration taken as the 1982 mean value of 341.13ppmV from the Mauna Loa Record was set to be constant throughout the spin-up. Subsequent CO_2 concentrations

were allowed to vary in line with the monthly atmospheric CO_2 concentrations from the Mauna Loa Record. Mean output conditions at each hour over the 25-year modelling period were extracted for each grid-box into annual files for GPP, NPP, and R_s. NEP was derived as NPP minus R_s, where the assumption was made that R_s could act as a surrogate for R_h.

2.3. Results

2.3.1. Primary productivity

The highest rates of photosynthesis are concentrated in the tropical broadleaf forests of central Africa, with GPP values of 4000g Cm^{-2} or more (Figure 2.3). These values decline to the north and south as the climate becomes more arid and tree cover decreases. The arid zones, such as the Sahara, exhibit values close to zero. Over the whole continent, the mean annual rate of GPP between 1982 and 2006 was calculated at 31.50 Pg Cyr^{-1} (Table 2.3), which is approximately one hundredfold the magnitude of maximum fossil fuel emissions for the continent, which increased from 0.157 to 0.291 Pg Cyr^{-1} between 1982 and 2006 (Boden *et al.*, 2009).

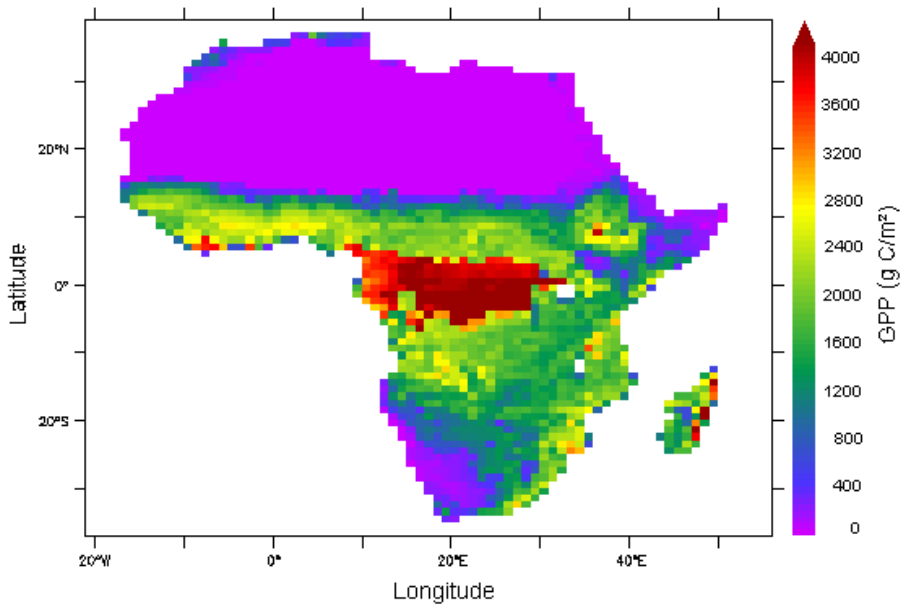

Figure 2.3: Mean annual GPP (g Cm^{-2}) at 1.0° spatial resolution for 1982-2006 as estimated by the JULES model.

Table 2.3: Comparison between the participating models in the CAMIC Project of mean annual continental GPP and NPP [IAV] in Pg Cyr^{-1}. Table reproduced from Weber et al. (2009).

Output	**CAMIC Participating Models**			
	JULES	LPJ_DGVM	LPJ_GUESS	ORCHIDEE
GPP	**31.50 [0.91]**	39.68 [1.73]	16.58 [1.04]	29.80 [1.20]
NPP	**12.01 [0.48]**	17.28 [1.12]	9.16 [0.67]	15.38 [0.77]

The value of GPP derived from JULES is dependent on the mechanics and parameterisation of the model, and as is clear from Table 2.3, different land surface schemes can produce widely varying estimations; ranging in this case from as low as 16.58 Pg Cyr^{-1} for LPJ-GUESS to 39.68 Pg Cyr^{-1} for LPJ-DGVM; even when a standardised modelling protocol and as uniform a suite of climate forcing data as possible is used. Furthermore, photosynthesis displays a considerable IAV - in the case of JULES the standard deviation was calculated as 0.91 Pg Cyr^{-1} – concentrated in regions corresponding to the IGBP land cover classes of woody savannas and savannas

(Figure 2.4). It is in these regions, characterised by distinct wet and dry seasons, where moisture becomes limiting during sustained dry spells. It is also evident from figure 2.4 that while the magnitude of carbon sequestered by photosynthesis varies considerably between the CAMIC participating models, they do share a similar distribution in the rate of IAV.

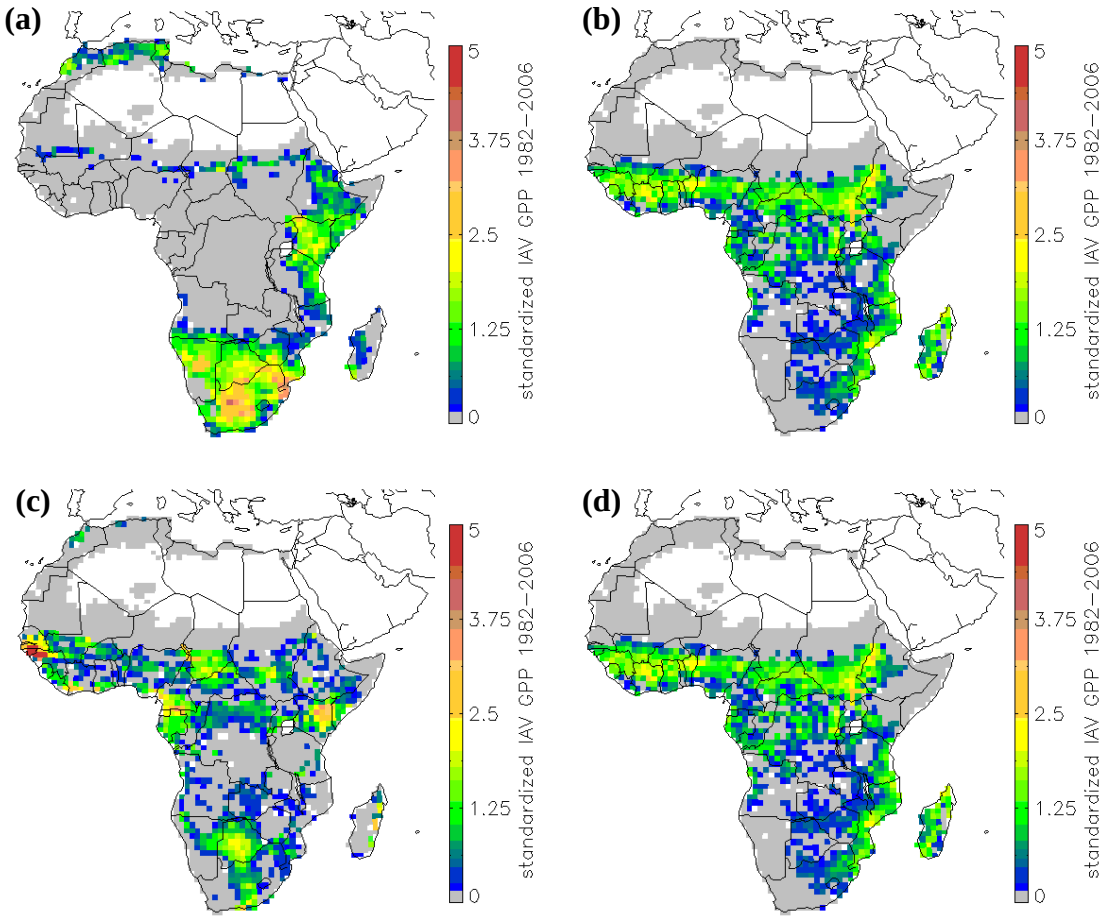

Figure 2.4: Standardised interannual variability – which is a measure of the degree of variability in units of standard deviations - of modelled GPP for the four participating CAMIC models: LPJ-DGVM (a); ORCHIDEE (b); JULES (c); and LPJ-GUESS (d). Figure reproduced from Weber et al. (2009).

Following respiratory loss for plant growth and maintenance - autotrophic respiration – the resultant NPP displays a similar geographical distribution, in that the highest values of around 1000 g Cyr^{-1} are found in the regions dominated by the IGBP

land cover class of evergreen broadleaf forest, declining to the regions of sparse vegetation; with the savannah ecosystems experiencing the strongest IAV (Figure 2.5). This magnitude and distribution of mean annual NPP is consistent with previous studies (Cramer *et al.*, 1999; Melillo *et al.*, 1993), with the relatively high IAV in savannahs a trait also observed by Williams *et al*. (2007). Furthermore, the mean annual continental NPP of 12.01 Pg Cyr^{-1} (Table 2.3) simulated by JULES is close to the average estimated by the ensemble of the four models participating in the CAMIC study; and is comparable to previously published estimates for Africa, which range between 7.0 and 16.6 Pg Cyr^{-1} (Cramer *et al.*, 1999; Potter, 1999; Cao *et al.*, 2001; McGuire *et al.*, 2001; Potter *et al.*, 2003; Williams *et al.*, 2008).

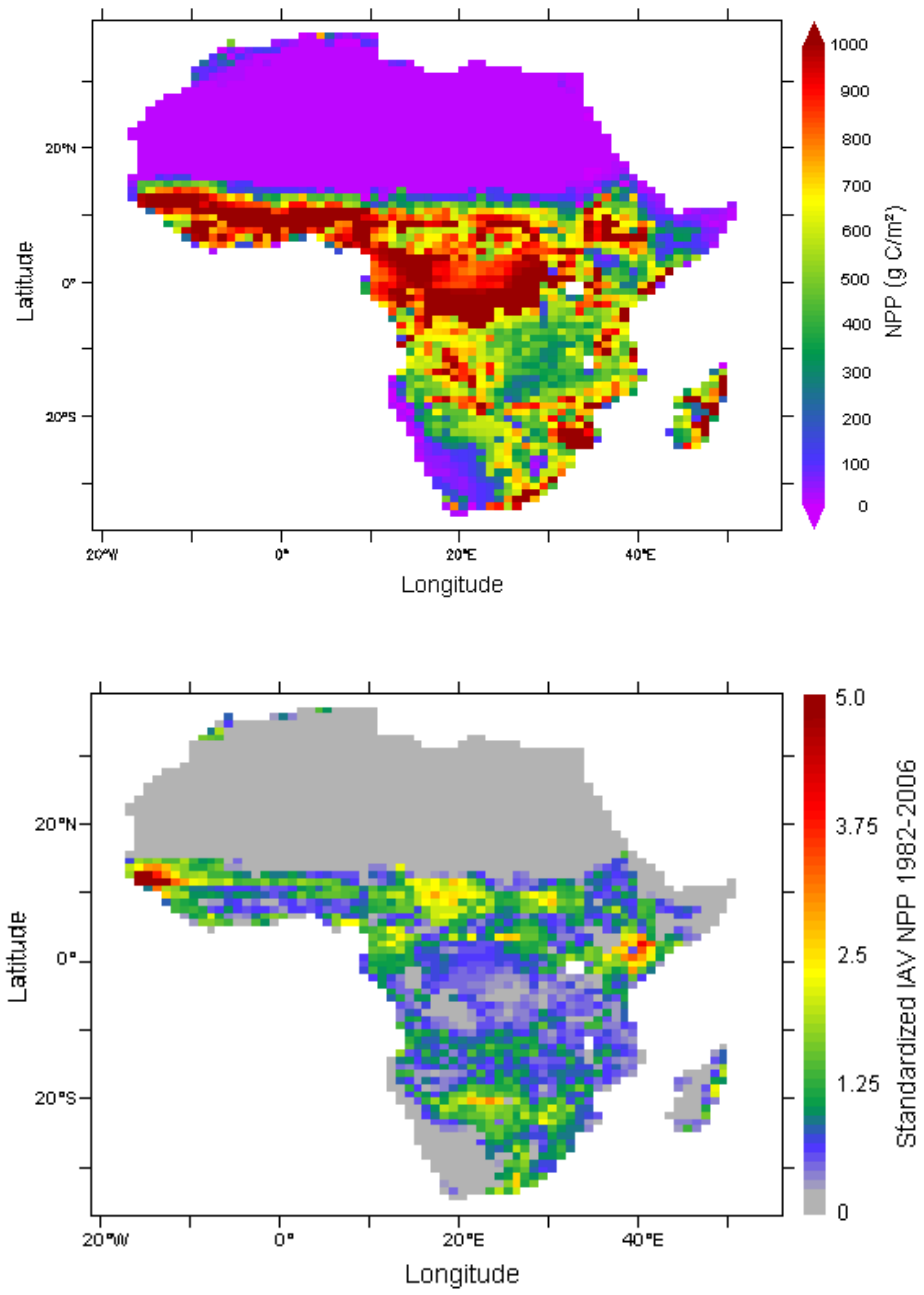

Figure 2.5: Modelled mean annual NPP (g Cm^{-2}) at 1.0° spatial resolution for 1982-2006 as estimated by the JULES model (top); standardised interannual variability – in units of standard deviations - of modelled NPP at 1.0° spatial resolution as estimated by the JULES model (bottom).

To assess the relationship between meteorological forcing data and NPP simulated by JULES on an annual scale, a principal component analysis (PCA) was carried out to extract weather patterns and gradients by reducing the dimensionality of the climate

forcing dataset. The array of climate variables was reduced to their principal components, and Pearson *r* correlations were calculated between the annual NPP and each principal component for each grid-box. As input to the PCA all six meteorological forcing variables were considered: air temperature, specific humidity, precipitation, downward short-wave radiation, downward long-wave radiation, and surface pressure (Table 2.4).

Over 86% of the variability in the annual meteorological data is explained by the first three components of the PCA, and can be used to infer the primary driving forces behind the IAV of NPP in the JULES model. The first component (PC-1) is strongly associated with moisture availability, with high component loadings with respect to both precipitation and specific humidity; but it also exhibits a strong association with downward long-wave radiation. The second component (PC-2) is most strongly associated with air temperature and surface pressure, with the third component (PC-3) primarily associated with downward short-wave radiation. When considering the situation at the grid-box level (Figure 2.6), positive correlations between NPP and PC-1 emerge over much of the continent, being strongest over savannah regions where moisture availability is the primary limiting factor on photosynthesis. Precipitation is one of the main factors responsible for PAR absorption, and the findings here are consistent with this, and in agreement with previous studies (Fang *et al.*, 2001; Williams *et al.*, 2008).

Table 2.4: Principal component analysis of the six meteorological forcing variables: air temperature (T); specific humidity (Q); precipitation (R); downward short-wave radiation (SW); downward long-wave radiation (LW); and surface pressure (P).

Component	Eigenvalue	Variance (%)	Cumulative (%)	Component Loadings					
				T	Q	R	SW	LW	P
1	2.872	47.9	47.9	0.44	0.95	0.90	-0.46	0.86	-0.15
2	1.329	22.2	70.1	0.73	-0.04	-0.07	-0.01	-0.10	0.89
3	0.974	16.2	86.3	0.35	-0.00	-0.01	0.85	0.24	-0.25
4	0.384	6.4	92.7	-0.39	0.09	0.19	0.24	0.09	0.35
5	0.307	5.1	97.8	0.07	0.03	0.35	0.07	-0.41	-0.07
6	0.134	2.2	100.0	-0.02	0.30	-0.17	0.04	-0.12	0.00

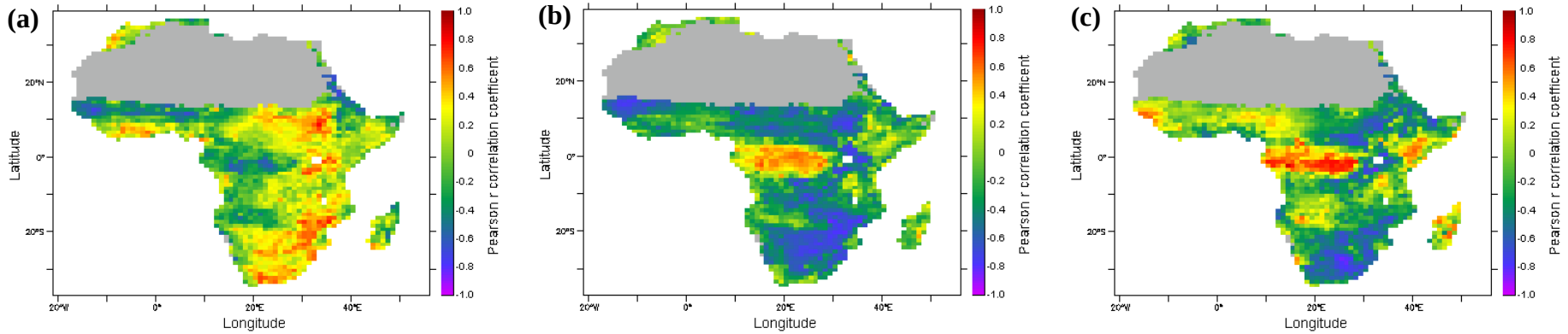

Figure 2.6: Pearson r correlations between modelled NPP and meteorological forcing Principal Components PC-1 (a); PC-2 (b); PC-3 (c).

In the case of PC-2, figure 2.6 indicates a geographical differentiation in which strong negative correlations are manifest in the savannah systems; whereas the correlations are positive in the central tropical forest. A similar picture is evident for PC-3, whereby very strong positive correlations are associated with the equatorial forest, where increased cloud cover over this region adversely affects PAR availability.

Having identified the primary climatic drivers behind the variability of NPP over Africa, it is pertinent to consider what the main causes of climate variability may be, and how these influence IAV in modelled NPP. As discussed in section 2.1 previous investigators have suggested ENSO to be a major driver of climate IAV particularly in southern Africa during the main November-February wet season. An appropriate approach to enable comparison between the strength of El Niño / La Niña events and NPP has been to represent ENSO as a multivariate index (Nemani *et al.*, 2003). This is the approach that is adopted here, with modelled NPP compared with the Multivariate ENSO Index (MEI) devised by Wolter and Timlin (1998) (Figure 2.7). A 6-month lag between MEI and corresponding NPP anomaly resulted in the strongest correlation (r = -0.330, $P<0.01$; N=294).

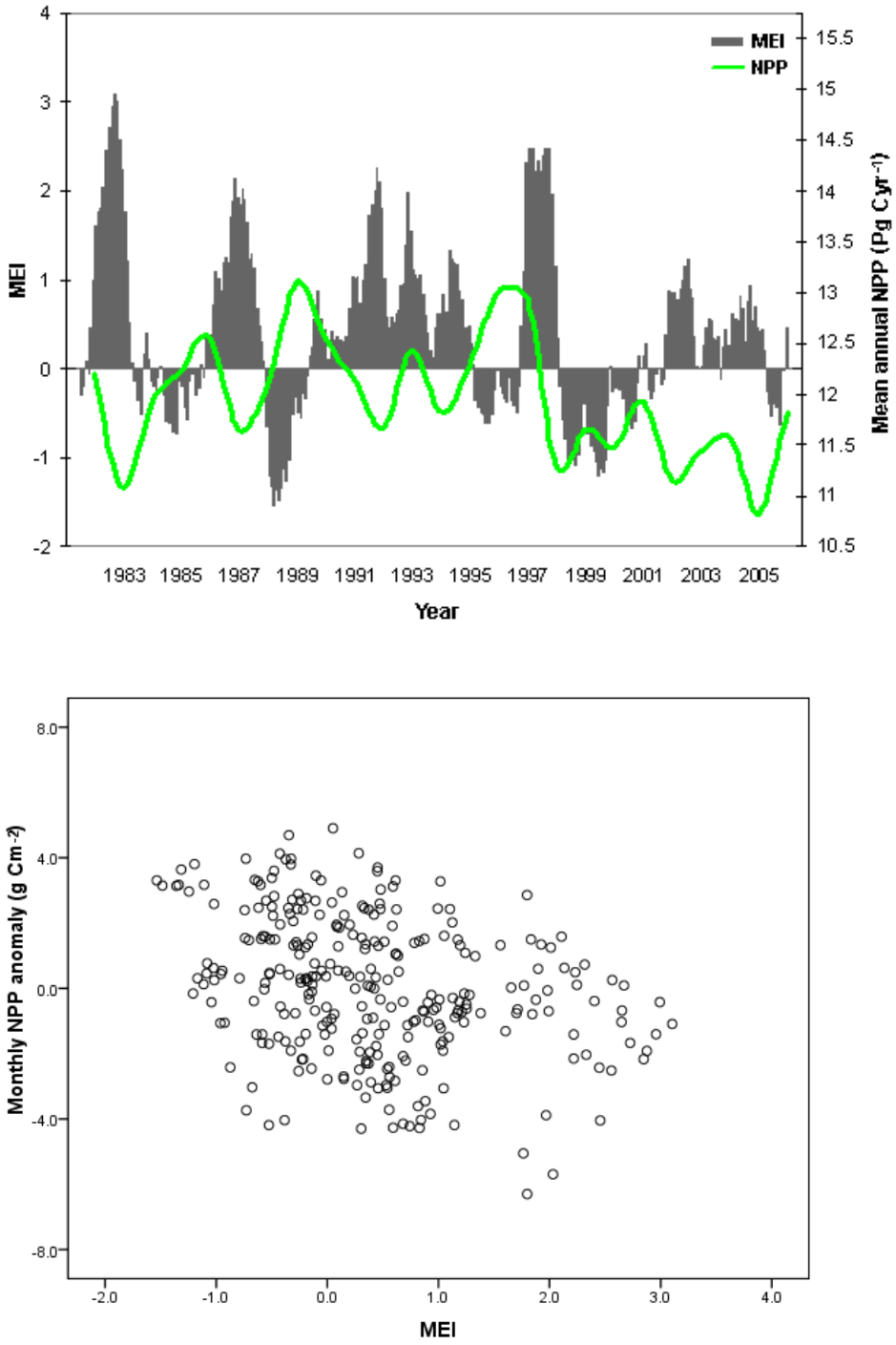

Figure 2.7: Times series of mean annual continental NPP (Pg Cyr^{-1}) against a Multivariate ENSO Index (MEI) (top); scatterplot of monthly NPP anomalies (g C m^{-2}) vs.MEI (bottom). The MEI is based on six variables: sea-level pressure, zonal and meridional surface-wind components, sea-surface pressure, surface-air temperature, and cloud-cover fraction. The magnitude (positive / negative) of the MEI corresponds to the strength of El Niño / La Niña events respectively.

It is clear from figure 2.7 that strong El Niño events are associated with a decrease in NPP, with increasing NPP occurring in conjunction with La Niña events. This negative relationship between NPP and the same MEI was also reported by Nemani *et al*. (2003). The three strong El Niño events of the 25-year modelling period - 1982/1983, 1987/1988, and 1997/1998 – correspond to reduced precipitation in some regions of the continent; this is particularly the case during the 1982/1983 and 1997/1998 events, in which extreme precipitation anomalies are evident in some equatorial areas (Figure 2.8). In addition to these extreme events, NPP is also seen to have sharply decreased during 1991/1992, which was an extremely dry period in southern Africa (Hely *et al.*, 2003). It may have been expected that the long-lasting La Niña event of 1999/2000 may have been responsible for a sharper increase in NPP than is apparent from figure 2.7. This may be due to the fact that extreme rainfall was limited to arid regions with sparse vegetation, whereas densely vegetated humid areas experienced very dry conditions (van der Werf *et al.*, 2006).

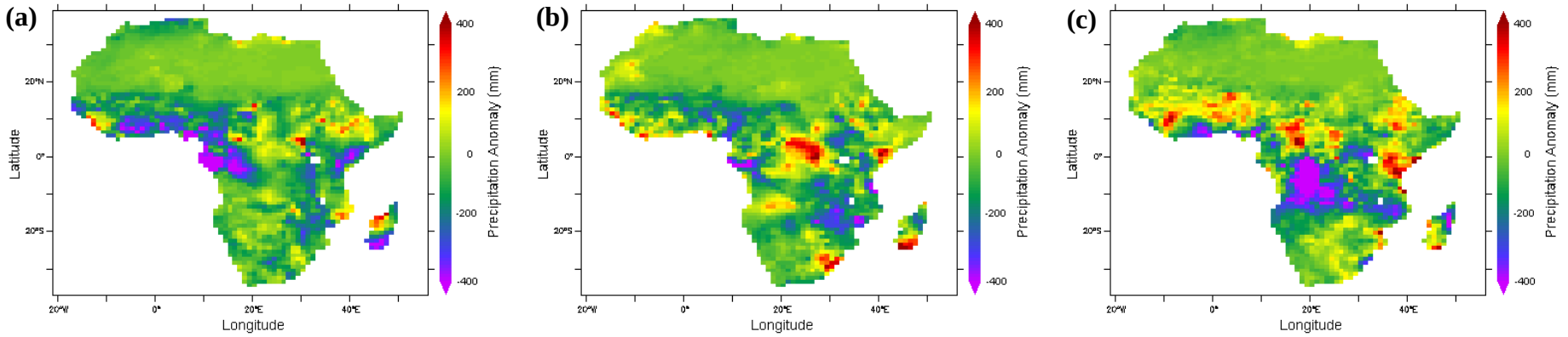

Figure 2.8: Precipitation anomalies with respect to the mean precipitation during the 25-year modelling period 1982 to 2006 during the three major El Niño events of this period: 1982/1983 (a); 1987/1988 (b); 1997/1998 (c). Data is from the NCEP Reanalysis II dataset calibrated with CRU and TRMM monthly data.

In addition to the ENSO phenomenon, monthly NPP growth rate simulated by the JULES model (Figure 2.9) was also found to be significantly related to atmospheric CO_2 growth rate (r = 0.290, P<0.01; N=300) from the Mauna Loa Record; a finding consistent with Nemani *et al*. (2003). A primary candidate for this response in NPP growth rate could be the CO_2 fertilisation effect - particularly in the C_3 broadleaf trees of the tropical forest - whereas over savannah regions, where C_4 grasses proliferate, NPP increases are mainly attributed to improved WUE (Field *et al.*, 1995; Schaphoff *et al.*, 2006). However, this correlation should be treated with caution since changes in NPP and R_h also change the atmospheric CO_2 growth rate (Francey *et al.*, 1995; Keeling *et al.*, 1995) and may be a more reasonable explanation for the correlation.

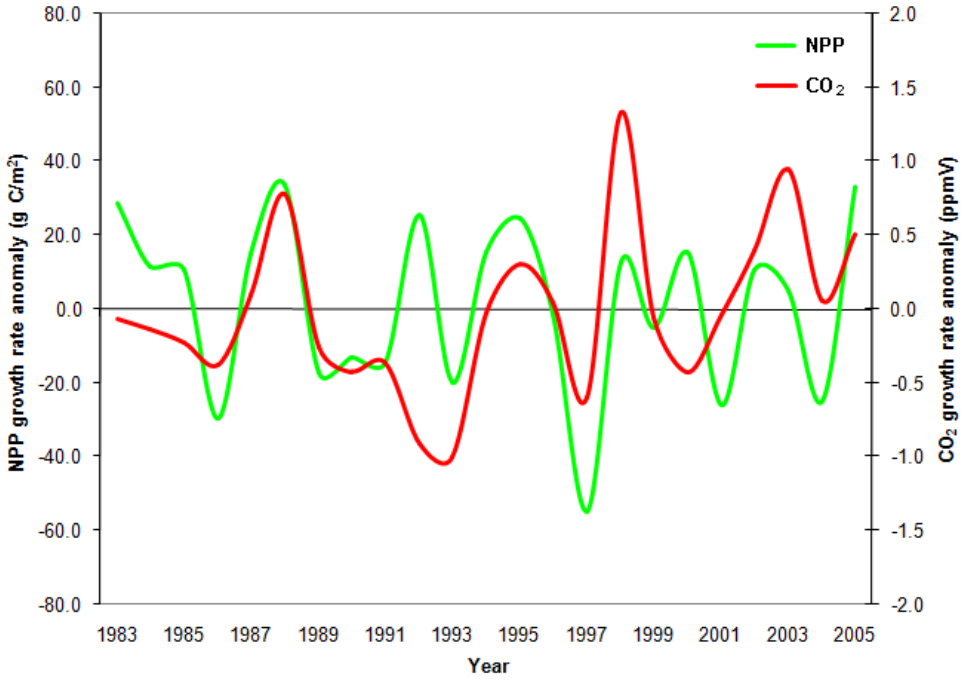

Figure 2.9: NPP growth rate anomalies modelled by JULES in relation to atmospheric CO_2 growth rate anomalies from the Mauna Loa Record. These anomalies are calculated as the difference between yearly values and the mean for the 1982–2006 period respectively.

2.3.2. Carbon balance

The carbon balance of each grid-box is not explicitly derived by the JULES model. NEP was therefore calculated from the output variables - NPP and R_s – the latter was treated as a surrogate for heterotrophic respiration since no aboveground litter respiration is present in JULES. The NEP derived for Africa in this study (Figure 2.10) displayed a large IAV of 0.71 Pg Cyr^{-1}, with a mean terrestrial uptake of 0.14 Pg Cyr^{-1}. In relation to published values, the modelled estimates showed considerable comparability. From 1982 to 1995 the mean uptake was 0.37 Pg Cyr^{-1} - similar to the estimate of 0.34 Pg Cyr^{-1} in Cao *et al*. (2001). During the 1990's a net sink of 0.20 Pg Cyr^{-1} was predicted, which is of a similar magnitude to the 0.15 Pg Cyr^{-1} estimated by Ciais *et al*. (2009). Strictly speaking though, since the model used in this latter study included a simple parameterisation for fire, the published value was an estimate of net biome productivity (NBP); a quantity which includes additional loss due to episodic disturbances, such as fires and harvests (Schulze and Heimann, 1998).

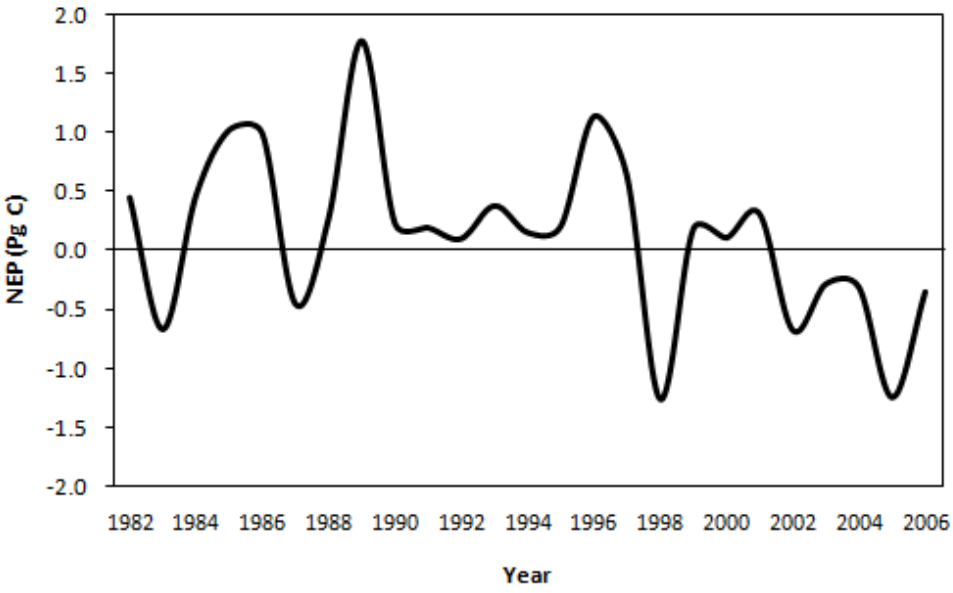

Figure 2.10: Times series of mean annual continental NEP in Pg Cyr^{-1}. Positive values indicate a sink of carbon and negative values indicate a source.

It is clear from figure 2.10 that during the 1980's and 1990's the JULES model simulates Africa to behave as a sink of carbon for much of these two decades, punctuated by three distinct periods which coincide with the three strong El Niño events of 1982/1983, 1987/1988, and 1997/1998, where the continent acts as a source of carbon. These three events are associated primarily with reductions in NPP, but also spikes in R_s (figure 2.11). It is also apparent, that from 2002 onwards Africa exhibits a net release of carbon from the biosphere, averaging -0.57 Pg Cyr^{-1}, with the maximum release occurring in 2005.

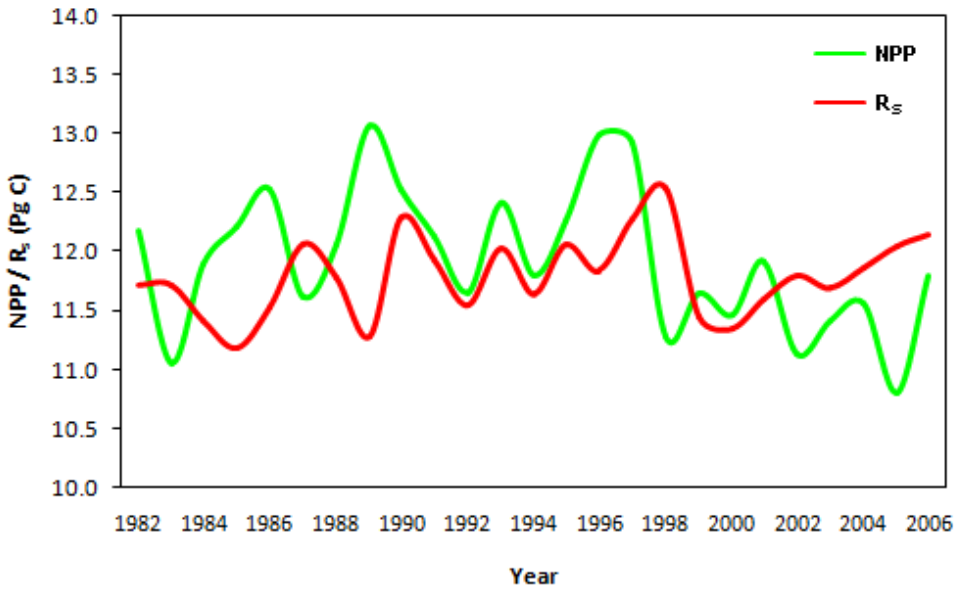

Figure 2.11: Time series of mean annual continental NPP and R_s in Pg Cyr^{-1}.

Although not yielding a strong MEI signal, 2005 experienced both the driest and hottest conditions during the 25-year investigative period (Figure 2.12), particularly in the savannahs. With moisture availability having been identified as a primary factor controlling NPP, and temperature being the single best predictor of soil respiration (Raich and Schlesinger, 1992), it would appear logical that the NEP for 2005 of -1.24

Pg Cyr^{-1} would result both from the lowest annual precipitation encountered during the 25-year period together with above average temperature.

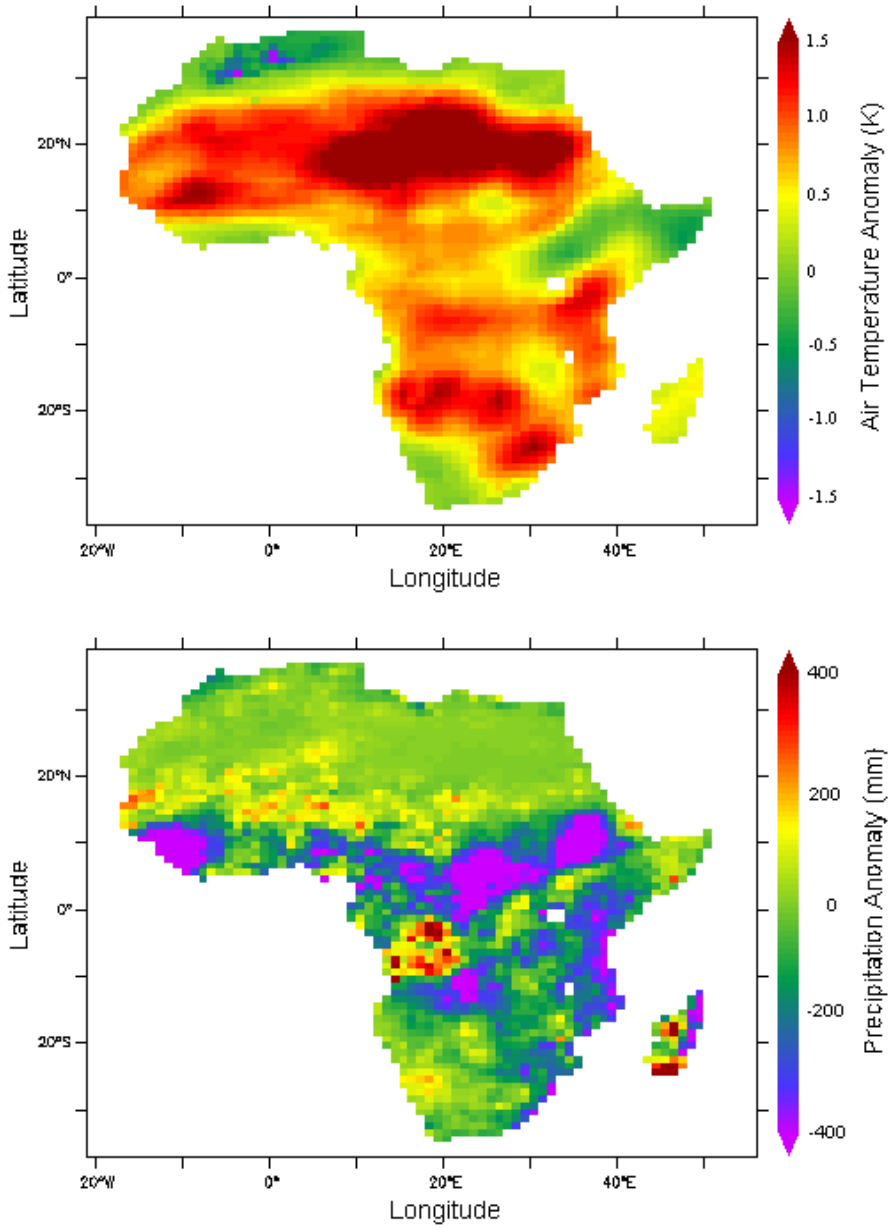

Figure 2.12: Air temperature anomalies (K) (top); and precipitation anomalies (mm) (bottom) for 2005 with respect to the mean air temperature and precipitation respectively during the 25-year modelling period 1982 to 2006. Both air temperature and precipitation data is from the NCEP Reanalysis II dataset, with precipitation data calibrated with CRU and TRMM monthly data.

What we also observe from figure 2.11 is that IAV in NPP (0.48 Pg Cyr^{-1}) is greater than that of R_s (0.34 Pg Cyr^{-1}) in agreement with Raich *et al*. (2002); and over the modelling period an overall downward trend is discernable in NPP in contrast to an overall upward trend in R_s. The prime candidate responsible for this upward trend in R_s is an increasing trend in temperature. Indeed, this 25-year window experienced an overall increase in air temperature of 0.7°C, with the six years spanning 2001 to 2006 representing six of the hottest seven years since 1982. The downward trend in NPP is partly a result of the lower than average values simulated since the last major El Niño event. The cause of this though appears more complicated with no one factor conclusive; and the inference being that multiple changes in climate patterns are responsible, such as increasing temperature in the savannah regions, and decreasing solar radiation over the tropical forests of central and west Africa.

2.4. Discussion

NPP is a biophysical quantity with potentially far reaching influence in climate modelling, whereby systematic comparison of interannual fluxes between models is a priority in reducing terrestrial carbon cycle uncertainties (IPCC, 2007). This is the motivation behind participation in the CAMIC Project; and subsequent investigation into both the drivers of terrestrial carbon flux variability, and the attempt to simulate the carbon balance of the African continent during the recent past.

The results presented here suggest both the magnitude and variability of terrestrial carbon fluxes simulated by the JULES land surface model are comparable both with other state-of-the-art land surface schemes and with published estimates from previous studies. In addition, the primary factors responsible for the variability between years have been identified. However, these findings come with a note of caution. JULES, like probably all land surface models, is limited by the accuracy to which it is able to

represent the complex physical processes that constitute the terrestrial biosphere. This limitation becomes more acute when attempting to imitate highly heterogeneous environments, such as the savannah ecosystems of Africa.

More specifically, in the context of this investigation several limitations within the JULES model are evident. Firstly, the differentiation between evergreen and deciduous broadleaf trees is essential for the accurate modelling of Africa vegetation, whereas in JULES these are both assigned to a single PFT. Incidentally, of the four CAMIC participating models, JULES presents the most simplified PFT specification. Secondly, the phenological cycle is a critical component for accurately modelling carbon fluxes in savannah ecosystems. While environmental cues are reasonably well understood and implemented in temperate environments, no account of leaf senescence is made in the model once water availability falls below a threshold value; whereas the two LPJ models, and ORCHIDEE, all contain raingreen phenology. Finally, despite fire and grazing being important determinants of ecosystem function, particularly in African savannahs (Archibald *et al.*, 2005), these disturbance regimes are a conspicuous omission in the model framework. In contrast, all three of the other participating models in the model intercomparison incorporate fire disturbance, based on Thonicke *et al.* (2001). What is more, ORCHIDEE also includes a simple parameterisation for herbivory. Indeed, this lack of both disturbance functionality and drought-deciduous phenology may be responsible for JULES exhibiting the lowest IAV in NPP of all the participating models.

With regards to the CAMIC project is general, a couple of caveats must also be highlighted before any interpretation of the findings can be made. Firstly, despite the noble attempt to unify datasets, the unique requirements of each land surface model mean some differences in the simulations may be attributed to the different

requirements of the individual models. For example, in the case of JULES, an additional two driving datasets were mandatory for running the model: downward long-wave radiation; and surface pressure. Although great effort was made to ensure the same methodology was applied in the re-gridding process as for the common datasets, uncertainty is unavoidable. Secondly, the treatment of R_h by the modelling community is unconstrained. Both LPJ models and ORCHIDEE derive R_h as the sum of emissions from aboveground litter decomposition and belowground soil decomposition; whereas JULES does not distinguish between aboveground and belowground R_h, instead simply describing a microbial soil respiration quantity. Aboveground heterotrophic respiration by animal biomass is universally ignored by the CAMIC models, most probably because it is difficult to quantify in space and time. This may contribute a non-trivial proportion of the total heterotrophic flux in an ecosystem, and as such disregarding this suggests a potential over-estimation of NEP. Although absolute magnitudes of NEP were not published as part of the CAMIC project, derivations of IAV suggest a probable carbon sink with respect to Africa (Weber *et al.*, 2009). It is therefore pertinent to acknowledge, that the effect of aboveground heterotrophic respiration introduces an explicit uncertainty on these predictions. In the case of JULES, the lack of a litter pool and disturbance functionality means all vegetation carbon lost from the individual PFTs during the process of background litterfall ends up in the soil carbon pool. If the soil respiration rate is inadequately parameterised an over-estimation in the build-up of soil carbon stocks will be simulated - the implication being that the true carbon sink of the continent may be lower than the estimations from JULES.

In a post-assessment of the CAMIC project by Bombelli *et al*. (2009) several sources of uncertainty associated with the model predictions were identified, including a lack of validation data and different representations of the biophysical processes by the

individual models. Most significantly though, particularly in the case of the highly heterogeneous savannah ecosystems, is the way in which the land surface is generalised in models. This is a current limitation inherent in all climate driven land surface models due to the relatively coarse resolution at which spatially heterogeneous climate variables, such as precipitation, are available in order to meet the sub-daily requirements of many models. Nevertheless, the CAMIC project did find some robust patterns in the modelled results. As illustrated in figure 2.4, the largest IAV in GPP was found by all models to be present in regions covered primarily with savannah land cover classes. What is more, the IAV in GPP is greater than that of ecosystem respiration in all models (Weber *et al.*, 2009), and thus exerts a greater influence on the net carbon balance.

For the JULES model the IAV in primary production has been shown to primarily be driven by moisture availability, particularly in savannah ecosystems; whereas short-wave radiation would appear to be the main factor in the central African tropical forest (Figure 2.6). Indeed, in the sensitivity analysis by Alton *et al*. (2007a) short-wave radiation was identified as exercising much control on JULES model output in their tropical forest study site. In these warm moist regions it is presence of clouds which limits photosynthesis by reducing the availability of PAR (Melillo *et al.*, 1993). Climate variability, and hence primary production, is influenced in Africa by factors such as ENSO (Figure 2.7). Furthermore, NPP variability is also influenced by atmospheric CO_2 concentrations (Figure 2.9), although the reverse cause and effect is also a consideration. In the tropical forests, which are principally composed of C_3 plants, CO_2 fertilisation is the prime candidate for CO_2 influence on NPP growth. In the semi-arid regions, where NPP is moisture limited, increased atmospheric CO_2 is likely to lead to an increase in NPP as a result of a reduction in stomatal conductance which increases

WUE. Moreover, increasing atmospheric CO_2 is likely to impact on heterotrophic respiration, since temperature increases associated with anthropogenic driven global warming influence the rates of soil respiration (Raich *et al.*, 2002). Indeed, the relationship between CO_2 and carbon fluxes in the context of Africa merits further research. Although much uncertainty exists in modelling the carbon balance of Africa, findings presented here suggest climatic factors such as ENSO are major drivers behind the IAV in the carbon fluxes of the African continent.

2.5. Conclusions

The purpose of this investigation was to examine the output of the JULES simulations with respect to other established land surface models to identify some of the limitations associated with land surface modelling. With a focus on terrestrial carbon fluxes four research questions were posed to analyse model sensitivity and to understand the drivers of the carbon cycle in Africa: i) are JULES NPP estimates comparable with those of other land surface models; ii) which climate variables produce the strongest correlations with NPP; iii) is NPP growth rate significantly related to increasing atmospheric CO_2; iv) is NPP the main driver of NEP variability.

The estimates of NPP simulated by the JULES model were comparable both with the other participating CAMIC land surface models, and with previously published values; the largest IAV being found in the savannah regions of the continent. This variability can be explained primarily by moisture availability and long-wave radiation, with short-wave radiation important in the central tropical forest. ENSO is a major factor behind the climatic variability and thus NPP variability, with the growth rate in NPP significantly correlated with the growth rate in atmospheric CO_2 concentration. Finally, these driving factors of NPP variability determine for the most part NEP variability, with temperature driven heterotrophic respiration also a significant

controlling factor on the net terrestrial flux of carbon between the land surface and the atmosphere. In conclusion, the JULES simulation suggests a weakening of the African terrestrial carbon sink during the recent past primarily caused by hot and dry conditions in savannahs.

This study has provided an evaluation of the biophysical processes and parameterisation of the JULES model for Africa; and the findings offer evidence that the continued use of the JULES model is justified for this research. However, land surface models have limitations. The mathematical equations which constitute their processing are only able to provide a simplified representation of the infinitely complex workings of the land biosphere. Observations on the other hand are able to describe ecosystems more realistically. We would however, need a lot of field observations to represent every niche in every land habitat. Fortunately, EO satellites provide a feasible alternative source. If we could integrate the instantaneous view of the land surface from satellites into land surface models it is possible we could reduce modelling uncertainties.

Chapter 3

Land surface temperature evaluation

Before attempting to integrate a key variable from EO satellites into the model it is pertinent to investigate how accurately the model is able to simulate the chosen variable. As was highlighted earlier, land surface models have uncertainties due to their approximation of physical processes and parameterisation, and the heterogeneity of the land surface. These can be compounded when key variables are inadequately represented. LST is one such critical variable, as it forms an integral component in the surface energy budget, and its accuracy is essential to applications such as desertification, water stress evaluation and soil moisture-climate feedbacks. Its strong diurnal cycle means that if we are to contemplate integrating more accurate instantaneous observations into biophysical models, then we would be better served with sub-daily observations. EO satellites represent the most practical source over large geographical areas.

This chapter analyses the ability of JULES to effectively simulate LST by way of *in situ* evaluation and a continental intercomparison study with remotely sensed LST from EO satellites. First, we must consider the accuracy of the most commonly used satellite-derived LST products. Although each product has undergone *in situ* validation, the majority of these field campaigns have been carried out over homogeneous sites, which are atypical of the wider landscape. It is therefore justifiable to perform a similar exercise over a more representative field site; in this case the mixed tree/grass landscape of an African savannah. Further evaluation over every unique habitat of Africa is not feasible; instead to strengthen this analysis a multi-temporal intercomparison between EO datasets and LST simulated by the model was carried out. The aim then here is to

consider two questions: i) how accurately is LST simulated by JULES and retrieved from EO satellites for a mixed tree/grass landscape of Africa; ii) how comparable is LST simulated by JULES over continental Africa with respect to satellite-derived LST products.

3.1. Introduction

LST is the radiative skin temperature of the land. It is derived from solar radiation, and is influenced by land/atmosphere boundary conditions such as albedo and precipitation (Huang *et al.*, 2008). It determines the emission of surface-to-atmosphere long-wave radiation (Rhoads *et al.*, 2001), and exerts control over the partitioning of energy into latent heat flux (Sellers *et al.*, 1997), sensible heat flux (Sun and Mahrt, 1995), and heat flux into the ground. LST is distinct from air temperature, with up to 20K differences possible between concurrent measurements of the same patch of dry bare soil (Byrne *et al.*, 1979), and is more closely related to the physiological activities of leaves (Sims *et al.*, 2008). Furthermore, it displays a strong diurnal cycle and can exhibit substantial non-uniformity - as much as 10K - over just a few metres of the landscape (Prata, 1994). This rate of change of LST is sensitive to surface characteristics such as vegetation cover, and soil moisture.

Being an important boundary condition it is an integral component in numerous applications: desertification (Sobrino and Raissouni, 2000); surface energy balance assessment (Pinheiro *et al.*, 2006a); and due to its close relationship to vapour pressure deficit, the monitoring of vegetation water stress (Hashimoto *et al.*, 2008). The importance of LST to the thermal behaviour of the surface and sub-surface of the land ensures it is a key variable in land surface modelling (Kustas and Norman, 1996), with numerous studies (Ge *et al.*, 2008; Jin *et al.*, 1997; Rhoads *et al.*, 2001) using LST as a benchmark for model validation. Over large geographical regions remotely sensed data

from EO satellites offers the most practical source for model validation, since this overcomes the limited spatial extent of local field measurements.

EO satellites determine LST from top-of-atmosphere (TOA) radiances at microwave and thermal infrared (TIR) wavelengths. Microwave retrievals can have substantial uncertainties due to the large range of variation in surface emissivities; whereas TIR retrievals are more sensitive to cloud contamination limiting the spatial and temporal sampling of measurements, but benefit from the peaking of the Planck function in the infrared. Instruments on board EO satellites which measure TOA radiances in the TIR apply a radiative transfer equation which combines the upwelling radiance emitted by the ground, the upwelling radiance emitted by the atmosphere, and the down-welling radiance emitted by the atmosphere and reflected by the ground. LST retrieval accuracy can be challenging as a result of emissivity variability and atmospheric effects. Surface emissivities can be highly variable owing to the heterogeneity of the land; a problem which is amplified in regions of high topographic variance and for larger viewing angles. These need to be accurately dealt with otherwise biases can occur in LST retrieval of several degrees (Schaadlich *et al.*, 2001).

Atmospheric effects can give a bias to the underlying LST if not corrected for. There is an atmospheric window though, where atmospheric attenuation is minimised. This window of high transmission is in the spectral region 8-13μm. What is more, according to Wien's Displacement Law the peak of the Earth's spectral radiance at an ambient temperature of 300K occurs at approximately 9.6μm (Lillesand and Kiefer, 1987). Most TIR algorithms for retrieving LST thus usually operate in this 8-13μm spectral range (Dash *et al.*, 2002). Even so, attenuation at these wavelengths, which is caused by the presence of aerosols and by water vapour absorption, can still be significant. The most commonly applied operational approach to resolve this is the

generalised split-window algorithms (Becker and Li, 1990; Wan and Dozier, 1996), which solve two simultaneous equations for TOA brightness temperatures for channels at approximately 11μm and 12μm wavelengths, based on *a priori* knowledge of the surface emissivity from land cover classification. The rationale behind this is that atmospheric attenuation is a function of the differential absorption at each channel wavelength (Trigo *et al.*, 2008a). Both atmospheric effects and emissivity variability need to accounted for to avoid retrieval errors of up to 12K (Sobrino and Raissouni, 2000; Sobrino *et al.*, 2003).

Surface heterogeneity ensures that the validation of remotely sensed LST is a challenging undertaking. As such, most validation studies have focused on sites larger than a satellite pixel which are topographically flat and homogeneous in terms of surface cover, with only limited campaigns in heterogeneous environments (Soria and Sobrino, 2007; Trigo *et al.*, 2008a). In the context of Africa such homogeneous areas are hard to find, and are not representative of much of the continent. A relevant objective here then is to evaluate both model LST and satellite-derived LST in a heterogeneous landscape, with any such investigation also enhancing the status of operational remotely sensed products.

In this study, the uncertainty of LST simulated by the JULES model was evaluated with respect to *in situ* measurements taken in a mixed tree/grass landscape, and by way of a multi-temporal intercomparison over Africa with three satellite-derived LST products: the advanced along-track scanning radiometer (AATSR), the moderate resolution imaging spectroradiometer (MODIS), and the spinning enhanced visible and infrared imager (SEVIRI). The savannah field site is described, as is the protocol followed for the field exercise and intercomparison. A brief account of the individual

remote sensing products is given, with further details of the model functionality presented. Where biases were found, potential causes are discussed.

3.2. Materials and methods

3.2.1. Field site

A field campaign was undertaken to validate the model and satellite-derived LST against *in situ* measurements. Work was carried out at a field site (Figure 3.1; Figure 3.2, left) located in the 1,948,528ha Kruger National Park (KNP) in north-eastern South Africa from 23rd July 2009 to 7th August 2009. Centred on 25.10°S, 31.47°E, the field site is situated in the Skukuza region of the National Park, which is classified as semi-arid savannah of tropical grassland and fine-leaved trees (Scholes *et al.*, 2001). Since savannahs cover nearly 50% of the continent of Africa (Ciais *et al.*, 2009), the choice of field site is appropriate.

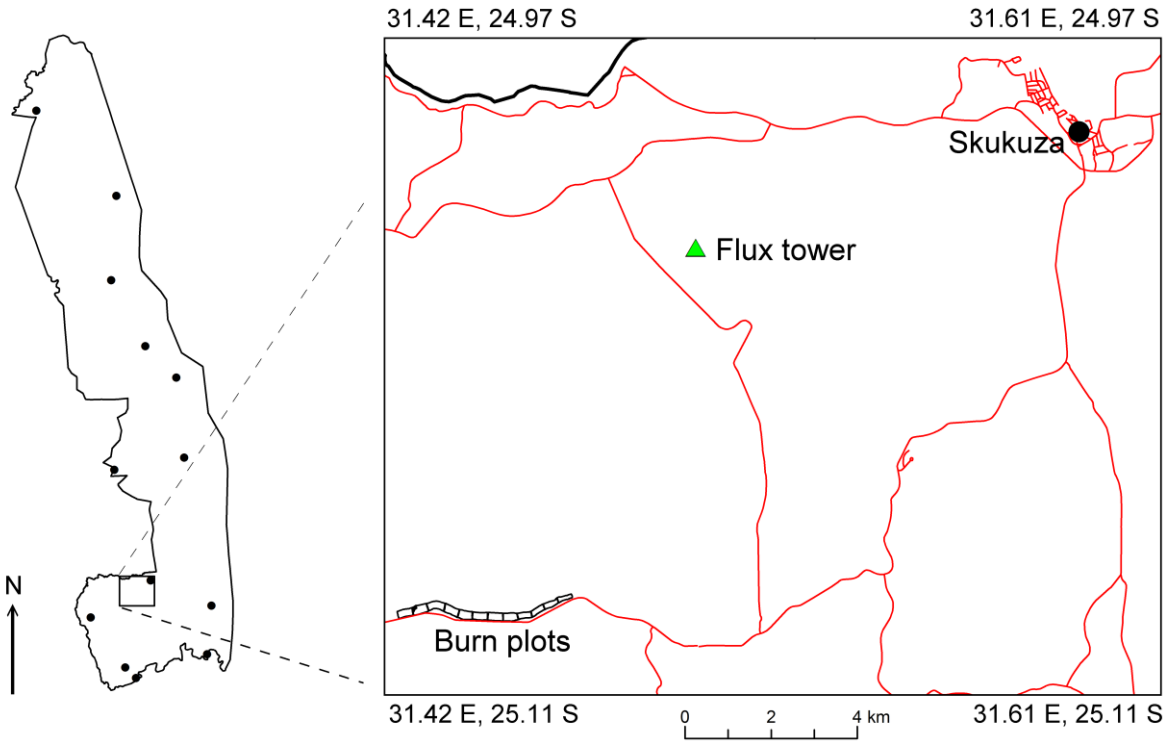

Figure 3.1: Location of the field site (labelled as burn plots) and Skukuza Flux Tower within the Kruger National Park in South Africa. The locations of the main rest camps are denoted, with Skukuza labelled.

Figure 3.2: Photographs illustrating a representative scene from the field site (left); and the Skukuza Flux Tower (right).

Figure 3.1 also highlights the location of the Skukuza Flux Tower (Figure 3.2, right) at 25.02º S, 31.50º E west-southwest of Skukuza, which has been delivering Eddy Covariance measurements since April 2000. Meteorological measurements for driving JULES during the field campaign period were acquired from this flux tower (Table 3.1). This was deemed an appropriate source of driving data as although located at a mean distance of approximately 10km from the field campaign site at a bearing of 19°, the assumption was made that meteorological measurements acquired from here would be more representative than the coarse resolution values utilised for the continental intercomparison.

The rationale behind the decision to undertake this exercise during the height of the southern African dry season was to maximise the probability of clear-sky conditions. Given that the field exercise was restricted to clear-sky conditions uncertainty in using the flux tower measurements was minimised, since one of the most spatially heterogeneous of the meteorological forcing variables is precipitation.

Table 3.1: Meteorological measurements acquired from the Skukuza Eddy Covariance Tower for driving the JULES model, detailing the instruments which acquire the measurements.

Variable	Instrument	Output Units
Air temperature	PT1000	°C
Precipitation	Tipping bucket	mm
Long-wave radiation	Pyranometer	W m^{-2}
Short-wave radiation	Pyranometer	W m^{-2}
Air pressure	Barometric pressure sensor	mb
Relative humidity	Capacity RH sensor	%
Wind speed	Cup anemometer	m s^{-1}
CO_2 mixing ratio	Infrared gas analyser	μmol mol^{-1}

The semi-arid subtropical climate of hot rainy summers and warm dry winters in conjunction with the biotic and abiotic controls on the energy, water and carbon balance (Table 3.2) support two distinct savannah communities: broad-leafed *Combretum* savannah; and fine-leafed *Acacia* savannah. Within the undulating landscape the shallow sandy soils of the ridges are dominated by nutrient-poor *Combretum* savannahs, with the clay soils of the lower slopes dominated by nutrient-rich *Acacia* savannahs (Scholes *et al.*, 2001).

Table 3.2: Field site biophysical characteristics; descriptions from [a]Scholes et al. (2001), [b]Barton et al. (1986), and [c]Low and Rebelo (1996).

Feature	Description
Altitude	370m[a]
Annual rainfall	550 ± 160mm[a]
Geology	Archaean granite rocks and gneiss of the Nelspruit suite[b]
Topography	Undulating landscape with ridge tops about 40m above the valley floor, and clay illuviation down the slopes to drainage lines approximately 3km apart[a]
Vegetation	Mixed lowveld bushveld[c]

3.2.2. Model dynamics

The JULES model explicitly treats the energy exchanges between the land and the atmosphere for each tile; unlike single-source models, which can generate uncertainties as they attempt to predict surface heat fluxes from mixed soil / canopy layers (Kustas and Norman, 1996). LST (T_{sfc}) is a key factor in the surface energy balance equation of each tile, which is defined by Cox *et al*. (1999) as:

$$SW_N + LW_{\downarrow} - \sigma T_{sfc}^{4} = H + LE + G_0 \quad (9)$$

Where SW_N is the net downward short-wave radiation derived from the surface albedo, $LW_{\downarrow}$ is the downward long-wave radiation, σ is the Stefan–Boltzmann constant, H is the sensible heat flux, LE is the latent heat flux, and G_0 is the heat flux into the ground. The grid-box LST is an aggregation of the individual tile surface temperatures, in which the tile surface temperatures multiplied by their respective fractional covers within the grid box are summed together to generate an overall grid-box surface temperature.

3.2.3. Remotely sensed LST products

Three commonly used satellite-derived LST products from TIR retrievals were compared with *in situ* measurements and with one another as part of the continental intercomparison exercise: AATSR, MODIS, and SEVIRI. To my knowledge, this is the first attempt to validate all three of these remotely sensed LST products in a mixed tree/grass savannah landscape.

The AATSR instrument on board the sun-synchronous, polar orbiting satellite Envisat at an altitude of approximately 800km is the latest in the along-track scanning radiometer (ATSR) family. Together with ATSR-1 and ATSR-2 on board the European

remote sensing satellites (ERS): ERS-1 and ERS-2 respectively, there is the potential for a long-term LST record spanning nearly 20 years. What is unique about AATSR is that it is able to determine TOA brightness temperatures from two distinct viewing perspectives: forward (approximately 55° from zenith) and nadir. While retrievals from both are a feature of the sea-surface temperature datasets, only the nadir view is processed for land surface retrievals. The 512km swath width of AATSR allows for global 1km pixel LST coverage every 3 days with overpasses at approximately 10:00 local solar time; the repeat cycle is 35 days. Here, the level-2 product ATS_NR__2P was used, which employs a split-window algorithm based on the 11μm and 12μm channels to provide calibrated TOA brightness temperatures converted to LST; whereby regression coefficients depend on 14 land cover classes, precipitable water, and the fraction of vegetation cover (Prata, 1993; Prata, 1994). The cloud clearing algorithm uses the 1.6μm near-infrared (NIR) channel to identify cloud affected pixels, in which identification is attempted by applying a series of tests to the brightness temperature. AATSR has on board calibration with good radiometric accuracy of less than 0.1K, where the target accuracy for retrievals during the day is 2.5K and during the night is 1.0K (Llewellyn-Jones *et al.*, 2001). In the validation study by Noyes *et al*. (2007), the uncertainty during the day was approximately 1.0K. A full description of the AATSR LST retrieval algorithm can be found in the product user manual which is accessible from the Envisat web site (http://envisat.esa.int/).

The SEVIRI instrument is the main payload on board the Meteosat Second Generation (MSG) geostationary satellites, which fly at an altitude of approximately 36000km above the equator. An image is acquired every 15 minutes, with the pixel size a function of the viewing angle. For the African continent, this equates to pixel sizes between 3km and 5km. LST retrieval is a more challenging undertaking than for the

polar-orbiting satellites, particularly at higher latitudes, as a result of increased atmospheric attenuation due to higher viewing zenith angles. A generalised split-window algorithm is used to estimate LST as a linear function of TOA brightness temperatures for the 10.8μm and 12μm channels, in which surface emissivity depends on land cover classes and the fraction of vegetation cover (Peres and DaCamara 2005; Trigo *et al.*, 2008b). The LST products are generated and disseminated by the Satellite Application Facility on Land Surface Analysis (LandSAF). They use cloud masking software developed by the Nowcasting and Very Short-Range Forecasting Satellite Application (http://www.nwcsaf.org) to identify clear sky pixels. Validation of LST retrievals indicates a bias free algorithm, with increasing random errors as a response to increasing viewing zenith angles (Trigo *et al.*, 2008a), in which the accuracy for most simulations between nadir and 50° viewing zenith angle can be potentially as low as 1.5K (Sobrino and Romaguera, 2004). The product user manual provides a comprehensive description of the LST retrieval algorithm, and can be accessed from the LandSAF web site (http://landsaf.meteo.pt/).

MODIS instruments are part of the payload of two sun-synchronous, near-polar orbiting satellites, Terra and Aqua. The large swath width of these instruments, 2330km, enables each satellite to provide a pair of observations globally every day. Terra retrievals correspond to approximately 10:30 local solar time in descending mode, and approximately 22:30 local solar time in ascending mode; the retrieval times for Aqua are 01:30 and 13:30 local solar time. Here, only version-5 of the daily 1km level-3 LST product MOD11A1 acquired from Terra was used, since meaningful intercomparison between Aqua retrievals and AATSR retrievals could not be achieved due to a mismatch in local overpass times. LST is estimated using the generalised split-window algorithm of Wan and Dozier (1996) as a linear function of TOA brightness

temperatures for bands 31 (11μm) and 32 (12μm), in which surface emissivity is dependent on land cover class and a linear correction for the satellite viewing angle (Wan *et al.*, 2002). The cloud masking algorithm used in version-5 includes refinements to account for surface elevation in an attempt to minimise the significant cloud contamination symptomatic of earlier versions, resulting in a reported accuracy better than 1.0K (Wan, 2008). Full details of MODIS LST retrieval is provided in the user manual, which is available from http://www.icess.ucsb.edu/modis/LstUsrGuide/.

3.2.4. In situ validation theory

For *in situ* measurements made at the surface of the earth the radiative transfer equation can be expressed as:

$$B_c(T_c) = \varepsilon_c B_c(T_{sfc}) + (1 - \varepsilon_c)\, B_c(T_{sky}) \tag{10}$$

Where $B_c(T_c)$ is the measured radiance given by the Planck function for effective brightness temperature T_c in the radiometer channel c, $B_c(T_{sfc})$ is the emitted surface radiance given by the Planck function for surface temperature T_{sfc} in channel c, and $B_c(T_{sky})$ is the down-welling atmospheric radiance given by the Planck function for effective brightness temperature T_{sky} of the atmosphere; ε_c is the emissivity of the Earth's surface in channel c. The non-uniformity of the surface emissivity means that the down-welling atmospheric radiance has a small, but significant impact on LST, so regular radiometric measurements of this correction factor are important, particularly if the sky is not homogeneous. In practice, this is carried out with a radiometer facing the sky at approximately 53° from zenith (Kondratyev, 1969; Coll *et al.*, 2005).

The spatial resolution of most satellite-derived LST is low compared with the heterogeneity of LST on the ground, so T_{sfc} at the scale of a satellite pixel is the average

surface temperature of weighted means of the surface temperatures of the principal land cover scenes (Kerr *et al.*, 1992; Soria and Sobrino, 2007):

$$T_{sfc} = \sum_{i} W_{(i)} T_{sfc(i)} \quad (11)$$

Where $W_{(i)}$ is the weight (or fractional cover) of the respective land cover type, and $T_{sfc(i)}$ is the surface temperature of land cover type *i*, with *i* corresponding to one of the principal land cover types (or endmembers) most representative of the field site.

3.2.5. Field methodology

In theory, the strong spatial and temporal variability of LST should impose an approach whereby simultaneous *in situ* measurements are made at every point over the surface encompassing a satellite pixel at the exact time of the satellite overpass. However, this approach is not possible in practice, and so a feasible alternative (Trigo *et al.*, 2008a) is to take simultaneous *in situ* measurements over the principal land cover types which constitute the satellite pixel at the overpass time. Here, concurrent radiometric measurements under clear-sky conditions were made over the three principal surface types – bare soil, grass and tree canopy – to coincide with each satellite overpass; this limitation of three principal types was imposed by the number of available radiometers.

For each overpass, three scenes on the ground were measured using three Apogee SI-121 infrared radiometers (labelled 1283, 1288 and 1291). Each radiometer had a spectral response of 8-14μm and a field-of-view (FOV) of 18°. All measurements were carried out within the recommended temperature range for operation of -55°C to 80°C, with radiometric accuracy quoted by the manufacturer as ±0.2°C between operating temperatures of -10°C to 65°C. The brightness temperature of each scene was measured with a 1-second periodicity, and every minute these measurements were averaged and

recorded, with the first and last average discarded to discount anomalous measurements at the beginning and end of the measurement window. Each radiometer was angled to give nadir readings and fixed to a tripod by way of a horizontal arm (Figure 3.3) to maximise stability.

Figure 3.3: Photograph illustrating the typical field setup of an Apogee SI-121 infrared radiometer. The radiometer is attached to the end of the horizontal arm of the tripod, pointing towards the ground at nadir.

Care was taken to ensure neither the tripod legs nor the operator's shadow intersected with the FOV. To measure the tree canopy, the height of the associated tripod was extended and the radiometer positioned over trees with a height up to 1.5m. Besides the explicit uncertainty of the Apogee SI-121 radiometers, the radiation seen by the instruments is subject to a scaling factor as the FOV-derived target footprint captures only 98% of the emitted radiation. Since only the mean temperature across the footprint is recorded, if a temperature gradient exists across the footprint then the scaling factor overlooks this. Before and after each overpass, measurements of down-welling atmospheric radiance were made by angling one of the radiometers towards the

sky at approximately 53° from zenith. Values of ε_c required for equation (10) were obtained from the advanced spaceborne thermal emission and reflection radiometer (ASTER) spectral library (Baldridge *et al.*, 2009) corresponding to the surface type of the measured scene (Table 3.3).

Table 3.3: Emissivities in the 8-14μm spectral range corresponding to the spectral response of the Apogee SI-121 infrared radiometers. Endmember emissivities were obtained from the ASTER spectral library (Baldridge et al., 2009) for surface types representative of the measured scenes: dry grass; deciduous trees; and red-orange sandy soil.

Endmember	**Emissivity ± σ**
Grass	0.940 ± 0.023
Trees	0.977 ± 0.004
Bare soil	0.941 ± 0.034

During the field campaign *in situ* radiometric measurements for all three endmember classes were acquired each morning to coincide with the morning overpasses of AATSR and MODIS, and also every 15 minutes to coincide with SEVIRI retrievals. For this *in situ* exercise the MODIS 1km level-2 product was used, MOD11_L2. The overpass times for AATSR and MODIS were predicted using the NASA LaRC Satellite Overpass Predictor (http://www-angler.larc.nasa.gov/cgi-bin/predict/predict.cgi). The presence of dangerous game animals enforced the limitation of daylight field work only, which meant that measurements of all three endmembers during the Terra MODIS night overpass were not possible. While two radiometers were mobile, one of the three radiometers was placed in the field with protection against animal interference for the entire duration of the campaign collecting diurnal measurements over a representative bare soil scene. This radiometer was encased in polystyrene along its shaft to prevent non-linear internal temperature

differences. Each day simultaneous measurements of this bare soil scene were acquired from all three radiometers in order to compare the calibrated measurements from each instrument.

3.2.6. Supervised classification

In order to compare the measurements acquired in the field with those obtained from EO satellites and simulated by the JULES model, weighted averages of the brightness temperatures for the three endmembers were calculated as per equation (11). The weight assigned to each endmember was determined, following the methodology of Soria and Sobrino (2007) and Trigo *et al*. (2008a), by means of a maximum likelihood supervised classification on the 4-m multispectral bands of an IKONOS image of the field site which were 'pan-sharpened' using the 1-m panchromatic band (Figure 3.4). The endmember proportions for each satellite pixel (Table 3.4) were derived from superimposing an overstrike of the pixels (denoted as AATSR-1, AATSR-2, MODIS-1, MODIS-2, MODIS-3, and SEVIRI) onto the classified image (Figure 3.5).

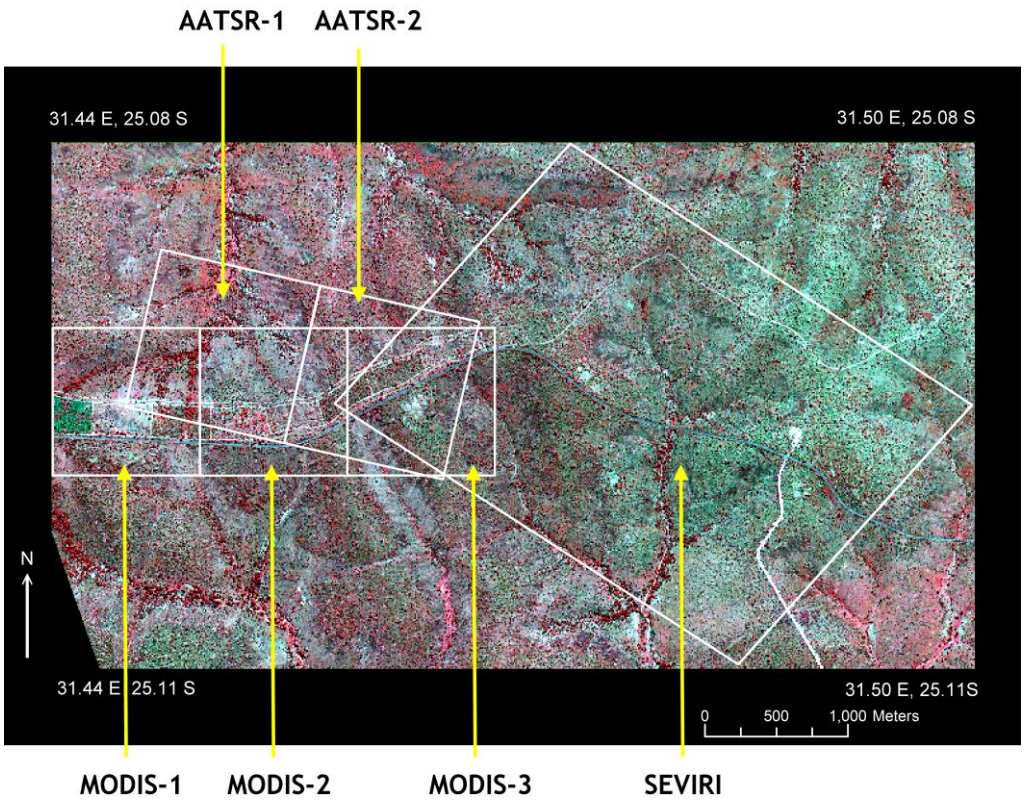

Figure 3.4: False colour composite covering the field site of the IKONOS 4-m multispectral image 'pan-sharpened' with the 1-m panchromatic band. An overstrike of the satellite pixels for AATSR, MODIS, and SEVIRI is indicated. Note that the area encompassing the SEVIRI pixel is also the area modelled by JULES.

Table 3.4: Proportions of the three endmember classes for each satellite pixel; the endmember proportions for JULES were the same as for SEVIRI. Percentages were obtained as a result of a supervised classification of a 'pan-sharpened' multispectral IKONOS image covering the field site.

Pixels	**Endmember proportions (%)**		
	Bare soil	**Trees**	**Grass**
AATSR-1	23.48	21.36	55.16
AATSR-2	28.20	23.20	48.60
MODIS-1	26.57	23.17	50.26
MODIS-2	27.01	19.56	53.43
MODIS-3	30.12	21.68	48.20
SEVIRI / JULES	22.21	14.28	63.51

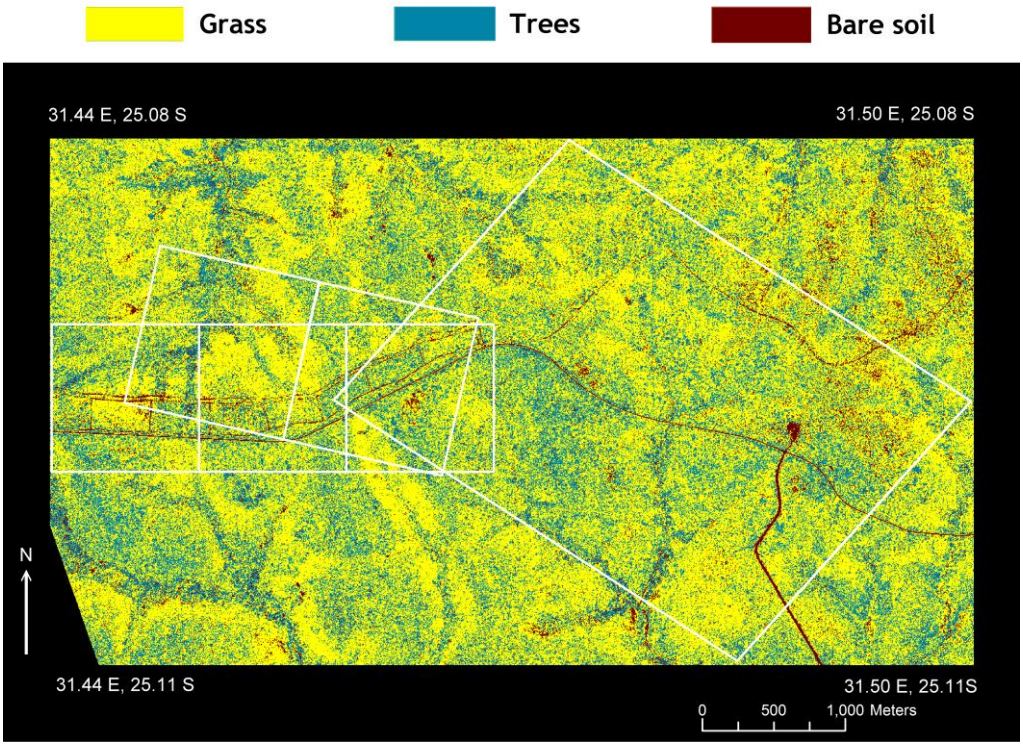

Figure 3.5: Maximum likelihood supervised classification of the 'pan-sharpened' multispectral image. The three endmember classes are indicated: bare soil (brown); grass (yellow); and trees (blue). An overstrike of the satellite pixels for AATSR, MODIS, and SEVIRI is indicated (white polygons).

The IKONOS image, which was acquired on 21st April 2005 and which displays no detectable cloud cover, encompasses a set of experimental burn plots (EBPs) bounded by fire breaks. GPS measurements of the corners of the burn plots taken during the field campaign were compared with the geolocation of the same points in the imagery - which as a result were found to be good. Training sets for the supervised classification were created by way of a survey of the field site, in which small homogeneous areas of the three endmembers were identified and supported with GPS readings. On closer inspection the IKONOS image reveals the presence of riparian systems, whereas water bodies were not considered as endmembers. It should be noted though, that at the time of the field campaign these riverbeds were dry, and so were classified as bare soil. In

the case of the JULES model, land cover proportions were taken as the endmember proportions for the SEVIRI pixel.

3.2.7. Model experimental setup

As stated in section 3.2.6., to enable comparison of field measurements with model simulations of LST, tile percentages in the JULES model were determined from the proportions of the three endmembers. In practice, the proportion of bare soil endmember was assigned to the JULES surface type of bare soil; the grass proportion was assigned to the JULES surface types of C_3 and C_4 grasses, with the split between them being determined from the ISLSCP II dataset of C_4 fractions; and the tree proportion was assigned to the JULES surface type of broadleaf trees.

JULES was run as a single 'point' with a 30 minute time-step for the duration of the field campaign uncoupled from TRIFFID, as it was considered too short a time interval to trigger significant vegetation-climate feedbacks as a result of changes to vegetation distribution. Prior to the main run, the model was spun-up according to section 2.2.3, in which the model was forced with climate from the first 10-days of the field campaign repeatedly until soil moisture and soil temperature were equilibrated. CO_2 concentrations and meteorological measurements were acquired from the Skukuza Eddy Covariance Tower at 30 minute intervals. In the case of downward long-wave radiation, the pyranometer measuring this has not been operational since 2005, and so bilinearly interpolated NCEP Reanalysis II data (Kalnay *et al.*, 1996) was instead used for this variable. Finally, soil characteristics (Scholes *et al.*, 2001) typical of this landscape were used to parameterise the subsurface of the model (Table 3.5).

Table 3.5: Soil parameters obtained from Scholes et al. (2001) and applied in the JULES model are broadly representative of the surrounding landscape, rather than being an exact parameterisation of the field campaign site. Field capacity is the moisture content at θ -33 kPa tension, and the wilting point is the water content at θ -1500 kPa tension.

Depth (mm)	**Sand (%)**	**Silt (%)**	**Clay (%)**	***K* sat (µm/s)**	**Field capacity (v/v)**	**Wilting point (v/v)**
0–300	69	6	25	0.52	0.20	0.10
300–600	65	3	32	0.01	0.21	0.11

3.2.8. Instrument calibration

Calibration of the three Apogee SI-121 radiometers was not carried out prior to the field campaign due to the unavailability of a blackbody. As such, the radiometers were set up in accordance with the manufacturer supplied calibration coefficients. Post-calibration was carried out in the Physics laboratories at the University of Leicester with the use of a ramping blackbody (Figure 3.6) from Leicester and thermometry courtesy of the Rutherford Appleton Laboratory, Oxford.

Figure 3.6: Photographs of the ramping blackbody illustrating the radiometer pointing towards the black coated cavity (left), and the top-down view of the insulating structure (right). Photographs courtesy of T. Trent, Department of Physics and Astronomy.

The blackbody consisted of a copper cavity, which is painted black to enforce an emissivity as close to one as possible, encased within an insulated structure. This structure was filled with an ice and water mixture above the level of the cavity, and the temperature of the mixture was gradually raised with a heating element, ensuring as even a temperature as possible was maintained at any one moment in time throughout the insulated structure by continually circulating the mixture with an electric pump.

The surface temperature of the cavity was measured with a radiometer pointing towards the black coated outer surface, and *in situ* with a platinum resistance thermometer (PRT), with a manufacturer quoted accuracy of ±0.01°C. A diagrammatic representation of the experimental setup is illustrated in figure 3.7. An experiment was carried out whereby the heating element raised the temperature of the mixture over a period of two hours. At five minute intervals the temperature of the blackbody was sampled from both the radiometer and the PRT. A linear regression equation was determined between the radiometer measurements and the PRT measurements covering the temperature increase.

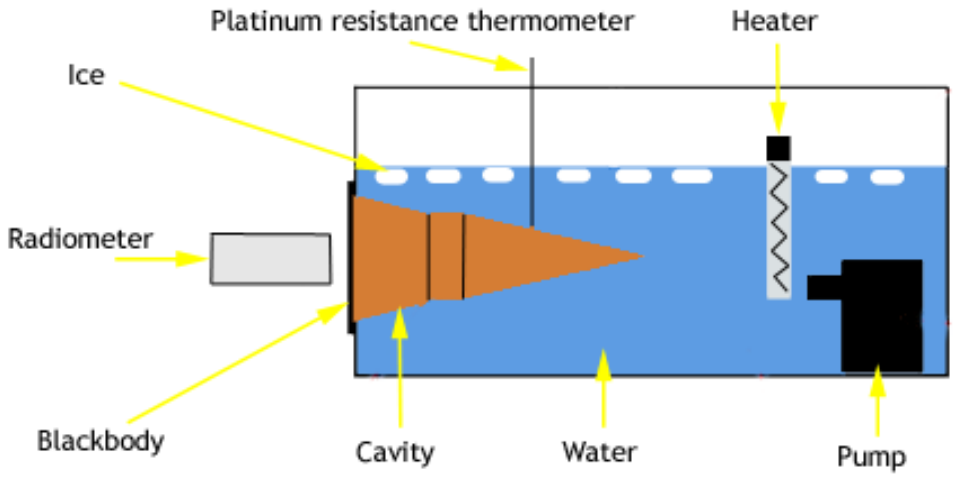

Figure 3.7: Diagrammatic representation of the ramping blackbody experimental setup.

This calibration equation was verified by repeating the experiment with the calibration equation applied directly to the recorded radiometric measurements. The whole experiment was repeated for the remaining two radiometers. Calibration equations (12, 13 and 14), where x is the original radiometric measurement and y is the calibrated measurement, were derived; figures 3.8 to 3.10 illustrate the effect of applying these equations to the original measurements in the context of the blackbody experiments.

$$y = 0.94x + 16.88 \quad (12)$$

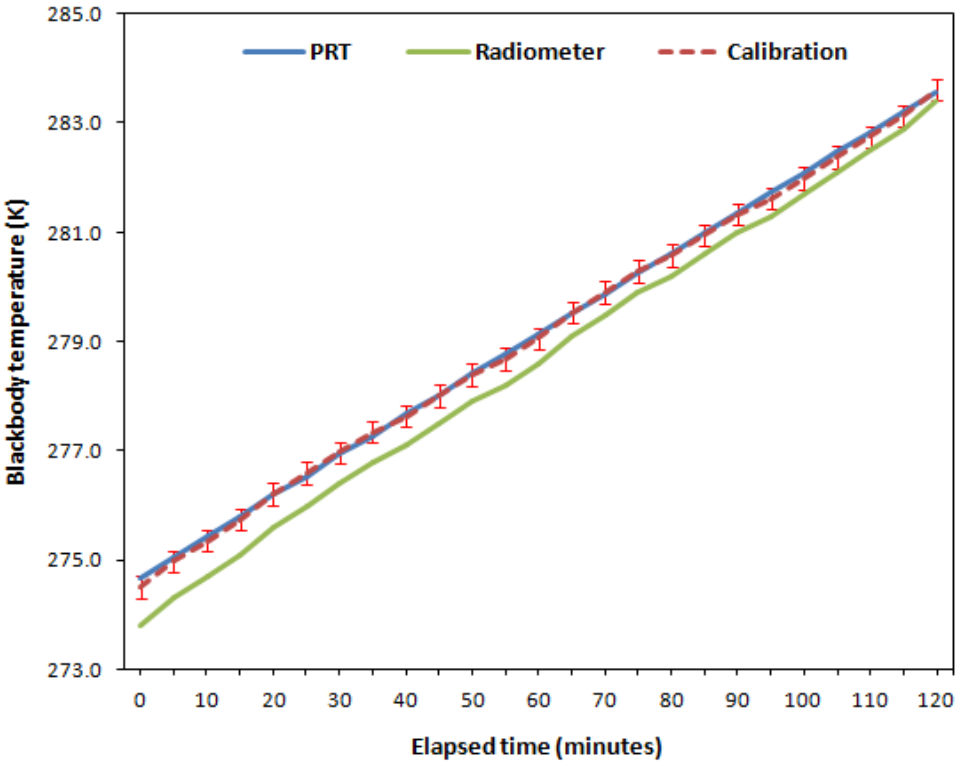

Figure 3.8: Time series for the calibration experiments illustrating the temperature of the blackbody as recorded by the platinum resistance thermometer (PRT), and radiometer 1283. The calibration line is the result of applying calibration equation 12 to the radiometric measurements. The error bars represent the radiometric accuracy of ±0.2°C for the Apogee SI-121 radiometers.

$$y = 0.90x + 28.53 \quad (13)$$

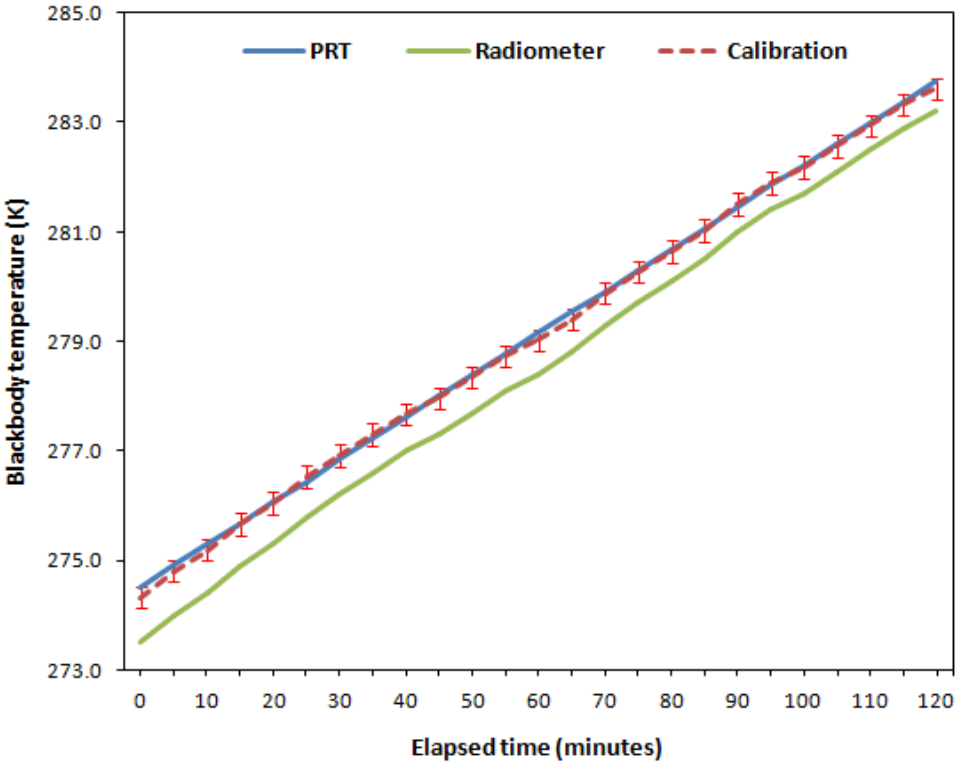

Figure 3.9: Time series for the calibration experiments illustrating the temperature of the blackbody as recorded by the platinum resistance thermometer (PRT), and radiometer 1288. The calibration line is the result of applying calibration equation 13 to the radiometric measurements. The error bars represent the radiometric accuracy of ±0.2°C for the Apogee SI-121 radiometers.

$$y = 0.91x + 26.28 \quad (14)$$

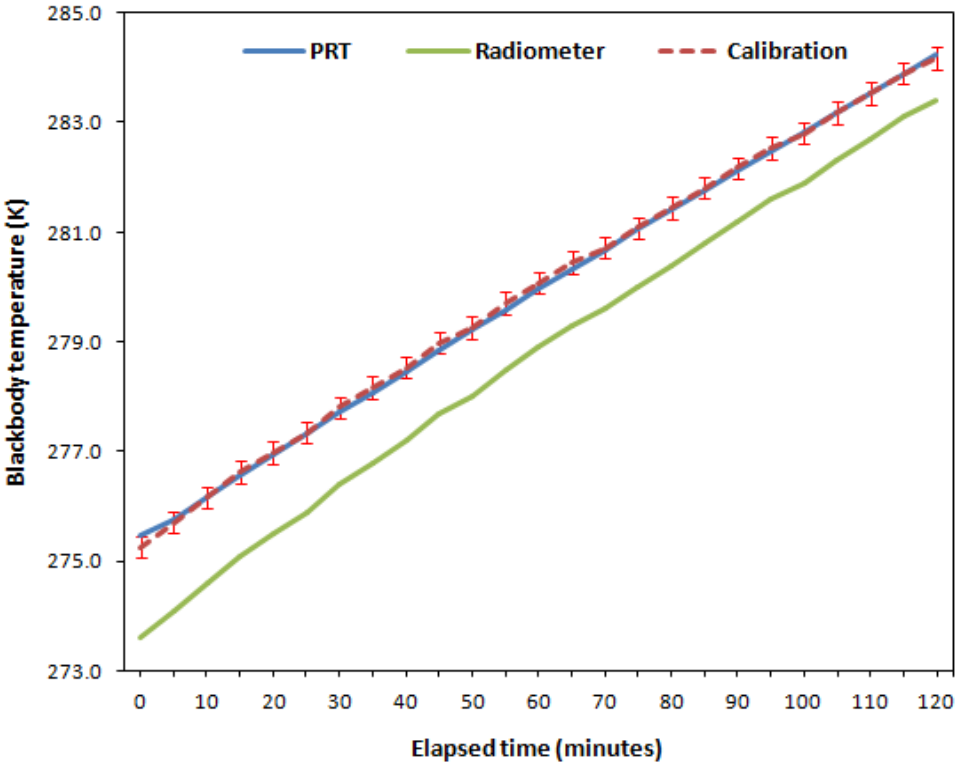

Figure 3.10: Time series for the calibration experiments illustrating the temperature of the blackbody as recorded by the platinum resistance thermometer (PRT), and radiometer 1291. The calibration line is the result of applying calibration equation 14 to the radiometric measurements. The error bars represent the radiometric accuracy of ±0.2°C for the Apogee SI-121 radiometers.

Equations (12, 13 and 14) were applied to the radiometric measurements taken by radiometers (1283, 1288 and 1291) respectively during the field campaign. Indeed, *in situ* measurements from all three radiometers of the fixed bare soil scene following the application of the calibration equations were comparable - within the ±0.2°C manufacturer quoted accuracy of the instruments.

3.2.9. Intercomparison analysis

For this exercise, much of the experimental setup of the JULES model mirrored that which has been described in 2.2.3. For instance, the source of each driving dataset remains the same as detailed in table 2.1. The principal difference here was that the model was only run for a single year, 2006; and the spin-up cycle was a repetition of the years 2001-2005. Simulated LST from JULES was compared with LST retrieved from AATSR, MODIS and SEVIRI during the months of March, June, September and December of 2006 for the whole of the African continent. These four months were examined to increase the likelihood of any seasonal differences between the different sources being brought to light.

In order to compare LST from the different sources the retrievals from satellite were re-projected to a regular 1° × 1° grid, to match the JULES output, by averaging geo-referenced pixels within each grid-box. Clouds scatter and absorb infrared radiance, and so to minimise cloud contamination only satellite pixels identified as cloud-free having the highest quality control flags were included in the re-projection. Comparing different LST datasets can be challenging prospect because of the variability of LST over brief time periods (Pinheiro *et al.*, 2006a). Here, intercomparison was performed at individual 1° grid boxes only when an AATSR overpass time intersected with a MODIS overpass time within a ±10 minute time window. These were compared with the closest 15-minute SEVIRI retrieval, and the closest 30-minute JULES simulation. Monthly composites of the differences between the LST sources were generated from the aggregation of all the individual grid-box comparisons carried out during the month. These were categorised into ‘day’ (approximately 07:00 - 12:00 UTC) and ‘night’ (approximately 19:00 - 24:00 UTC) observation windows, as these correspond to the Terra MODIS orbital overpass times for Africa.

3.3. Results

3.3.1. In situ study

Figure 3.11 shows both modelled LST and the individual satellite retrievals plotted against the LST observations collected *in situ* over a heterogeneous landscape of KNP during local morning between 23rd July and 7th August 2009.

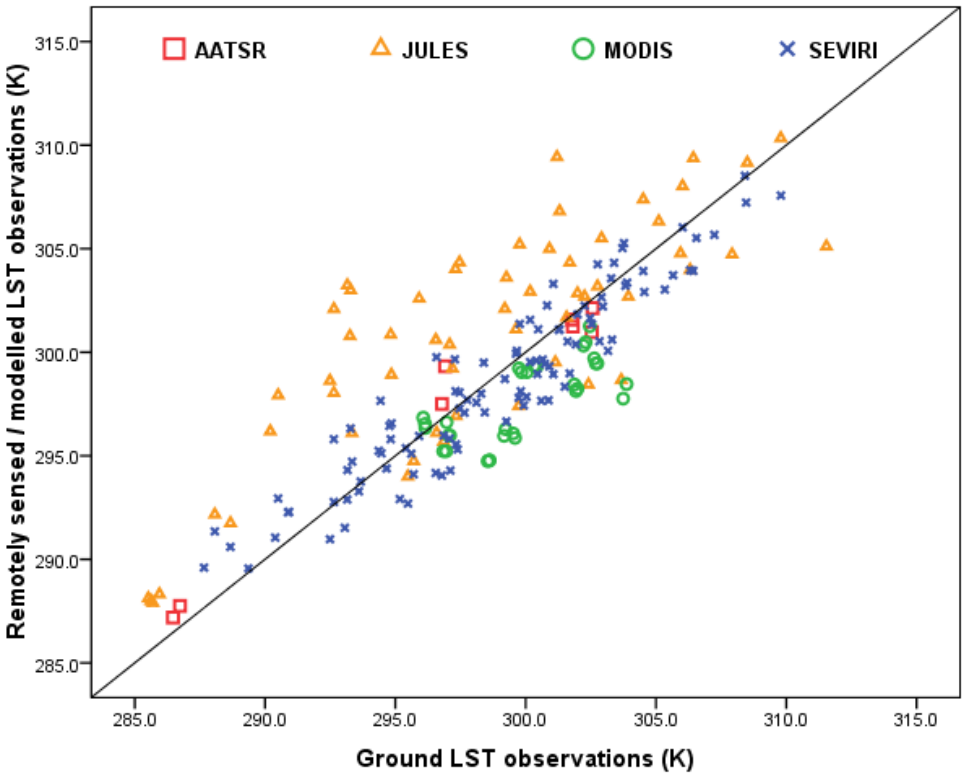

Figure 3.11: Remotely sensed and model simulated LST vs. in situ observations taken during local morning in the Kruger National Park, South Africa, between 23rd July and 7th August 2009.

What is evident is that both AATSR and SEVIRI retrievals are clustered relatively evenly above and below the line of equality between ground observations and remotely sensed observations. In the case of AATSR, seven of the eight retrievals are within ±1.50K of the corresponding ground measurements. The biases for SEVIRI retrievals are slightly larger, but still range within ±3.20K of the ground observations. For MODIS, almost all of these retrievals display a negative bias, peaking at -5.98K,

when compared with field measurements for the corresponding pixels. In contrast, the majority of simulated LST values from JULES have a positive bias with respect to the corresponding ground observations. What is more, the spread of bias is the greatest of the four LST sources, with a maximum of 10.07K and minimum of -6.43K.

If we consider the overall statistics of this exercise (Table 3.6), we see that the model displays the largest bias with respect to the ground observations, with a standard deviation twice as large as any of the satellite-derived LST products. Of the EO sources, AATSR was found to be the most accurate, with an overall mean bias of 0.26K. Such a small bias is consistent with previous studies comparing AATSR retrievals with ground observations (Coll *et al.*, 2006; Noyes *et al.*, 2006; Noyes *et al.*, 2007), in which the mean biases found in these studies were all between ±1.0K. The root mean square error (RMSE) of 1.17K for AATSR is comparable with the 1.7K quoted by Soria and Sobrino (2007) from their validation study over heterogeneous fields in Morocco. The uncertainty found here of 1.21K is also within the 2.5K (Llewellyn-Jones *et al.*, 2001) daytime target accuracy for retrievals. With respect to SEVIRI, the negative mean bias of -0.38K is smaller than found in other studies (Kabsch *et al.*, 2008; Trigo *et al.*, 2008a), and the uncertainty of 1.65K is within the 2.0K target accuracy for retrievals set down by LandSAF. Finally, the largest mean bias and standard deviation exhibited by a satellite-derived LST product was that of MODIS. Although within the range (-1.8K to -4.0K) of numerous studies (Bosilovich, 2006; Noyes *et al.*, 2006; Trigo *et al.*, 2008a), the uncertainty of 1.67K is outside the 1.0K accuracy reported by Wan (2008), and emphasises the importance of ongoing evaluation of remotely sensed LST products.

Table 3.6: Comparison between LST from both remotely sensed products and the JULES model, and in situ observations taken from the field site in KNP. Bias, σ (standard deviation) and root mean square error (RMSE) correspond to the modelled and remotely sensed LST with respect to the in situ measurements corresponding to the respective pixel locations.

Source	**Bias (K)**	**σ (K)**	**RMSE (K)**
AATSR	0.26	1.21	1.17
MODIS	-2.24	1.67	2.77
SEVIRI	-0.38	1.65	1.68
JULES	2.48	3.69	4.41

3.3.2. Intercomparison

Figures 3.12 to 3.15 illustrate the spatial differences between each source of LST data and a single reference source, in this case SEVIRI, for monthly 'day' composites during the four periods, March, June, September and December of 2006. These figures contain image gaps due to insufficient intersecting observations available for some grid-boxes to construct monthly composites. What can be discerned however, is that AATSR LST is most comparable with SEVIRI LST, whereas both MODIS and JULES produce LST with a consistent negative difference with respect to SEVIRI (and for that matter AATSR). This negative difference follows a different pattern for MODIS and JULES; and in the case of MODIS, this would seem to largest over the savannah landscapes of Africa. The choice of these four specific months was made to highlight any seasonal differences between the distinct sources of LST, and indeed some clear variations are apparent. For instance, MODIS retrieved lower LST, with respect to SEVIRI, over the northern savannahs in June, whereas during December it was over the southern savannahs where this difference was strongest. Furthermore, over northern Africa SEVIRI is retrieving the highest temperatures over much of the comparison period; whereas over southern Africa both AATSR and JULES retrieved slightly higher

temperatures during December, and over much of the comparison period AATSR retrieved the highest temperatures. Indeed, continent-wide the source of highest mean temperatures was AATSR. This finding is consistent with that of Noyes *et al*. (2006) in their study across ten sites in Europe and North Africa. They also found SEVIRI to systematically record higher LST than MODIS; as did Trigo *et al*. (2008a) in their study over Central Africa and the Iberian Peninsula. Again this is consistent with the findings presented here, with the MODIS viewing angle primarily responsible. The negative difference of MODIS with respect to SEVIRI increases with the size of the viewing angle, probably as a result of differential heating rates between sunlit and shadow scenes, as was postulated by Trigo *et al*. (2008a). SEVIRI on the other hand, observes predominantly sunlit scenes.

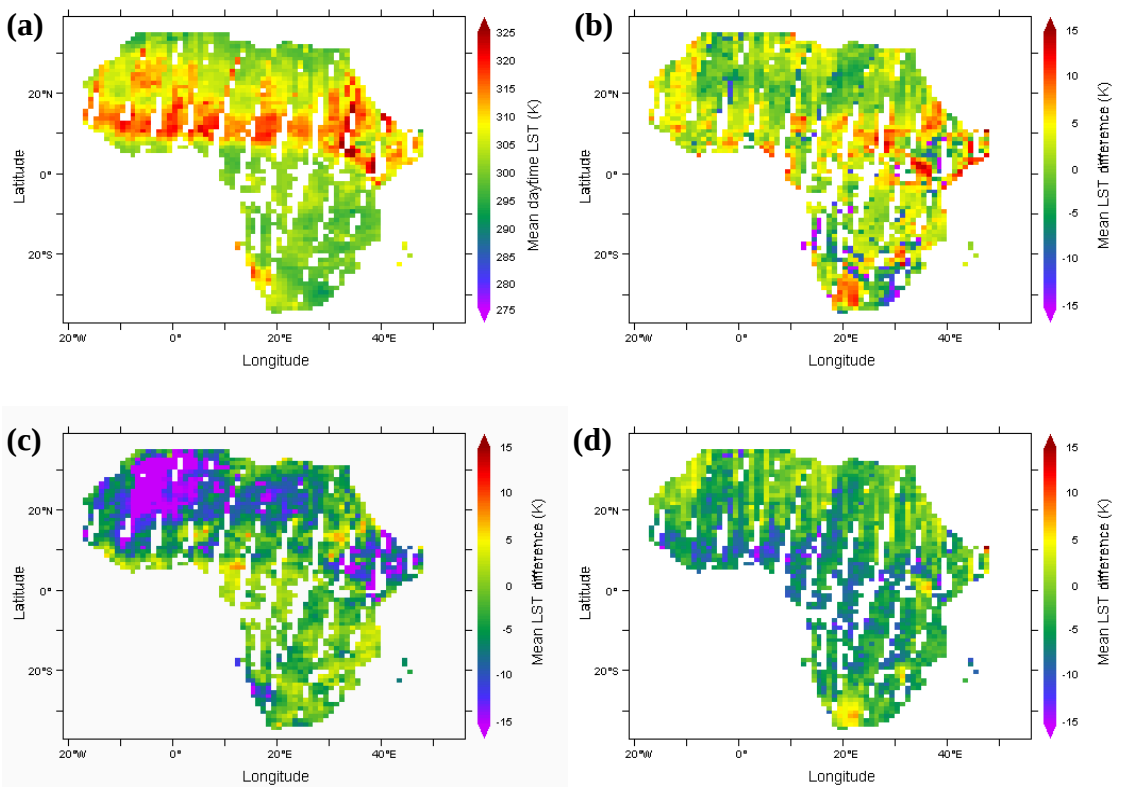

Figure 3.12: Mean 'daytime' LST (approximately 07:00 - 12:00 UTC) for March 2006 retrieved from SEVIRI (a) displayed in absolute units; and AATSR minus SEVIRI (b); JULES minus SEVIRI (c); and MODIS minus SEVIRI (d) over Africa. The monthly composites are based on temporal retrievals when both AATSR and MODIS overpass times coincided within a ±10 minute tolerance; with the nearest 15-minute SEVIRI retrieval and the nearest 30-minute JULES simulation being applied. Figure reproduced from Ghent et al. (2010).

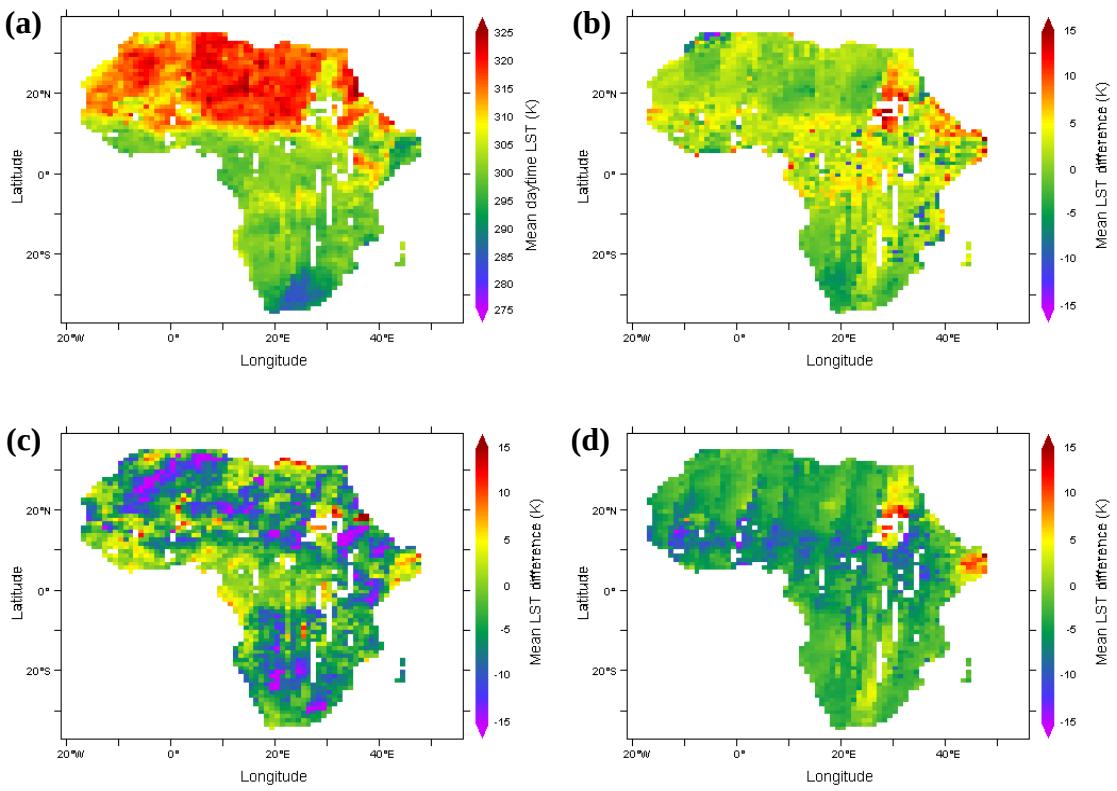

Figure 3.13: Mean 'daytime' LST (approximately 07:00 - 12:00 UTC) for June 2006 retrieved from SEVIRI (a) displayed in absolute units; and AATSR minus SEVIRI (b); JULES minus SEVIRI (c); and MODIS minus SEVIRI (d) over Africa.

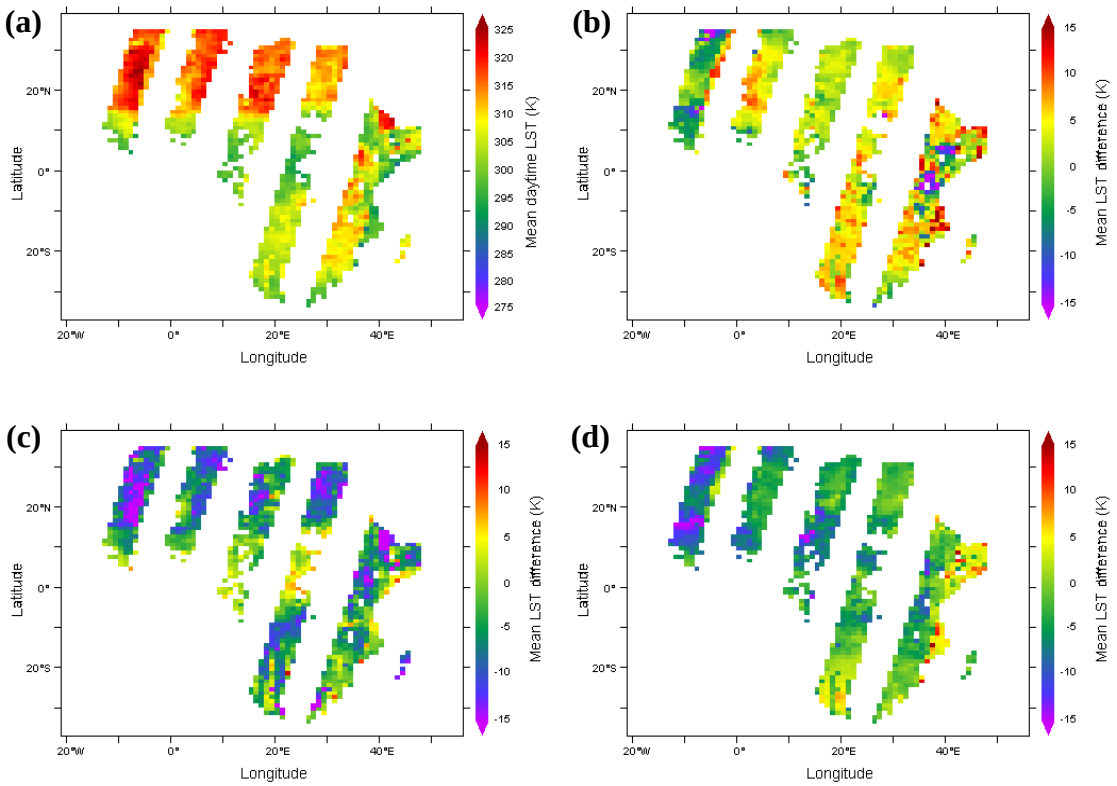

Figure 3.14: Mean 'daytime' LST (approximately 07:00 - 12:00 UTC) for September 2006 retrieved from SEVIRI (a) displayed in absolute units; and AATSR minus SEVIRI (b); JULES minus SEVIRI (c); and MODIS minus SEVIRI (d) over Africa.

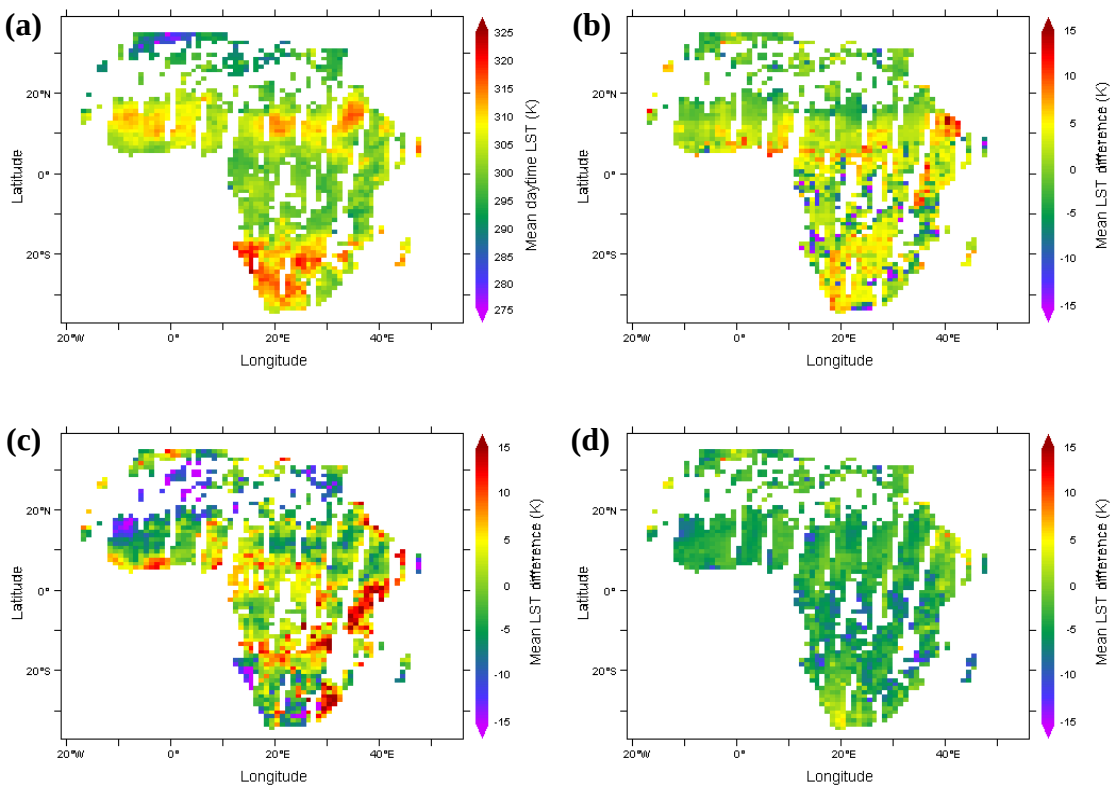

Figure 3.15: Mean 'daytime' LST (approximately 07:00 - 12:00 UTC) for December 2006 retrieved from SEVIRI (a) displayed in absolute units; and AATSR minus SEVIRI (b); JULES minus SEVIRI (c); and MODIS minus SEVIRI (d) over Africa.

If we now consider LST modelled by JULES, it would seem from figures 3.12 to 3.15 that the model consistently underestimates surface temperatures with respect to satellite-derived sources; this appears to be most pronounced over barren or sparsely vegetated regions, such as the Sahara. One possible cause of this difference is the way in which LST is aggregated across a grid-box. In JULES, grid-box LST is a linear combination of the individual tile surface temperatures weighted by their corresponding fractional covers. In any multiple-source model though, grid-box surface temperature should be defined as the fourth root of the aggregation of the fourth power of component surface temperatures multiplied by their corresponding fractional covers (Norman *et al.*, 1995; Li *et al.*, 2005). However, while this may rationalise some of the discrepancy in multiple tiled grid-boxes, this does not provide a satisfactory explanation

for the large difference observed over barren or sparsely vegetated regions, which are almost exclusively composed of grid-boxes with single tile components; in which case no tile aggregation is made. In these bare soil grid-boxes it was instead suspected, that the primary candidate for the model underestimation was poor soil parameterisation. This is a logical suspicion, since in JULES the surface temperature of bare soil is quantified not only from the surface energy balance equation, but also from the soil temperature of the topmost layer in the soil profile.

To investigate this possibility further, the intercomparison experiment between JULES and the satellite-derived sources of LST was repeated under a modified soil parameterisation (denoted as parameterisation-B; henceforth for this exercise the original parameterisation will be referred to as parameterisation-A). This modified parameterisation encompassed the use of the ISLSCP II 1° × 1° gridded soil dataset (Global Soil Data Task, 2000); with soil albedo incorporated from the dataset derived from the MODIS global albedo product MCD43C1 by the University of Swansea (Houldcroft *et al.*, 2009) for use in the JULES model. The change in model simulated LST is illustrated in figure 3.16.

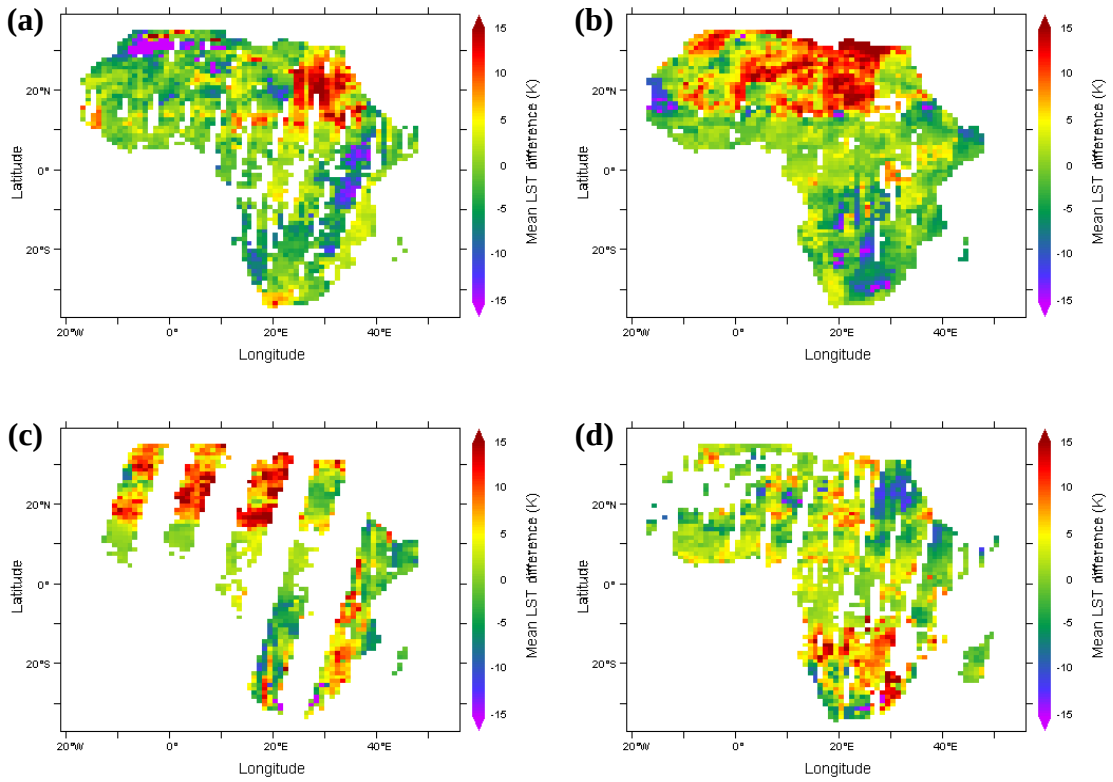

Figure 3.16: Mean 'daytime' LST (approximately 07:00 - 12:00 UTC) over Africa for JULES parameterisation-B minus JULES parameterisation-A during March (a); June (b); September (c); and December (d) of 2006.

Over much of the continent warmer signatures were obtained with parameterisation-B compared with parameterisation-A, particularly over the Sahara during June and September, and much of southern Africa during December. Mean continental differences between JULES and each of satellite-derived sources of LST (Table 3.7) substantiate this, with a reduction exhibited by parameterisation-B, compared with parameterisation-A, against both AATSR and SEVIRI. In the case of MODIS, the change from parameterisation-A to parameterisation-B has resulted in JULES simulating higher surface temperatures than MODIS during the 'night' for each of the four months.

Table 3.7: Mean day (approximately 07:00 - 12:00 UTC) and night (approximately 19:00 - 24:00 UTC) differences for March, June, September and December 2006, between both parameterisation-A and parameterisation-B of JULES, and each of the remote sensing products over the African continent.

Month	JULES (parameterisation-A) - EO data (K)			JULES (parameterisation-B) - EO data (K)		
	AATSR	**MODIS**	**SEVIRI**	**AATSR**	**MODIS**	**SEVIRI**
			Day			
March	-6.76	-1.85	-5.39	-6.42	-1.51	-5.05
June	-6.81	-2.14	-5.48	-5.13	-0.45	-3.79
September	-11.21	-5.27	-7.47	-7.94	-2.00	-4.21
December	-6.52	-2.25	-5.50	-4.83	-0.55	-3.81
			Night			
March	-3.27	-0.12	-5.45	-1.44	1.71	-3.62
June	-7.37	-2.20	-5.46	-2.55	2.62	-0.64
September	-8.49	-4.33	-7.54	-3.22	0.95	-2.27
December	-2.31	0.71	-1.15	-2.11	0.91	-0.95

The spatial pattern of the reduction in differences when parameterisation-B is used rather than parameterisation-A is confirmed when LST is analysed for each IGBP land cover class (Figure 3.17) with respect to SEVIRI. It is clear that the largest differences for parameterisation-A were generated over barren or sparsely vegetated surfaces, during both ‘day’ and ‘night’ windows and across seasons. In most comparison periods these differences were reduced with the introduction of parameterisation-B, significantly so during June and September. In fact where negative differences existed for parameterisation-A, these were reduced for parameterisation-B over the majority of surface types, or indeed became slightly positive. Average ‘night’ differences were reduced more than during the ‘day’; due primarily to the surface being kept warm as a result of enhanced ground heat flux due to the increased thermal conductivity of many grid-cells following the re-parameterisation of the soil. Not all surface types experience a reduction in difference though, evergreen broadleaf forest being a notable example; but overall the evidence from figures 3.16 and 3.17, and from table 3.7, is that the new

soil parameterisation incorporated into parameterisation-B has improved the simulation of LST by JULES when compared with retrievals from EO satellites.

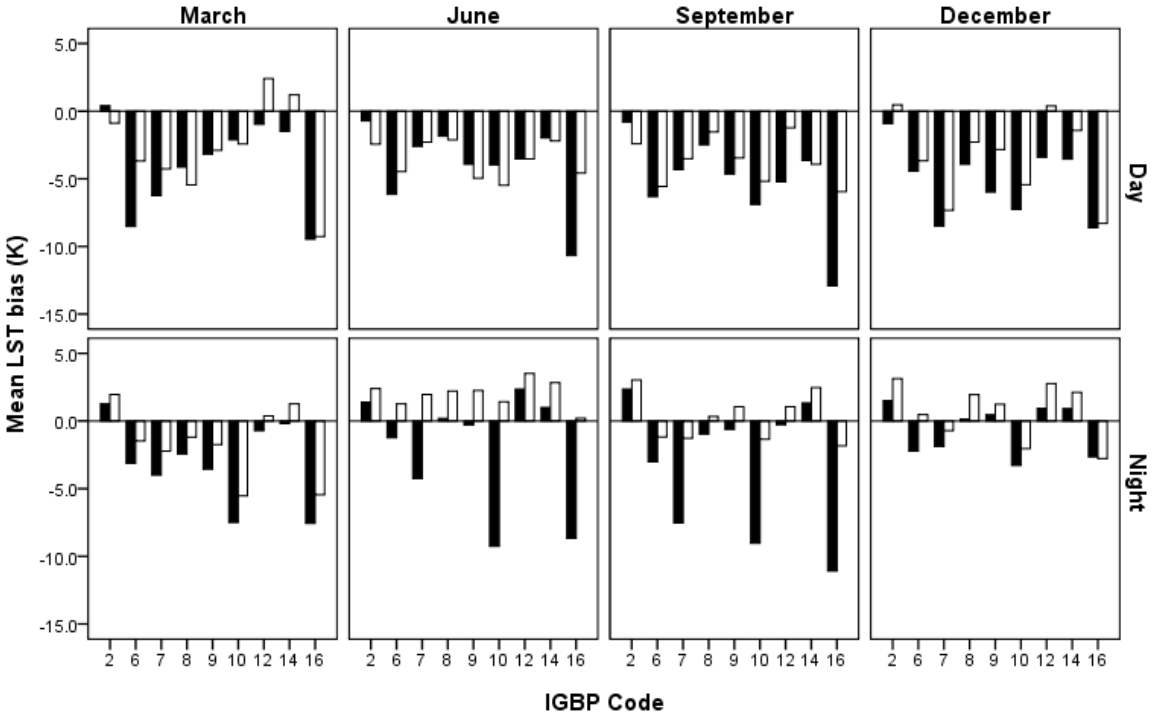

Figure 3.17: Comparison of the difference between JULES and SEVIRI for both parameterisation-A (black bars) and parameterisation-B (white bars) of JULES categorised by IGBP land cover classes: evergreen broadleaf forest (2); closed shrublands (6); open shublands (7); woody savannas (8); savannas (9); grasslands (10); croplands (12); cropland / natural vegetation mosaic (14); and barren or sparsely vegetated land (16).

3.4. Discussion

LST is an important component in the surface energy budget; and validation with field campaign measurements is an essential activity for ensuring the credibility both of remotely sensed datasets and the outputs of land surface models. Like all such undertakings though, the field exercise described here is subject to a number of uncertainties.

In the first place, timing was an unavoidable factor influencing the results. The field campaign, which was carried out over a site classified as semi-arid, was limited to a relatively narrow 15-day period of 2009 during the height of the southern African dry season. At this time of year the majority of the herbaceous layer is composed of dry grass. As such, different biases may result at alternative times of the year when live plants, which are actively transpiring, can be relatively cooler than other surface types - in contrast to the difference at the time of the field campaign - thus affecting LST averaging over a pixel. A similar case can be made for the tree canopy, which during the time of the field campaign consisted of a considerable percentage of drought deciduous trees. Indeed, the location and timing of the field campaign may have exacerbated the negative bias displayed by MODIS, since Wan *et al*. (2004) identified large uncertainties in the classification-based emissivities in such semi-arid regions. The spatial and temporal synchronicity between field measurements and remotely sensed measurements, for example in the precise timing of a satellite overpass or the geolocation accuracy of pixels, may also be a source of uncertainty.

In addition to the uncertainties associated with field radiometry described in section 3.2.5 intrinsic user error is inevitable - as in any field experiment - even though great care was taken to observe only a single surface type at nadir assisted by the use of a stabilising tripod. With regards to this point, measuring sunlit scenes at nadir generates an additional source of difference between the ground measurement and satellites - which do not view the surface at nadir. Indeed, recent studies have found that LST retrievals from satellites depend upon the angle of observation (Pinheiro *et al*. 2004; Pinheiro *et al*. 2006b). Since the upscaling of the three endmembers are biased towards sunlit scenes this could explain a proportion of the negative bias with respect to MODIS, and to a lesser degree SEVIRI which observes predominantly sunlit scenes. To

compensate for this a fourth radiometer would be required to measure the shadow scene beneath the tree canopy, whereby the different endmember proportions observed under different sun-view geometries could be estimated using a geometric projection model (Pinheiro *et al.*, 2006b).

Any methodology for upscaling from a 'point' source to that of a satellite pixel is also subject to uncertainties owing to the various assumptions that are necessarily made. A first assumption is that the precise geolocation and surface area of a satellite pixel can be guaranteed. Second, is that for each pixel validated the same generic land cover classes can be reliably classified. Finally, there is the assumption that within and between each pixel the thermal behaviour of each land cover class remains invariant; in reality this is not the case. For example, a significant factor which affects the emissivity of a surface feature, and hence LST variability, is moisture content (Goward *et al.*, 2002). Substantial LST heterogeneity can permeate an area of similar land cover features due to microscale variations in such traits. For sites which are homogeneous these issues are less significant, but unfortunately such sites are atypical, and do not give a sufficiently realistic representation of the terrestrial environment of the Earth.

Uncertainties aside, validation of LST with ground measurements can be a time consuming activity, and is geographically limited. A more feasible alternative, with a larger spatial and temporal consequence, is an intercomparison exercise between LST products retrieved from EO satellites. The intercomparison exercise carried out here generated, for the most part, findings which concur with previous studies (Madeira *et al.*, 2005; Noyes *et al.*, 2006; Trigo *et al.*, 2008a). If we consider for the moment the three satellite-derived LST products; a number of factors may have contributed to the differences encountered here and indeed in these prior studies. Firstly, although the comparison of synchronous retrievals in space and time was given utmost attention,

slight differences are to be expected. For example, discrepancies in geolocation can affect the heterogeneity of the surface which is analysed. Likewise, the ±10 minute tolerance window adhered to here, although narrow, represents adequate opportunity for LST variability. Secondly, the land surface is viewed from a different perspective by each satellite sensor, with the proportion of sunlit or shadow scenes viewed being a factor of the viewing angle. In the case of MODIS, retrievals are systematically lower than both AATSR and SEVIRI; this negative difference increases with increasing viewing angle. Finally, there are inherent differences in the way TOA radiances are processed by each sensor. Examples include the accuracy of instrument calibration, the application of different emissivity maps, and unique cloud clearing algorithms. Considering this last point further, cloud contamination limits the available imagery ensuring intercomparison exercises remain challenging undertakings; this was particularly so with respect to AATSR retrievals because of the longer repeat cycle. A final point here, is that further investigation into any effect Saharan dust aerosols have on TOA radiances is merited, which may be pertinent to intercomparisons over northern hemisphere Africa.

When LST simulated by the JULES model was compared with LST retrieved from EO satellites, large negative differences were found between JULES and satellite sources during both day and night. Several possible reasons for these differences could be considered. A tendency for satellite-derived LST products to overestimate ground-based measurements has been reported (Trigo *et al.*, 2008a), and although theoretically this could explain some of deviation, this phenomenon was not evident from the field campaign carried out here. The way in which the model aggregates LST over a grid-box was also not considered significant, as discussed in section 3.3.2. One potential inconsistency between EO sources and land surface modelling could be with the

varying assumptions applied in the algorithms for generating LST, although such differences are likely to be difficult to quantify. On the other hand, it has been shown that an alternative parameterisation of the soil conditions - including albedo - resulted in a reduction in the mean negative difference. Such an improvement is rational since surface albedo and soil moisture are key determinants of LST variability (Goward *et al.*, 2002). Surface albedo, for example, controls the quantity of energy absorbed by the surface. As for soil moisture, a dry soil surface is generally hotter and loses more sensible heat, whereas a wet soil surface in general has a lower surface temperature and loses more latent heat (Smith *et al.*, 2006).

3.5. Conclusions

This investigation has evaluated the accuracy to which a key boundary condition, LST, can be simulated by the JULES model. In the case of Africa, much weight is placed on model simulations and EO data to quantify surface-to-atmosphere heat and water fluxes, since the ground observation network remains relatively sparse, and as such accuracy is fundamental. Here, an evaluation of both model output and retrievals from EO satellites was carried out over a savannah landscape of South Africa. This was complemented with an intercomparison between each source of LST over the whole of the continent; and this two-pronged approach represents a unique undertaking in evaluating the JULES model with respect to LST. Specifically, two research questions have been addressed: i) how accurately is LST simulated by JULES and retrieved from EO satellites for a mixed tree/grass landscape of Africa; ii) how comparable is LST simulated by JULES over continental Africa with respect to satellite-derived LST products.

The findings from the *in situ* exercise indicate that both AATSR and SEVIRI are retrieving LST over a mixed tree/grass landscape with uncertainties lower than their

respective target accuracies. MODIS on the other hand did not meet its target accuracy. As for JULES, the uncertainty derived here of 3.69K was the highest of the individual sources of LST, with an average overestimation with respect to *in situ* measurements of 2.48K. Results from the intercomparison indicate JULES systematically underestimated LST with respect to AATSR and SEVIRI in particular. This was most marked over barren or sparsely vegetated landscapes, although a considerable reduction in this difference was achieved with a re-parameterisation of soil properties. Indeed, all subsequent research carried out with the JULES model was performed under this modified soil parameterisation (parameterisation-B) and will be referred to henceforth simply as JULES.

The JULES model, like probably all land surface models, is limited by the accuracy to which the physical processes of the terrestrial biosphere can be realistically imitated. Improvements may be possible by integrating observation data into the model, with EO satellites representing the most practical source at a global or regional scale.

Chapter 4

Development and validation of a LST data assimilation scheme

An ongoing motivation of this study has been that JULES, like all land surface models, has uncertainties resulting from inappropriate parameterisation, the approximation of physical processes and land surface heterogeneity. As such, key variables can be inadequately represented. In this research, it was shown in chapter 2 that LST, which forms an integral component in the surface energy budget and in soil moisture-climate feedbacks, is simulated by the JULES model with considerable uncertainty. Having identified a deficiency in the simulation of this key boundary condition, the next appropriate step is to investigate whether the integration of instantaneous observations from EO satellites improves the ability of the model to accurately estimate important fluxes between the land and the atmosphere. This technique is known as data assimilation.

This chapter focuses on analysing the behaviour of the JULES land surface model when remotely sensed LST observations retrieved from satellite are assimilated into the model. The aim here is to investigate whether a reduction in uncertainty in the ability of JULES to model the energy and water cycles by means of data assimilation is possible. Two questions will be considered when tacking this problem: i) can a reduction in the uncertainty of surface energy fluxes be achieved by constraining simulations of LST with observation data; and ii) how does the assimilation of satellite-derived LST affect the quantification of soil moisture.

4.1. Introduction

Large uncertainties persist in our understanding of biogeochemical cycle feedbacks. A sizeable portion of this uncertainty may be attributed to the quantification of land/atmosphere interactions within coupled climate models (Notaro, 2008), which diminishes our capability to accurately model climate feedbacks. Indeed, the limited collection of equations to represent complex biophysical processes and a tendency of over-parameterisation (Pipunic *et al.*, 2008) infers a degree of uncertainty in land surface modelling. An increasingly exploited technique to constrain model predictions with observation data is data assimilation; with *in situ* observations, such as from the FLUXNET network, used in data fusion experiments (Williams *et al.*, 2009). EO data represents a feasible alternative source of observations over large geographical areas, particularly where the *in situ* observation network is sparse such as in Africa.

Data assimilation involves the adjustment of the model state with external measurements of a predictable uncertainty, in order to minimise the errors in the model predictions. The model state is updated at regular intervals when observations become available. The strength of the adjustment is derived from the respective weightings of both the model and observation uncertainties. In cases where the observation values are more accurate than the model estimates, for instance, the model state is adjusted in a way in which it more closely corresponds to the observations.

Considerable research has focused on data assimilation into atmospheric models (Daley, 1991; Houtekamer and Mitchell, 2001; McNally *et al.*, 2006; Uppala *et al.*, 2005), with the state-of-the-art being to directly assimilate radiances from EO satellites into models. Ocean/atmosphere models have also received attention (Annan *et al.*, 2005; Ridgwell *et al.*, 2007), driven by the need to better understand the role of ocean biogeochemistry in the long-term regulation of atmospheric carbon. Only relatively

recently has focus switched to the land surface, with EO data being assimilated into hydrologic (Reichle *et al.*, 2002; Crow and Wood, 2003) and ecosystem models (Williams *et al.*, 2005; Quaife *et al.*, 2008; Rastetter *et al.*, 2010).

As is the case with this investigation, particular attention has been given to the assimilation of satellite-derived LST to constrain surface heat flux and soil moisture estimations (Bosilovich *et al.*, 2007; Huang *et al.*, 2008; Margulis and Entekhabi, 2003). In a recent intercomparison (de Rosnay *et al.*, 2009) much variation between land surface models was identified in the simulation of soil moisture. Optimisation, as a result of data assimilation, would appear a worthwhile mission, presenting an opportunity to improve our predictive ability of land/atmosphere fluxes of energy and water; the prospect being a reduction in climate feedback uncertainty.

Numerous assimilation mechanisms exist, including the three-dimensional and four-dimensional variational schemes, and the Kalman Filter. The latter provides an optimum linear sequential solution based on *a priori* knowledge of model and observation uncertainties (Gelb, 1974). This method evolved into variants to cope with non-linear assimilation - the Extended Kalman Filter (EKF) – and further, to avoid the computationally expensive integration of the state error covariance matrix – the Ensemble Kalman Filter (EnKF). The EnKF first proposed by Evensen (1994) employs a Monte Carlo approach and is more flexible and robust in covariance modelling than the EKF (Reichle *et al.*, 2002). In previous implementations, Huang *et al*. (2008), for example, assimilated LST from EO satellites resulting in a 1.0K improvement in soil temperature estimates. Pipunic *et al*. (2008) also assimilated satellite-derived LST, as well as latent and sensible heat observations, to manipulate surface heat flux predictions. A key finding was that the assimilation of higher temporal source data resulted in more accurate predictions. Finally, the assimilation of canopy reflectance by

Quaife *et al*. (2008) into a simple carbon pool and box model produced substantial improvements in the estimation of GPP.

While much success has been achieved in assimilating observations into relatively simple biosphere models, few attempts, like that of Vivoy et al. (2001) who investigated normalised difference vegetation index (NDVI) assimilation into the ORCHIDEE model have looked at data assimilation into complex biophysical and biogeochemical models. In the case of JULES, this first study here into assimilating LST by means of the EnKF represents a pertinent objective, and a logical step in the ongoing evolution the land surface scheme which has seen improvements to the standard implementation in recent years (Alton *et al.*, 2007b; Mercado *et al.*, 2007).

Here, the assimilation into the JULES model of LST retrieved from the SEVIRI instrument is presented, including a description of the assimilation methodology. The effect on soil moisture and surface heat fluxes were analysed, whereby the model simulations were compared with a satellite-derived soil moisture dataset and *in situ* measurements respectively. Finally, the implications of data assimilation on terrestrial feedbacks to the climate system and the implications for biogeochemical cycling are considered.

4.2. Materials and methods

4.2.1. Model dynamics

The surface temperature T_{sfc} is key to the derivation of both sensible and latent heat fluxes. Temperature and humidity gradients between the surface and atmospheric reference height z_1 above the surface are used to derive the sensible heat flux (H) and latent heat flux (LE) respectively:

$$H = \frac{\rho c_p}{r_a}\left(T_{sfc} - T_1 - \frac{g}{c_p} z_1 \right) \quad (15)$$

$$LE = \Psi \frac{L\rho}{r_a}\left(q_{sat}(T_{sfc}) - q_1 \right) \quad (16)$$

Where ρ is the surface air density, c_p is the specific heat capacity of the air, L is the latent heat of vaporisation of water, r_a is the aerodynamic resistance, g is the acceleration due to gravity, $q_{sat}(T_{sfc})$ is the saturated specific humidity at surface temperature T_{sfc}, and T_1 and q_1 are the air temperature and specific humidity respectively at reference height z_1. Finally, Ψ is a factor determined from the proportions of bare soil evaporation, canopy evaporation, sublimation from snow, and transpiration by vegetation; LE is thus driven by evapotranspiration (ET).

Soil moisture, a characteristic which demonstrates a long memory, is also controlled by evapotranspiration, in which changes in the surface soil moisture M_1 is incremented not only by transpiration extracted directly from the surface layer by plant roots, but also by the diffusive water flux flowing between layers - which consists of throughfall precipitation P_f, snowmelt S_m, surface runoff Y_s, and the diffusive water flux flowing out to the layer below W_1 - and is expressed in equation (17). Total unfrozen soil moisture content M within each layer, is given by equation (18).

$$\frac{dM_1}{dt} = P_f + S_m - Y_s - W_1 - \rho\,(1 - f_a)\{q_{sat}(T_{sfc}) - q_1\}\left\{\frac{(1-v)\,\beta(\Theta_1)}{r_a + r_{ss}} + \frac{e_1 v}{r_a + r_c}\right\} \quad (17)$$

$$M = \rho_w \Delta z \Theta_u \quad (18)$$

Where f_a is the grid-box wet canopy fraction, v is the grid-box fractional cover of vegetation, $\beta(\Theta_1)$ is the soil moisture availability factor with volumetric soil moisture concentration Θ_1 in the surface soil layer, e_1 is the fraction of the transpiration extracted

from the surface soil layer, r_{ss} and r_c are a fixed soil surface resistance and the canopy resistance respectively, ρ_w is the density of water, Δz is the depth of the soil layer, and Θ_u is the volumetric concentration of unfrozen soil moisture. W_1 is expressed as:

$$W_1 = K \left\{ \frac{\partial \psi}{\partial z} + 1 \right\} \tag{19}$$

Where K is the hydraulic conductivity and ψ is the soil water suction, assuming the Clapp and Hornberger (1978) dependencies. A more comprehensive picture of the soil hydrological and thermodynamic components of the model can be found in Cox *et al*. (1999).

4.2.2. Data assimilation method

Data assimilation was carried out using the EnKF, with the exact implementation (Ghent *et al.*, 2009; Ghent *et al.*, 2010; Ghent *et al.*, in press) following the approach of Evensen (2003). The EnKF propagates an ensemble of states, whereby the expensive integration of the standard Kalman Filter is avoided, with the distribution of the ensemble spread determining the state error covariance matrix. For this implementation only LST is directly manipulated, with $\mathbf{X}_{t+1}$ being the state vector representing LST for every grid-box at time t+1 and is defined as:

$$\mathbf{X}_{t+1} = F\,(\mathbf{X}_t, \boldsymbol{\alpha}_{t+1}, \boldsymbol{\beta}) \tag{20}$$

Where F is the model operator which operates on the state vector $\mathbf{X}_t$ at time t, the meteorological forcing data $\boldsymbol{\alpha}_{t+1}$ at t+1, and the time-invariant biophysical parameters $\boldsymbol{\beta}$. Here, the model operator is JULES, and the meteorological forcing variables have been listed in table 2.1.

For the initial state (t=0) following spin-up of the model, each ensemble member of the state vector $\mathbf{X}_0^a$ is derived by adding random noise which conforms to a Gaussian distribution with zero mean and error covariance $\mathbf{P}_0$, based on knowledge of the model error. For the general case, at time t+1 each ensemble member of the forecast state vector $\mathbf{X}_{t+1}^f$ is propagated with the addition of stochastic forcing $\boldsymbol{\gamma}$ to equation (20) and is expressed as:

$$\mathbf{X}_{t+1}^f = F\,(\mathbf{X}_t^a, \boldsymbol{\alpha}_{t+1}, \boldsymbol{\beta}) + \boldsymbol{\gamma} \qquad \boldsymbol{\gamma} \sim N\,(0, \mathbf{P}) \tag{21}$$

Where $\mathbf{X}_t^a$ is the analysis state vector at time t, and $\boldsymbol{\gamma}$ conforms to a Gaussian distribution with zero mean and model error covariance **P**.

Data assimilation performance is strongly affected by the model error, which in this experiment was based on the standard deviation of the bias between the simulations by the model and *in situ* measurements taken during the field campaign described in section 3.2. The model error was thus defined as 3.69K (Table 3.6). Each ensemble member of the forecast state for a grid-box is updated when observations for that grid-box become available, by applying the update equation:

$$\mathbf{X}^a = \mathbf{X}^f + \mathbf{K}\,(\mathbf{y} - \mathbf{H}\mathbf{X}^f + \boldsymbol{\varepsilon}) \qquad \boldsymbol{\varepsilon} \sim N\,(0, \mathbf{R}) \tag{22}$$

Where **K** is the Kalman gain matrix, **H** is the observation operator relating the model state to the observations **y**; with the observations being perturbed with stochastic forcing $\boldsymbol{\varepsilon}$ conforming to a Gaussian distribution with zero mean and observation error covariance **R**. Here, the observation error was based on the SEVIRI LST product uncertainty, which was defined as 1.5K according to the study by Sobrino and Romaguera (2004). This definition is comparable to the observation error of 1.65K

measured during the field campaign described in section 3.2. The Kalman gain matrix is a function of the forecast model error covariance matrix $\mathbf{P}^f$, and the observation error covariance matrix **R**, and determines the correction to the forecast state vector:

$$\mathbf{K} = \mathbf{P}^f \mathbf{H}^T [\, \mathbf{H}\, \mathbf{P}^f \mathbf{H}^T + \mathbf{R}\,]^{-1} \quad (23)$$

The cost of solving equation (23) is a function of the number of ensemble members; to avoid excessive computational cost the optimum ensemble size should be determined. The mean of the ensemble members is a measure of the optimum estimate of the model state (Burgers *et al.*, 1998; Evensen, 2003), and the variance around the mean can be taken as an indication of the uncertainty. Manipulations to LST (T_{sfc}) through the process of data assimilation are propagated throughout the model, affecting predictions of heat and water fluxes (equations (15) to (17)).

4.2.3. Experimental setup

For this investigation, the experimental setup of JULES mirrored for the most part that which has been described in section 2.2.3, with the soil properties parameterised as per parameterisation-B described in section 3.3.2. The model was first spun-up by repeating the years 2002 to 2006 inclusive until soil temperature and moisture conditions were equilibrated, with the resultant spun-up state saved as a file. Two separate renderings of the model were run for the whole of 2007: one with a 1° × 1° spatial resolution covering continental Africa; and 'point' scale runs at specified validation locations. In both cases the model was run with an hourly time-step.

This experiment involved SEVIRI observations being assimilated into both renderings of the JULES model. This choice of SEVIRI LST was based on the associated fine temporal resolution of both satellite-derived product and the model. In

the continent-wide case, cloud-free LST pixels from SEVIRI were averaged over each grid-box; whereas for the 'point' cases, LST was retrieved from each pixel corresponding to each validation location.

An underlying assumption of data assimilation is that the differences between the modelled values and observations are not biased. However, systematic biases often exist due to uncertainties among EO products as a result of variable observation angles, cloud contamination, and the bias towards cloud-free rather than all-sky conditions; but also due to the fact that land surface heterogeneity in models is at best parameterised. Such biases prevent a statistically optimal analysis (Dee and da Silva, 1998), and chapter 3 demonstrated that systematic bias exists between the JULES model and satellite-derived LST, even following the re-parameterisation of the soil properties. To resolve this, the bias correction methodology of Reichle and Koster (2004) was applied. This involves model and observation cumulative distribution functions (cdfs) being equated (Figure 4.1), and is an appropriate method, since the bias is not attributed to a one particular source (Drusch *et al.*, 2005).

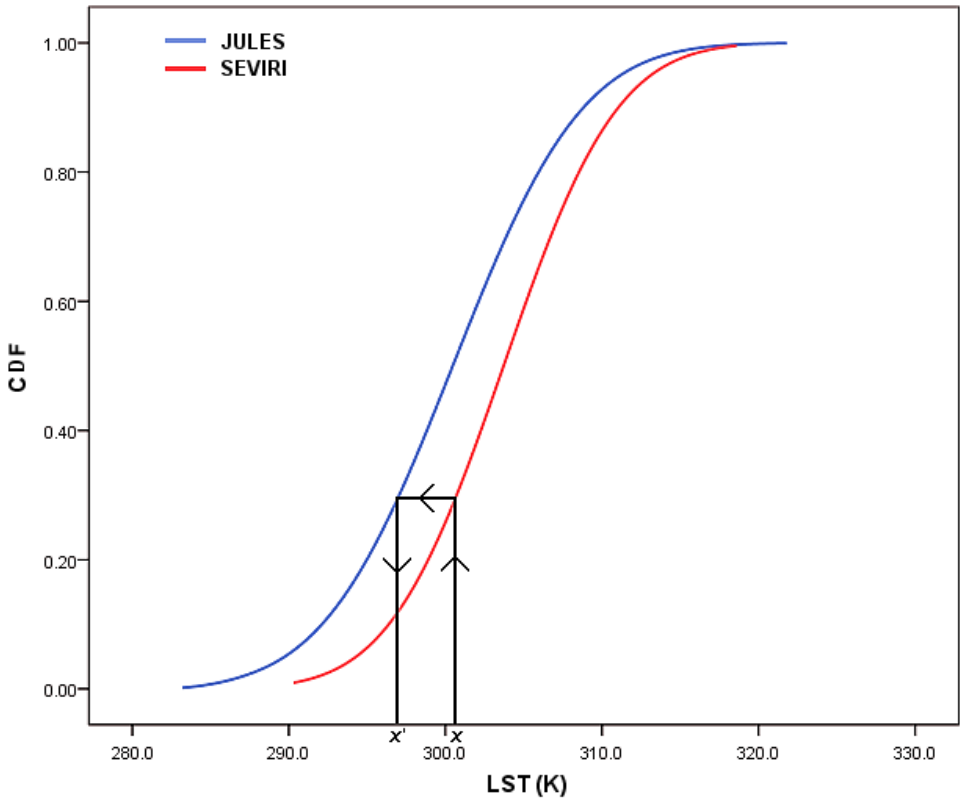

Figure 4.1: The average cumulative distribution functions (cdfs) of LST from JULES and SEVIRI, whereby, unscaled SEVIRI observation x are converted into scaled observations x′ using cdf matching. Figure reproduced from Ghent et al. (2010).

In this investigation, SEVIRI LST observations (denoted by x) are converted into scaled LST observations (denoted by x') by solving equation (24):

$$cdf_j(x') = cdf_s(x) \tag{24}$$

Where cdf_j and cdf_s are the JULES and SEVIRI cumulative distribution functions respectively. This cdf matching was performed with values covering the whole year for every grid-box.

4.2.4. Validation protocol

To evaluate the impact of the assimilation of LST into the JULES model, soil moisture was compared, both with and without assimilation, against a satellite-derived dataset for an area of West Africa (15°W to 10°E longitude, 5°N to 20°N latitude) from 1st January to 31st May 2007. In addition, energy fluxes were compared with measurements retrieved from four flux towers managed by the CARBOAFRICA consortium as part of the FLUXNET network using the Eddy Covariance method (Baldocchi *et al.*, 2001). Comparisons were made, both for open loop modelling – that is without data assimilation; and following the assimilation of LST, from 1st October to 31st December 2007 against H and LE fluxes from: savannah/grassland at Demokeya (13.28º N, 30.48º E), Sudan; Miombo woodland at Mongu (15.44º S, 23.25º E), Zambia; semi-arid savannah at Skukuza (25.02º S, 31.50º E), South Africa; and tropical savannah at Tchizalamou (4.29º S, 11.66º E), the Congo (Figure 4.2).

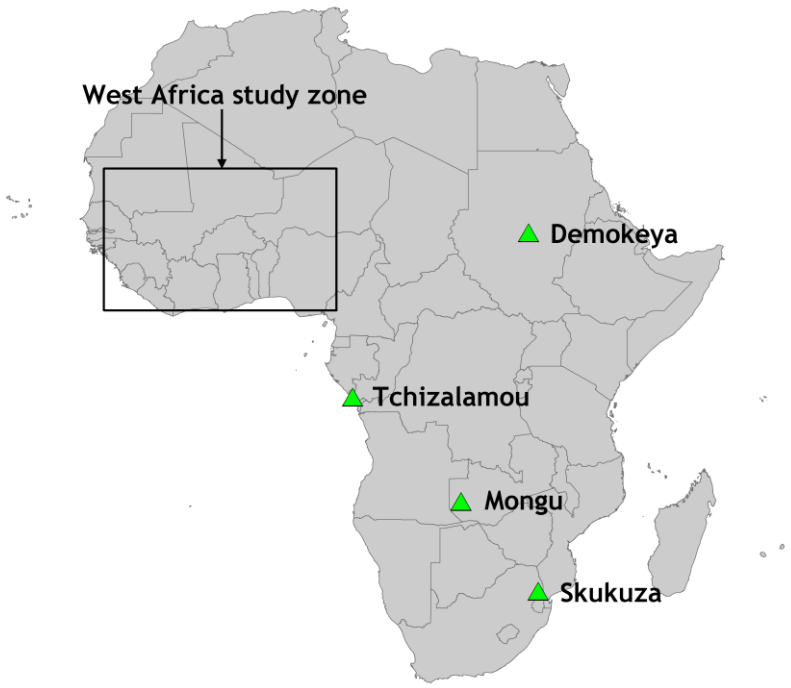

Figure 4.2: Location of the four flux towers for validation of surface energy fluxes, and the area of West Africa over which soil moisture is evaluated with and without data assimilation.

The soil moisture dataset used here is derived from radar backscattering coefficients, which are sensitive to surface soil water without being affected by cloud; and are produced from the active C-band (5.6 GHz) microwave scatterometer instruments on board the European Remote Sensing Satellites (ERS-1 and ERS-2). A surface soil moisture (SSM) dataset has been developed by the Institute of Photogrammetry and Remote Sensing at the Vienna University of Technology, with SSM 'observations' in the top 5cm of the soil profile, retrieved from two separate ERS receiving stations: Maspalomas and Matera, applicable to this study.

To summarise, the change detection method, which generates the SSM dataset in a discrete 12.5km global grid, involves scatterometer estimates being used to model the incidence angle dependency of the radar backscattering coefficients. These are normalised to a reference incidence angle of 40°, and scaled over the long-term between the driest and wettest observations to produce relative SSM data, which ranges from 0% to 100%. A full account of the method for SSM retrieval can be found in Wagner *et al*. (1999), with the soil moisture noise model (Naeimi *et al.*, 2009) describing the uncertainty.

Good agreement has been shown for the SSM dataset, both against other datasets of soil moisture (Wagner *et al.*, 2003; Pellarin *et al.*, 2006; Crow and Zhan, 2007), and *in situ* measurements (Wagner *et al.*, 1999; Ceballos *et al.*, 2005). For example, in studies over Ukrainian field sites (Wagner *et al.*, 1999), and across a network of 20 stations in western Spain (Ceballos *et al.*, 2005), mean correlations in the top 100cm of the soil profile were found to be 0.41 and 0.75 respectively. In this latter study the RMSE between the scatterometer data and the average soil moisture was found to be 2.2%.

4.3. Results

Prior to analysing the effect of data assimilation on model output, an optimum ensemble size was selected. Different sizes were tested, and the RMSEs were evaluated against MODIS LST, which acted as an independent source of LST. A considerable reduction in RMSE is encountered, compared with the open loop scenario, when even a small number of ensemble members are chosen (Figure 4.3).

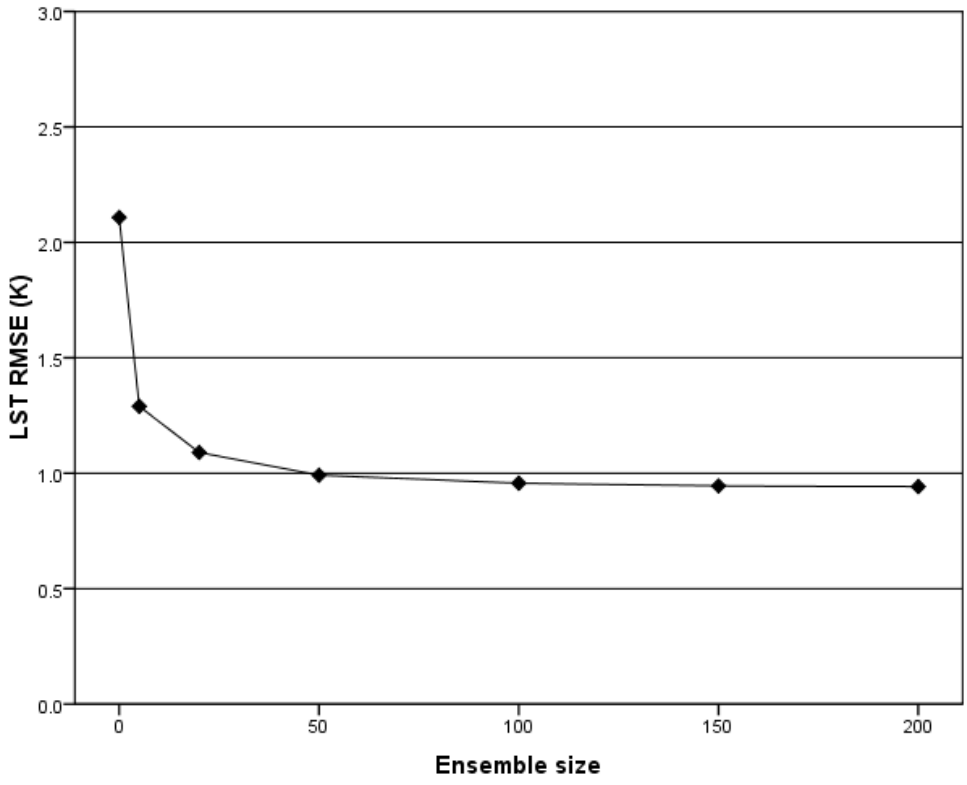

Figure 4.3: Comparison test of LST RMSEs with respect to MODIS LST observations following the assimilation of SEVIRI LST into JULES for different ensemble sizes during 2007. Figure reproduced from Ghent et al. (2010).

As the ensemble size is increased the reduction in RMSE continues albeit at a decreasing rate. To test the significance of these reductions *t*-tests assuming equal variances were performed on the mean RMSEs from 50 repeated runs at ensemble sizes of 5, 20, 50, 100, 150 and 200. The reduction in RMSE remained statistically significant

at the 5% level when the ensemble size was increased up to 100 ensemble members, but ceased to be significant when the size was increased to 150. All subsequent experiments were thus carried out with an ensemble size of 100.

With regards to applying the method over the West African study zone, mean soil moisture in the top 5cm of the soil profile simulated by JULES is clearly higher than 'observations' derived from the ERS scatterometers for the first five months of 2007 (Figure 4.4). It is also evident that the updated model estimates following the assimilation of LST are more comparable with the 'observations'.

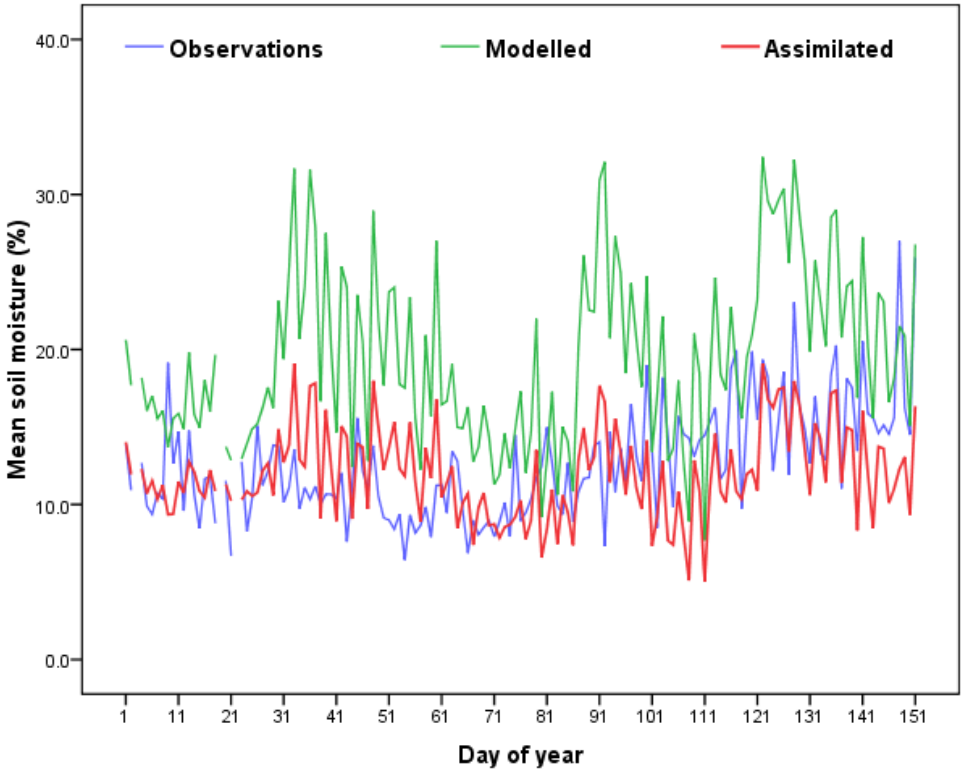

Figure 4.4: Time series of mean soil moisture in the top 5cm of the soil profile over a region of West Africa (15°W to 10°E longitude, 5°N to 20°N latitude) from 1st January – 31st May 2007 for both open loop modelling and model simulations following LST assimilation. Surface soil moisture observations derived from ERS scatterometers are plotted for comparison. Figure reproduced from Ghent et al. (2010).

The change in simulated soil moisture is not homogeneous across the region, and figure 4.5 illustrates the spatial distribution of the differences between model estimates with and without data assimilation. The effect of assimilation can be quantified as a 21.6% reduction in RMSE between the model estimates and the ERS scatterometer 'observations'. The significance of this reduction was examined with *t*-tests assuming equal variances on the mean RMSEs from 50 repeated runs with and without assimilation. The *t*-statistic of 10.4 indicated that the RMSE reduction was statistically significant at the 99% confidence level.

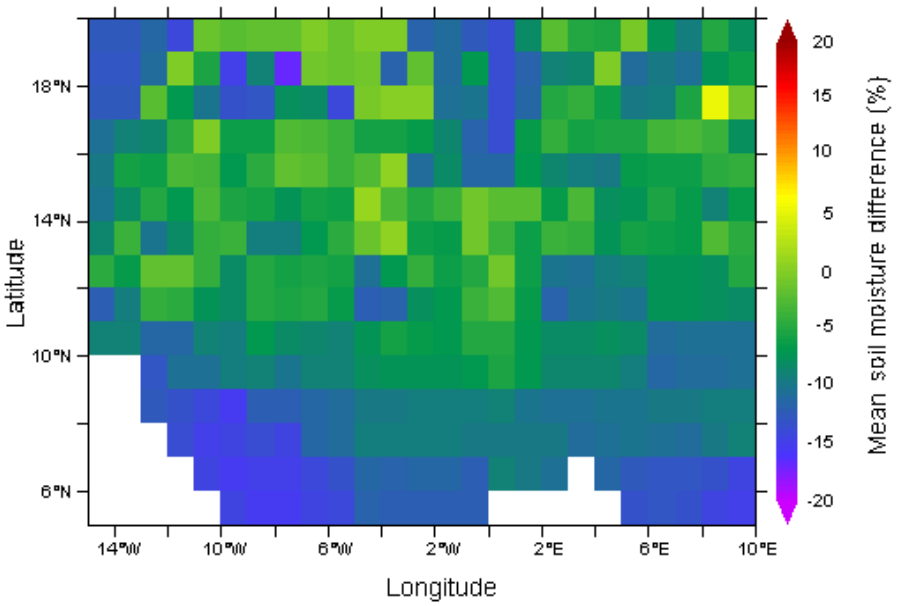

Figure 4.5: Mean daily soil moisture difference between open loop modelling and model simulations with LST assimilation in the top 5cm of the soil profile over a region of West Africa (15°W to 10°E longitude, 5°N to 20°N latitude) from 1st January – 31st May 2007. Figure reproduced from Ghent et al. (2010).

The updating of modelled LST following assimilation drives changes in the partitioning of available energy into H and LE fluxes; with H being a function of the difference between temperatures at the surface and the surrounding air (Rhoads *et al.*, 2001), and LE being a function of the influence surface temperature exerts on the vapour pressure deficit (Hashimoto *et al.*, 2008). Partitioning is also influenced by

available soil moisture and vegetative cover, with LE exchange higher for greater vegetative cover (Smith *et al.*, 2006). These fluxes are tightly coupled within the surface energy balance equation, whereby an increase in one is associated with a decrease in the other. Figures 4.6 and 4.7 illustrate the change in H, LE and ET fluxes respectively for both open loop modelling and following data assimilation over the same geographical area of West Africa during the first five months of 2007.

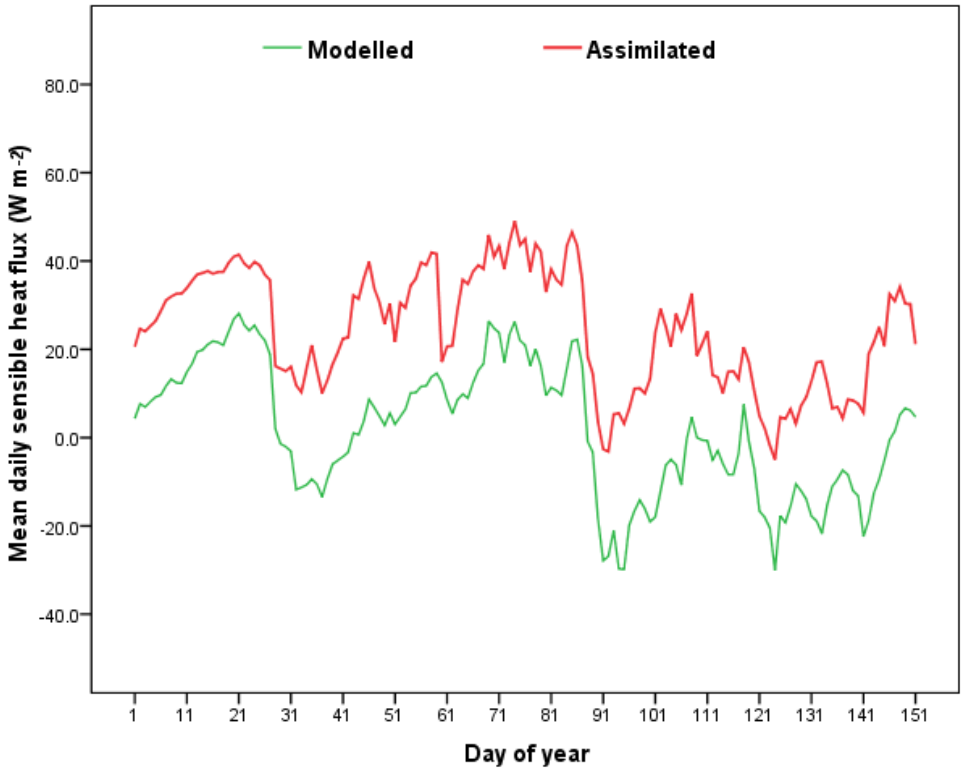

Figure 4.6: Time series of mean sensible heat flux over a region of West Africa (15°W to 10°E longitude, 5°N to 20°N latitude) from 1st January – 31st May 2007 for both open loop modelling and model simulations following LST assimilation.

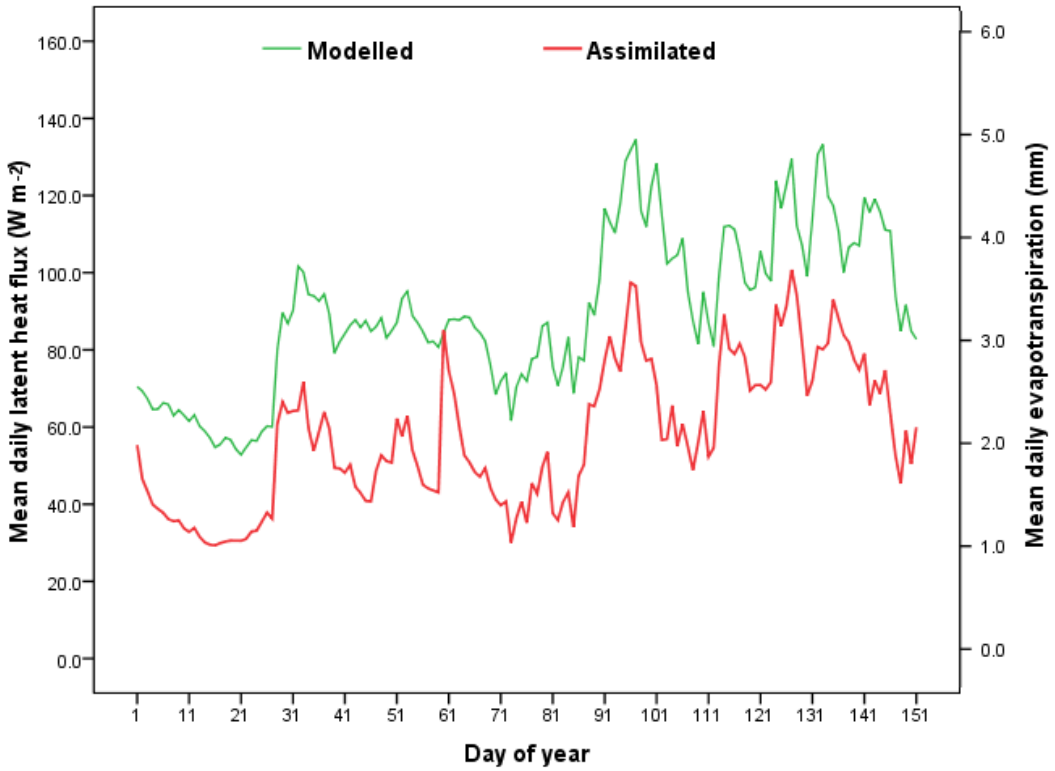

Figure 4.7: Time series of mean daily latent heat flux (left axis) and mean daily evapotranspiration (right axis) over a region of West Africa (15°W to 10°E longitude, 5°N to 20°N latitude) from 1st January – 31st May 2007 for both open loop modelling and model simulations following LST assimilation. Figure reproduced from Ghent et al. (2010).

The impact of data assimilation has been to increase the H flux while simultaneously decreasing the LE flux. This is consistent with the reduction in soil moisture; a drier soil heats up more rapidly, since air which has a lower heat capacity than water occupies a greater percentage of the soil, and the drier soil loses a greater proportion of energy as sensible heat. In the case of LE, these changes are driven by changes in ET.

Figures 4.8 and 4.9 quantify the effect of LST assimilation on the fluxes of H and LE respectively in comparison with Eddy Covariance measurements from the four flux towers at Demokeya, Mongu, Skukuza and Tchizalamou for the final three months of

2007, which was the only period during this year where sufficient data was available for all sites. It is evident that differences exist between the *in situ* measurements and the model estimations – for both open loop modelling and when LST was assimilated. Although the general seasonality within each time series is comparable, JULES displays a tendency to under-estimate sensible heat and over-estimate latent heat. However despite these differences, at each site and for each variable, reductions in RMSE were found when LST was assimilated compared with open loop modelling (Table 4.1). Although only the H flux at Demokeya appeared to experience a strong reduction in RMSE, all the reductions were found to be significant at the 95% confidence level when *t*-tests assuming equal variances were carried out on 50 repeated model runs with and without data assimilation. In fact, three quarters of RMSE reductions recorded in table 4.1 were significant at the 99% confidence level.

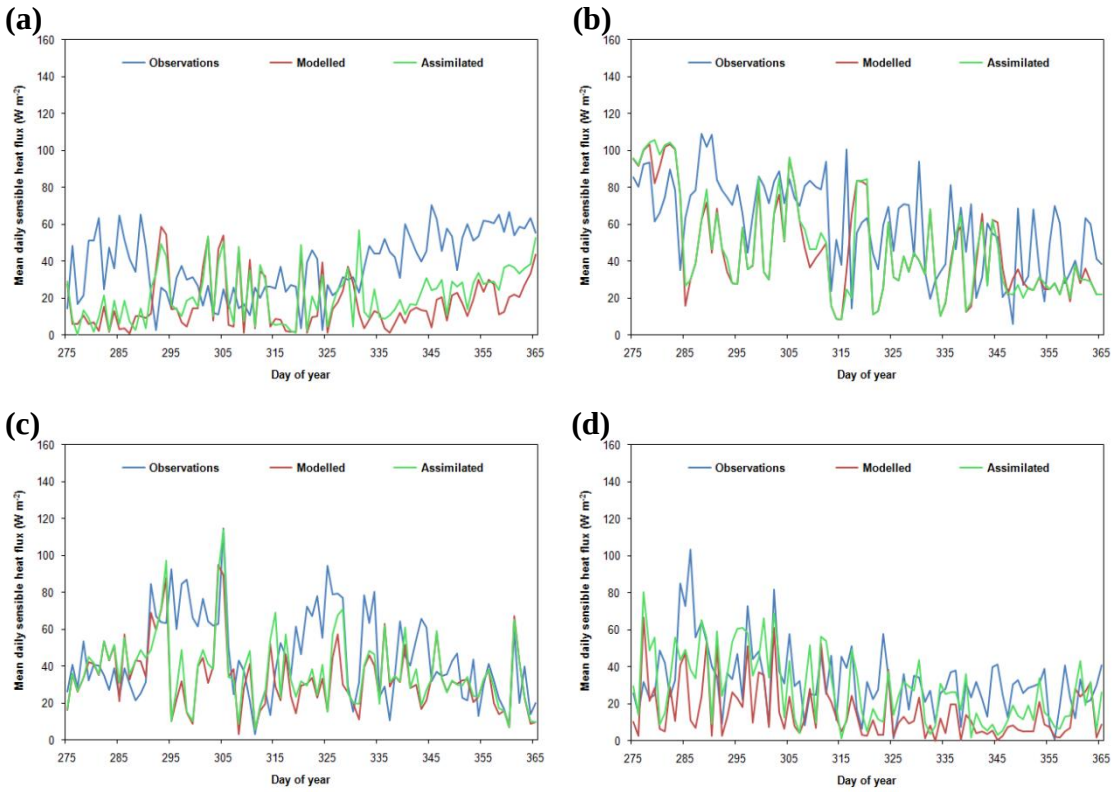

Figure 4.8: Time series of mean sensible heat flux at four flux towers from 1st October – 31st December 2007: Demokeya, Sudan (a); Mongu, Zambia (b); Skukuza, South Africa (c); and Tchizalamou, Congo (d). The time series indicate the Eddy Covariance observations together with both open loop modelling and model simulations following LST assimilation into JULES.

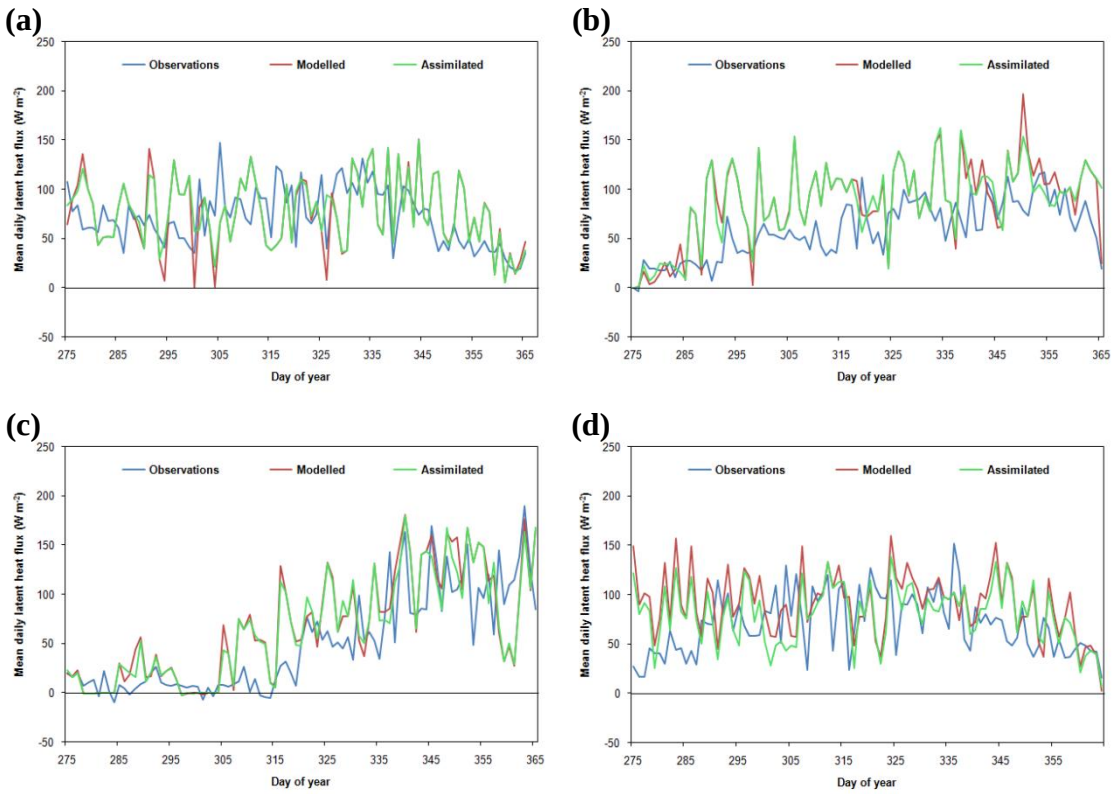

Figure 4.9: Time series of mean latent heat flux at four flux towers from 1st October – 31st December 2007: Demokeya, Sudan (a); Mongu, Zambia (b); Skukuza, South Africa (c); and Tchizalamou, Congo (d). The time series indicate the Eddy Covariance observations together with both open loop modelling and model simulations following LST assimilation into JULES.

*Table 4.1: Evaluation of model simulations of sensible (H) and latent heat (LE) fluxes with and without LST data assimilation from 1st October to 31st December 2007, with respect to 1-hourly Eddy Covariance measurements from four flux towers: Demokeya, Sudan; Mongu, Zambia; Skukuza, South Africa; and Tchizalamou, Congo. t-tests assuming equal variances were performed on the mean RMSEs from 50 repeated runs, with the percentage reduction in RMSE given along with the t-statistic and an indication of significance of the one-tailed t-test (** refers to significance at the 0.99 level; * refers to significance at the 0.95 level). Table reproduced from Ghent et al. (2010).*

Source	**Variable**	**Modelled RMSE (W m^{-2})**	**Assimilated RMSE (W m^{-2})**	**Error reduction (%)**	***t*-statistic**
Demokeya	H	54.15	40.78	24.69	35.393**
	LE	41.07	40.31	1.85	1.993*
Mongu	H	41.42	40.56	2.08	2.251*
	LE	49.21	47.29	3.90	4.441**
Skukuza	H	30.76	28.66	6.83	5.066**
	LE	47.52	43.17	9.15	10.935**
Tchizalamou	H	27.18	24.26	10.74	7.620**
	LE	41.30	39.48	4.41	4.938**

4.4. Discussion

Land surface models are able to simulate the global state of the terrestrial biosphere over the full diurnal cycle, yet they are limited by the accuracy in which they can represent the full complexity of physical processes which constitute the land surface. Remote sensing on the other hand is able to provide an instantaneous observation of the area of interest, but can be hampered by sporadic instrumentation problems, missing data as a result of cloud contamination for example, and is constrained by the inability of a single sensor to provide full diurnal coverage at a global scale. Data assimilation combines these alternative sources of information, balancing the uncertainty in both, in order to produce an optimal representation of the evolving state of the land surface.

The mechanism employed in this investigation was the EnKF. Over land, use of the EnKF is often based on covariance localisation methods, whereby the global analysis is sub-divided into smaller sub-domains. As described in previous implementations (Hamill *et al.*, 2001; Houtekamer and Mitchell, 2001), these sub-domains are independently analysed based solely on local observations, and simultaneously updated in parallel. This technique effectively sets sampled cross-covariances between geographically disparate points to zero; a requirement due to the possibility of spurious cross-correlations, with the EnKF being subject to sampling errors which are a function of the ensemble size (Evensen, 2003). Indeed, for small ensemble sizes the accuracy of estimations has been shown to be better with covariance localisation (Reichle and Koster, 2003). In the case of JULES grid-cells are independent of each other, since there are no lateral fluxes between individual cells, and as such the sub-domains analysed here were the individual cells.

The assimilation of SEVIRI LST into the JULES model from 1st January to 31st May 2007 for each grid-cell of the West African study zone resulted in a mean reduction in soil moisture in the top 5cm of the soil profile. The upshot being, that simulations were more comparable with the SSM dataset derived from ERS scatterometers; although a note of caution when using this dataset, is that during retrieval azimuthal viewing geometry is not taken into account, increasing the possibility of biased estimates in extreme climates, such as deserts (Bartalis *et al.*, 2006). That said, the assimilation of LST also affected the partitioning of energy between H and LE fluxes, with the comparison against Eddy Covariance measurements from four flux towers resulting in statistically significant reductions in RMSEs (with data assimilation) for all site-variable combinations.

In general, it can be argued that these findings indicate it to be beneficial to update the modelled state with satellite-derived observations using a data assimilation mechanism, such as the EnKF. This view would be consistent with the findings from past assimilation studies (Huang *et al.*, 2008; Pipunic *et al.*, 2008). However, although promising, this investigation, like many of those undertaken previously, is based upon various assumptions. For instance, the assumptions made during the processing of EO products may not be consistent with those made in land surface models. Data assimilation is reliant on accurate prediction of observation uncertainty; biased observations will cause departure from the correct model state (Quaife *et al.*, 2008). In this investigation perturbations appended to the observations were constrained by a fixed uncertainty, whereas observation errors are most likely to be spatially and temporally variable. Indeed, during the daytime over desert and semi-arid regions SEVIRI retrievals are reported (Trigo *et al.*, 2008b) to regularly fail the 2.0K LandSAF accuracy target. The uncertainty to which LST can be stated is relevant to the errors in surface-to-atmosphere fluxes. For example, a 1.0K LST error can lead to a 10% error in ET (Moran and Jackson, 1991), whereas a 10% error in H can result from a 0.5K LST error (Brutsaert *et al.*, 1993). Finally, a 1.0 to 3.0K error in LST can lead to errors as much as $100 Wm^{-2}$ in heat fluxes (Kustas and Norman, 1996).

For retrievals from instruments onboard polar orbiting satellites however, such as AATSR or MODIS, the longer duration between available observations, compared with the frequent retrievals from SEVIRI, suggests an alternative observation operator should be implemented to directly manipulate a variable with a longer temporal memory than LST; soil temperature for example. Certainly this is a possibility which may warrant future examination. The purpose of this investigation though, has been to understand whether a change in the heat and water fluxes between the surface and atmosphere

could be brought about by manipulating the surface temperature modelled by JULES. Having shown this, it is conscientious to consider what the implications are of applying the current assimilation strategy in the model.

The West African study zone overlays a hotspot region of strong land/atmosphere coupling as identified by Koster *et al*. (2004). In the experiment presented here data assimilation of LST has resulted in a mean reduction in surface soil moisture over this region during the modelling period. If soil moisture falls below a critical value then a partial closing of stomata results - as a preventative measure against excessive water loss. Stomatal conductance, which is affected not only by the availability of moisture in the soil, but also the quantity of PAR (Essery *et al.*, 2003), controls the rate of ET. Soil moisture anomalies can translate into precipitation anomalies through the ET rate which drives atmospheric water vapour pressure, thereby influencing regional climate change (Shukla and Mintz, 1982; Taylor *et al.*, 2010). Coupled to the Hadley Centre Unified Model, the change in soil moisture modelled by the land-surface scheme could feedback on the precipitation regime influencing the predictions of pluvial and drought conditions, which in turn could affect the distribution of vegetation, surface albedo, and subsequent surface evaporation.

A reduction in soil moisture, and corresponding reduction in ET, has the potential to impact the carbon balance of the region, since Rosenzweig (1968) postulated a positive relationship between ET and NPP. In section 2.3.2 it was shown that the interannual variability of NPP as modelled by JULES was greater than that of heterotrophic respiration over Africa. The implication of any decrease in NPP would be a corresponding decrease in NEP, thus weakening the uptake of carbon by the terrestrial biosphere in this region. Future climate change, driven by increased concentrations of greenhouse gases, is likely to enhance hydrological responses in these hotspots of strong

land/atmosphere coupling, although large uncertainties remain (Notaro, 2008). It is thus essential that such feedbacks are represented in climate models as accurately as possible if future climate change is to be predicted with confidence.

4.5. Conclusions

The aim of this study has been to investigate whether the development of a data assimilation scheme for the JULES model using the EnKF is both feasible, and could lead to tangible improvements in the estimation of surface fluxes. Having established a deficiency in the simulation of LST - an integral component in the calculation of surface-to-atmosphere heat fluxes and particularly sensitive to surface moisture conditions - observations from SEVIRI were integrated into the model over the African continent during 2007. The intention was to address two specific questions: i) can a reduction in the uncertainty of surface energy fluxes be achieved by constraining simulations of LST with observation data; and ii) how does the assimilation of satellite-derived LST affect the quantification of soil moisture.

Findings indicate that by directly manipulating LST, surface energy and water fluxes could be constrained. Specifically, reductions in RMSEs were achieved when sensible and latent heat flux simulations with data assimilation were compared with Eddy Covariance measurements from four flux towers located across Africa, as opposed to open loop modelling. Over a region of West Africa, simulations of soil moisture were also more comparable against an independent dataset with data assimilation than without, suggesting soil moisture was overestimated by open loop modelling; a result which could have profound implications for using the JULES model to predict climate over this hotspot of strong land/atmosphere coupling.

To my knowledge, this represents a first attempt at constraining the predictions of surface fluxes of heat and water from JULES by integrating remotely sensed values

with the EnKF. This is an encouraging development which warrants further research to investigate the assimilation of vegetation indices, or even reflectances from EO satellites. Indeed, the potential of expanding these developments to the JULES framework into an operational system should be explored. In the context of this research project though, the data assimilation skill acquired could be applied to constrain the model when addressing some scientific problem.

Chapter 5

Fuel moisture content simulation over African savannahs

Evidence has been presented in previous chapters to indicate that the JULES model is an adequate tool for modelling the physical processes of the terrestrial biosphere, and that model simulations can be improved by incorporating instantaneous measurements from satellite. One element that the current operational model framework lacks is the capability to model the fire regime, a key land/atmosphere feedback and an important control on vegetation structure and distribution. Africa is responsible for a large proportion of global biomass burning, but quantification is subject to considerable uncertainty. A significant development in this respect would be to improve the prediction of one of the most important drivers of fire occurrence and propagation: fuel moisture content (FMC).

This chapter investigates whether the model skill developed in previous chapters can be applied to derive a first modelled dataset of FMC over the mixed tree/grass environments of the African continent. The approach taken here was to construct a surface dryness index to represent the moisture content of the fuel, based on the ratio of NDVI to LST. In this context, two specific questions will be addressed: i) can fuel moisture content be satisfactorily estimated across the savannah landscapes of Africa using a land surface modelling approach; and ii) can this approach be enhanced by utilising data assimilation of satellite-derived LST.

5.1. Introduction

Fire is one of the most important disturbances in terrestrial ecosystems, because it is integral to global biogeochemical cycling and vegetation succession (Nepstad *et al.*,

1999; Cochrane, 2003). In mixed tree/grass environments, such as the African savannahs, fire suppresses woody cover, and promotes landscape heterogeneity. As savannahs cross a precipitation gradient the fire regime, which experiences return intervals of typically one to five years, becomes the main regulator of the structure and composition of vegetation, maintaining woody cover below the climate potential (Sankaran *et al.*, 2008). These are among some of the most frequently burnt ecosystems, and are major contributors to the atmosphere of trace greenhouse gas emissions and radiatively active aerosols, which affects atmospheric chemistry and thus climate (Scholes *et al.*, 1996; Andreae and Merlet, 2001).

Despite the importance of fire activity in the African savannahs to the global climate system, the conclusion from previous modelling studies (Thonicke *et al.*, 2001; Lehsten *et al.*, 2009) was that significant uncertainty was associated with fire modelling. One of the most sophisticated fire models is the SPread and InTensity of FIRE (SPITFIRE) model (Thonicke *et al.*, 2010), which while generating encouraging simulations remains driven by the same simplified estimations of key fuel variables affecting fire ignition and propagation as identified for previous models (van der Werf *et al.*, 2006; Lehsten *et al.*, 2009). Improving fire model predictions is a prerequisite for reducing the uncertainty in the carbon cycle of savannah ecosystems, and indeed globally. What is more, the fire regime is dynamic and could experience changes in frequency and intensity driven by changes in climate, economy and demography (Hoffmann *et al.*, 2002). It is therefore imperative that an improved ability to accurately understand and predict this important disturbance is a priority, to reduce uncertainties in climate modelling.

FMC is considered one of the three most important drivers – together with fuel load and ignition source - influencing fire occurrence and propagation (Chuvieco *et al.*,

2004a; Arora and Boer, 2005; Hao and Qu, 2007). However, due to the complexity of plant-water interactions it is difficult to quantify. Methodologies to derive FMC include field sampling and the calculation of meteorological danger indices (MDIs). While both these traditional methods have been exhaustively employed, they have disadvantages. The former method for example, is both labour intensive and costly, and can only provide measurements at a local scale (Hao and Qu, 2007). Since samples need to be oven-dried, real-time estimation is also not possible (Aguado *et al.*, 2007). In the case of MDIs, three main problems are evident. Firstly, MDIs cannot accurately model the variability in soil moisture, or the drought resistance of live vegetation (Chuvieco *et al.*, 2004a). Secondly, they are formulated from measurements which may be acquired from weather stations not appropriate to the study site, resulting in interpolation errors (Aguado *et al.*, 2007). Finally, since they are calibrated for use in specific biogeographical areas, when applied elsewhere inconsistent predictions may result (Aguado *et al.*, 2007).

In recent years an alternative approach for deriving FMC over large geographical regions has gained momentum, namely the use of remote sensing. Vegetation indices in particular have been used to determine the moisture content of live fuel (Chuvieco *et al.*, 2002; Verbesselt *et al.*, 2007). In fact, for herbaceous species good correlations have been found, although this could not be repeated for shrubs and trees (Chuvieco *et al.*, 2004b; Verbesselt *et al.*, 2007). The use of satellite-derived vegetation indices to derive FMC does however have one significant drawback: they are most sensitive to changes in chlorophyll content, a characteristic which shows no discernible change in dry matter (Verbesselt *et al.*, 2007). Indeed, Chuvieco *et al*. (2003) and Hao and Qu (2007) argue that FMC cannot be reliably retrieved from reflectance measurements alone, since dead material cannot be accurately estimated in this way.

The application of land surface modelling would enable the moisture content of both live and dead vegetation to be estimated, providing potentially global predictions at a high temporal resolution. In addition, a modelling approach has the advantage of not being subject to missing data limitations associated with EO retrievals, such as cloud cover or instrumentation problems. The approach taken here was to derive an aggregated FMC; whereby the absorption and evaporation which control the moisture content of dead elements (Verbesselt *et al.*, 2007) can be modelled as a function of meteorological and soil conditions, and the moisture content of live elements can be represented by a surface dryness index based on the ratio between NDVI and LST. The rationale for the latter component is that as plants dry out the NDVI signal decreases since the chlorophyll content is reduced (Verbesselt *et al.*, 2006), whereas LST increases as a result of a reduction in the cooling effect of evapotranspiration (Chuvieco *et al.*, 2004b). Numerous studies (Sandholt *et al.*, 2002; Chuvieco *et al.*, 2004b; Snyder *et al.*, 2006) have shown that this ratio between NDVI and LST results in statistically stronger correlations to FMC than either of these variables separately.

This investigation utilises model skill developed in previous chapters to derive FMC over the savannah landscapes of Africa using a land surface modelling approach. In the JULES model, FMC was simulated as a linear function of abiotic conditions in combination with the ratio between remotely sensed NDVI data forced into the model and model simulated/assimilated LST. The precise form of this relationship was calibrated using *in situ* measurements acquired during the field campaign to KNP described in section 3.2. Using this relationship a map of daily FMC over the mixed tree/grass landscapes of Africa was produced, and these model predictions were validated against measurements from a data archive covering three alternative locations within the KNP.

5.2. Materials and methods

5.2.1. Study area

The establishment of prescribed burning on EBPs within the KNP means the interaction between fire and vegetation has been continuously studied since 1954, justifying the choice of study area for model calibration and validation. The KNP experiences extended wet and dry periods, whereby annual precipitation for six to twelve consecutive years is either higher or lower than the long-term mean, significantly influencing fuel loads (van Wilgen *et al.*, 2004). During the 1990s the burning regime of the park changed to allow naturally ignited fires to burn unhindered, with human ignited fires carefully managed; prior to this, a policy of rotational burning approximately once every three years in late winter or early spring had been implemented (van Wilgen *et al.*, 2004).

The EBPs are grouped together into strings, of which four are located in each of the four principal landscapes of the park: Mopani; Pretoriuskop; Satara; and Skukuza (Figure 5.1). Each landscape is characterised by different physiology, phenology and structure; with soils of different texture, hydrological properties, and nutrient cycling. In the southern most section, Pretoriuskop can be classified as Lowveld Sour Bushveld overlying granite geology dominated by tall *Terminalia sericea* trees, and experiencing mean annual precipitation of approximately 700-750mm. Further north, the Satara site can be classified as *Sclerocarya birrea* / *Acacia nigrescens* savannah overlying basalt geology, with mean annual precipitation of approximately 500-550mm. Finally, the northern most site – Mopani – is dominated by *Colophospermum mopane* trees also overlying basalt geology, with mean annual precipitation of 450-500mm (Biggs *et al.*, 2003; Govender *et al.*, 2006). The Skukuza site has been described previously in table

3.2. Annual, biennial, or triennial burn treatments are replicated for each string within each group.

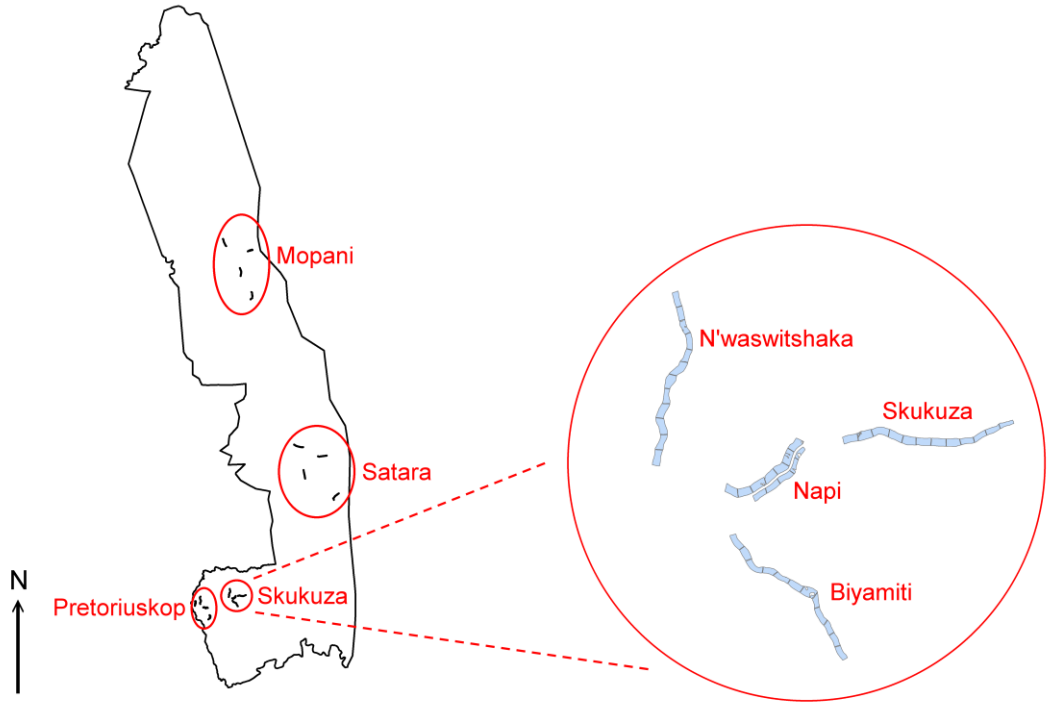

Figure 5.1: Location of the four groups of EBPs within the KNP, each containing four strings where treatments are replicated.

In order to calibrate the JULES model, measurements of FMC were acquired from the Skukuza string during the field campaign which took place from 23rd July 2009 to 7th August 2009 and has been described in detail in section 3.2. This string consists of EBPs ranging in size from 3.62 ha to 7.63 ha with a mean of 6.01 ha (Table 5.1). An indication of the treatments applied to this string is also provided in table 5.1. To validate the model, simulations of FMC were compared against measurements from EBPs which constitute the strings at Mopani, Pretoriuskop, and Satara; these were acquired by the South African National Parks Authority (SANParks) and are stored in archive datasets, made available courtesy of Scientific Services, Skukuza.

Table 5.1: Burn schedule for the Skukuza string. The 'burn code' refers to the month of treatment together with the interannual frequency; where B1 is an annual burn, B2 is a biennial burn, and B3 is a triennial burn. The date of the previous burn prior to the beginning of the field campaign is given.

Plot number	Area (ha)	Burn code	Date of previous burn
1	6.52	October B2	13/10/2006
2	7.14	December B2	Accidental fire 2005
3	7.63	February B2	27/02/2007
4	6.75	August B2	20/08/2008
5	6.69	April B2	12/05/2009
6	6.50	August B1	20/08/2008
7	6.86	Control	No burn
8	6.43	December B3	03/12/2003
9	4.69	October B3	13/10/2006
10	4.62	February B3	04/03/2008
11	4.66	April B3	12/05/2009
12	3.62	August B3	07/08/2006

5.2.2. Field methodology

During the field campaign, FMC was measured across four separate EBPs of the Skukuza string: plot six, plot eight, plot ten, and plot twelve (Figure 5.2) on 27th July, 30th July, 2nd August and 5th August respectively. Each approximately rectangular EBP was systematically sampled by taking measurements every 50m along four transects, totalling 28 samples per plot. Since the herbaceous layer contributes the bulk of the fuel (Shea *et al.*, 1996) within the EBPs, and as any burning consumes the grass layer and scorches the shrub understory but has little effect on the tree canopy (Scholes *at el.*, 2001), it was deemed satisfactory to simply sample the herbaceous layer of each plot.

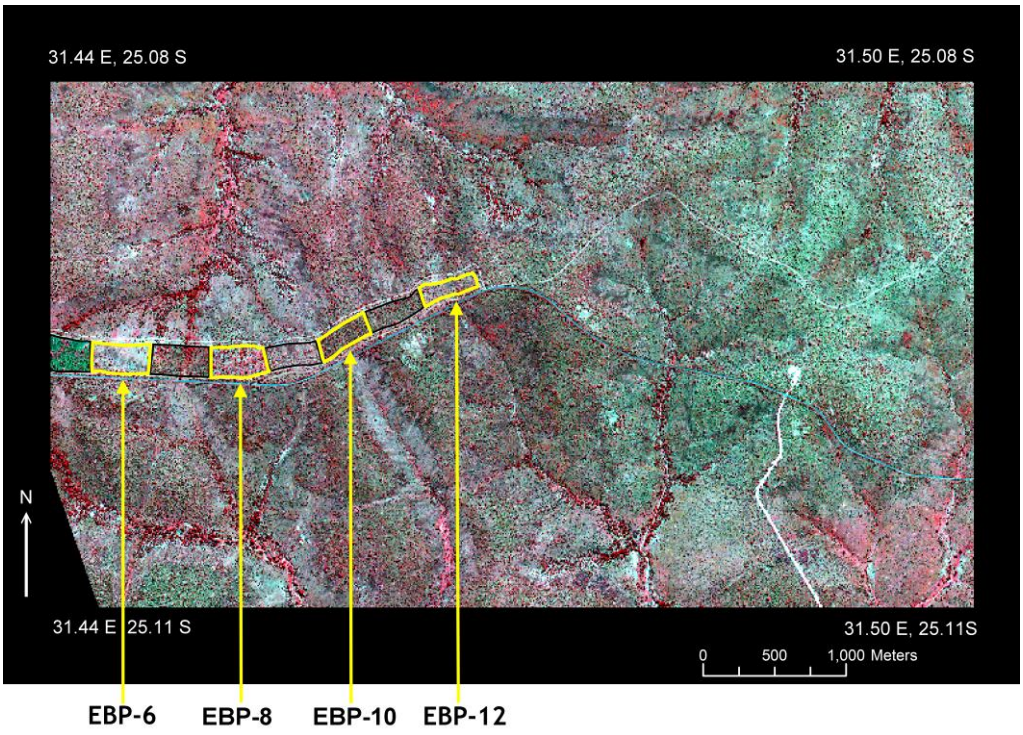

Figure 5.2: Location of the four EBPs within the Skukuza string where FMC measurements were collected during the field campaign.

Each herbaceous sample, which included both live and dead components, was a representative selection of all grass species within the 0.5m × 0.5m sample quadrat. Samples were stored in air-tight jars; both jar and content were weighed prior to drying to first obtain the wet weight of the samples, and then again following oven-drying at 60°C for 48 hours to obtain the dry weight. FMC was calculated as the percentage of moisture over the weight of the dry matter following the methodology outlined in previous studies (Chuvieco *et al.*, 2003; Aguado *et al.*, 2007):

$$FMC = 100\% \times \left(\frac{W_w + W_d}{W_d}\right) \quad (25)$$

Where W_w is the weight of the biomass prior to oven-drying, and W_d is the weight of the dry matter. The number of sampling events was restricted to four due to limitations

which included the duration of the field campaign, the required time to dry samples, and the limited oven space available.

In addition to the collection of FMC measurements, at each sample point LST of the grass scene was measured in accordance with methodology outlined in section 3.2, and soil moisture was collected using a Delta-T ML2 Theta probe (Figure 5.3). The probe estimates the volumetric water content of the top 60mm of the soil by measuring the difference between the internal voltage of the probe and that reflected by the five rods to derive the dielectric constant of the soil. Measurements were taken every second and averaged every minute, with the mean taken only once the readings from the probe had reached equilibrium; data outside this equilibrium was discarded.

Figure 5.3: Photograph illustrating the Delta-T ML2 Theta probe set up to measure soil moisture.

5.2.3. Experimental setup

For the calibration experiment, a linear regression equation was developed to describe the observed FMC from the most appropriate combination of the ratio between NDVI and LST, days since the last precipitation event, soil moisture, and meteorological conditions. The Akaike Information Criterion (AIC) was used as the method to accept or reject variables, with the model having the minimum AIC producing the best

goodness-of-fit. This choice of potential predictors was selected based on evidence from previous studies (Sandholt *et al.*, 2002; Chuvieco *et al.*, 2004b; Snyder *et al.*, 2006; Verbesselt *et al.*, 2007) regarding the characteristics which influence the moisture content of herbaceous fuel. As discussed previously, LST and soil moisture were measured at each sample plot, whereas the meteorological conditions were acquired from the Skukuza Flux Tower, described in section 3.2.1 and situated at a mean distance of approximately 10km from the string. For each sample, the nearest 30-minute snapshot to the time the sample was collected was retrieved from the flux tower. As illustrated in section 3.2.7, in the case of downward long-wave radiation bilinearly interpolated NCEP Reanalysis II data (Kalnay *et al.*, 1996) replaced the missing data from the flux tower.

Finally, the daily NDVI for the EBP sampled on that day was calculated as the normalised transformation of the NIR to red reflectance ratio extracted from the level-2 daily 250m surface reflectance product MOD09GQ according to:

$$NDVI = \frac{\rho_{NIR} - \rho_{red}}{\rho_{NIR} + \rho_{red}} \tag{26}$$

Where ρ_{red} is the red reflectance (band 1) and ρ_{NIR} is the NIR reflectance (band 2). The NDVI signal for a given EBP was taken as the mean signal of all the pixels which overstrike the plot (see Figure 5.4) weighted by the percentage by which each respective pixel intersected with the plot. Although only the herbaceous layer was sampled since the trees typically do not burn (Scholes *et al.*, 2001; Govender *et al.*, 2006), this represents the effective FMC of the whole plot. As such, it was deemed appropriate to apply the NDVI signal of the entire EBP which encompasses reflectance from the tree canopy and bare soil endmembers in addition to the grass endmember. If cloud cover

prevented the retrieval of a signal on a given day then the NDVI was interpolated from values for previous and subsequent days.

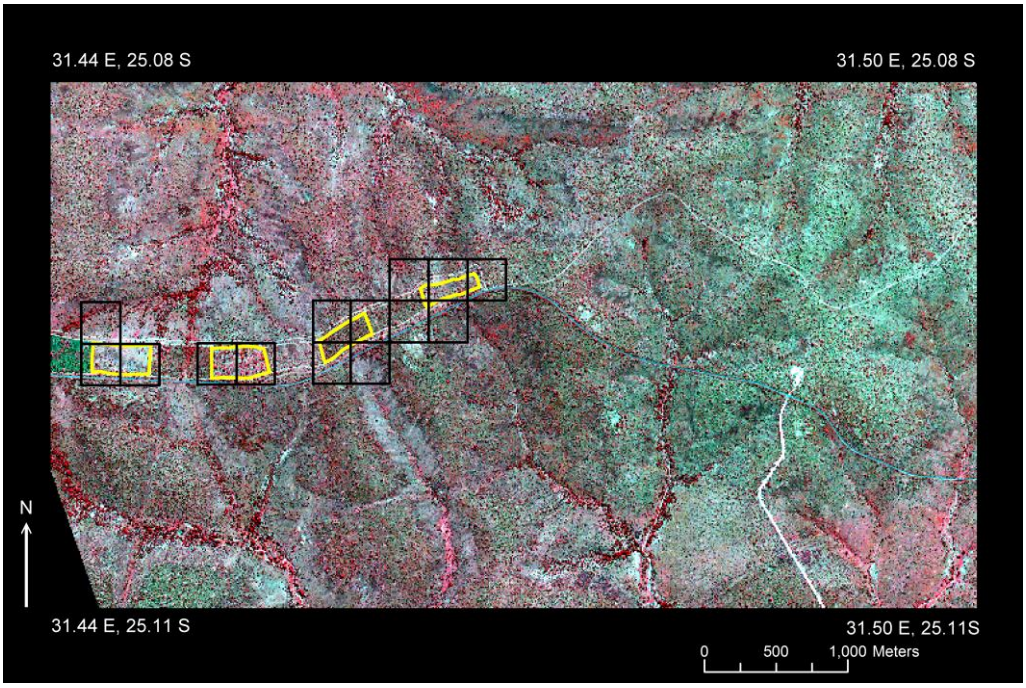

Figure 5.4: Overstrike of the MODIS 250m pixels from the surface reflectance product MOD09GQ (black squares) which intersect the EBPs (yellow polygons) sampled during the Skukuza field campaign.

The regression equation was integrated into the JULES model to enable simulation of FMC over a wide geographical area. Specifically, the model was set up in the same vein as described in section 4.2.3 at an hourly time-step from 2001 to 2009, with and without SEVIRI LST assimilated into the model. In this case though, the chosen spatial resolution was 0.5° x 0.5°, since only a sub-region of the African continent was considered - the mixed tree/grass landscapes. These were reasoned to be most appropriate to the calibrated form of the regression equation, and included the IGBP land cover classes of woody savannas; savannas; grasslands; croplands; and the cropland/natural vegetation mosaic (Figure 5.5). As previously, the model was spun-up first by repeating the years 2000 to 2004 inclusive until soil temperature and moisture conditions were equilibrated. NDVI data was acquired from the MODIS 16-day 0.05°

MOD13C1 collection; this was aggregated to 0.5° and time-interpolated to provide daily estimates. Since LST collected during the model calibration was centred on local solar noon, this was the time chosen for the derivation of a daily FMC estimate in the regional simulation. These estimates were compared against measurements acquired from EBPs situated in the Mopani, Pretoriuskop and Satara landscapes of the KNP. The archive of field measurements made available by SANParks are inscribed with the date, and location, and cover all seasons and years during the 2001 to 2009 period.

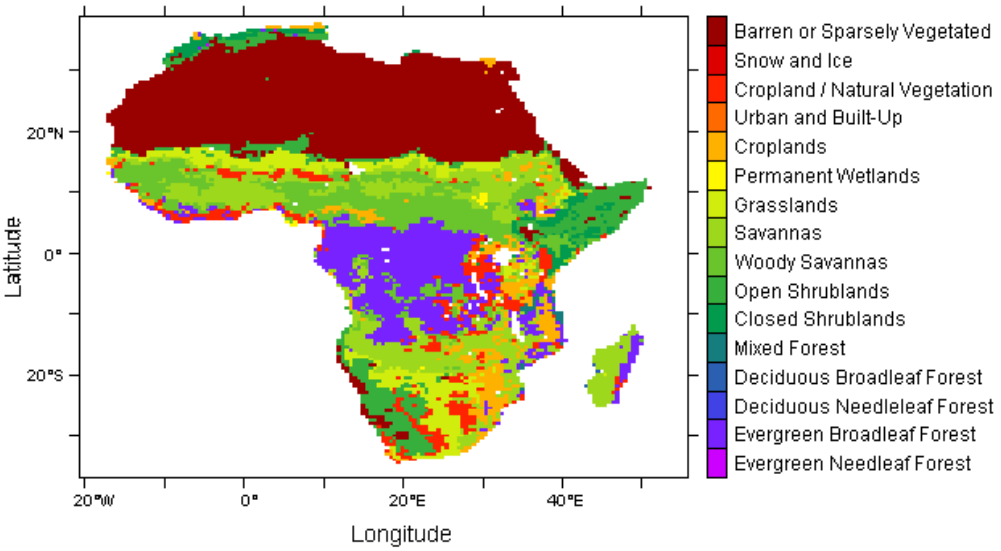

Figure 5.5: IGBP land-cover classes for Africa at 0.5° spatial resolution.

5.3. Results

5.3.1. Model calibration

To simulate FMC a multiple linear regression model was derived, whereby the AIC was used as the method to accept or reject variables (Table 5.2), which described the observed values. Potential predictors included the ratio between NDVI and LST to represent surface dryness, days since the last precipitation event, soil moisture,

downward long-wave radiation, downward short-wave radiation, air temperature, specific humidity, and wind speed.

Table 5.2: Multiple linear regression of modelled FMC against fuel moisture predictors: NDVI / LST (Φ); days since previous precipitation event (DP); wind speed (WS); specific humidity (Q); downward short-wave radiation ($SW_{\downarrow}$); soil moisture (M); downward long-wave radiation ($LW_{\downarrow}$); and air temperature (T_A). The model with the minimum Akaike Information Criterion (AIC) has the best goodness-of-fit and was selected as the calibration equation.

Model	***r***	r^2	**RMSE**	**Predictors**	**AIC**
1	0.828	0.685	20.31	Φ	660.33
2	0.882	0.777	16.99	Φ, DP	624.14
3	0.905	0.820	15.28	Φ, DP, WS	602.96
4	0.918	0.843	14.17	Φ, DP, WS, Q	589.34
5	0.925	0.856	13.58	Φ, DP, WS, Q, $SW_{\downarrow}$	581.88
6	0.934	0.872	12.72	Φ, DP, WS, Q, $SW_{\downarrow}$, M	571.35
7	0.934	0.872	12.72	Φ, DP, WS, Q, $SW_{\downarrow}$, M, T_A	573.35
8	0.934	0.872	12.72	Φ, DP, WS, Q, $SW_{\downarrow}$, M, T_A, $LW_{\downarrow}$	575.12

This model indicates that the linear combination of a surface dryness index, soil moisture and climate variability is responsible for almost ninety percent of the FMC variance. The RMSE between the predicted FMC and *in situ* observations was 13.38, and the exact form of the calibration equation is expressed as:

$$FMC = 42000\,\Phi - 0.26\,DP + M - 0.10\,SW_{\downarrow} - 3.96\,WS + 2265\,Q - 11.96 \qquad (27)$$

Where Φ is the ratio between NDVI and LST (T_{sfc}), *DP* is the number of days since a last precipitation event, *M* is the soil moisture, $SW_{\downarrow}$ is the downward shortwave radiation, *WS* is the wind speed, and *Q* is the specific humidity. Figure 5.6 illustrates the predicted FMC, using equation (27), plotted against the *in situ* observations collected

during the field campaign. Much of the observed FMC was grouped lower than 20%, with the highest values acquired following the rainfall event on 2nd August.

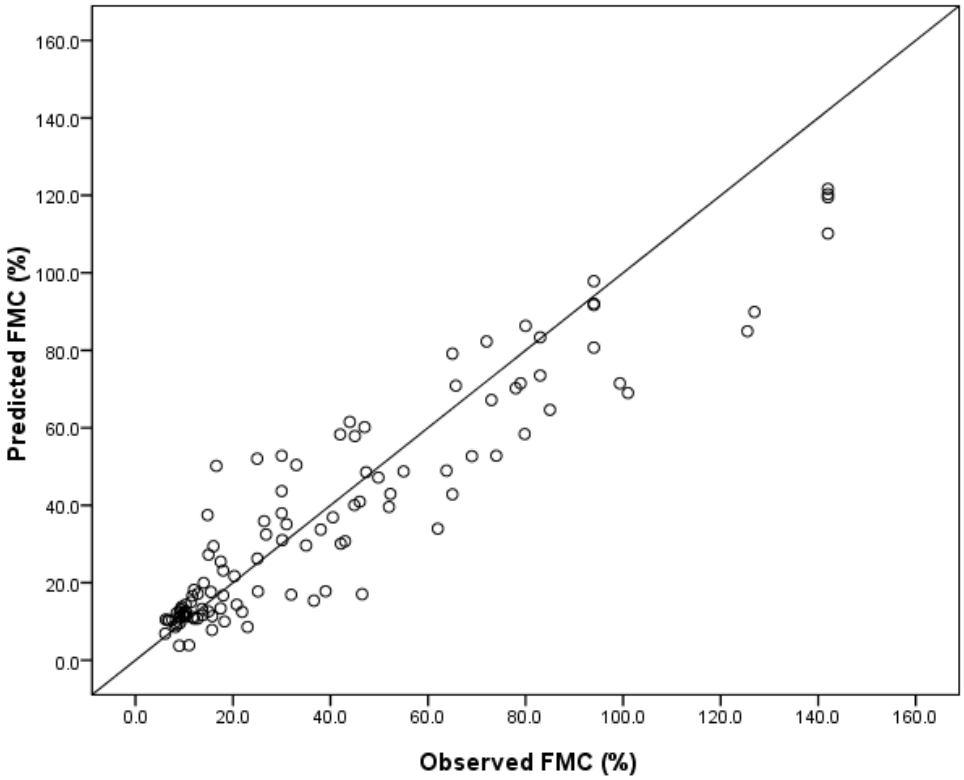

Figure 5.6: Predicted FMC derived from regression vs. in situ observations taken at Skukuza during the field campaign in the Kruger National Park, South Africa, between 23rd July and 7th August 2009. The observations were used in the development of the regression equation rather than as an independent validation dataset.

5.3.2. Model simulation and validation

Equation (27) was integrated into the JULES framework and FMC over the mixed tree/grass landscapes of Africa were henceforth simulated. Validation of the model simulations was performed against an archive of field measurements acquired from EBPs within three landscapes of KNP distinct from the Skukuza calibration site: Mopani, Pretoriuskop and Satara. Although exact collection times for the field measurements from these validation sites were not recorded, it was confirmed to be

around local noon (Navashni Govender, personal communication). The simulation of FMC by JULES was performed with and without LST data assimilation. The impact on one of the key predictors, soil moisture, is illustrated in figure 5.7. The estimates of mean soil moisture from the three validation landscapes are consistently lower, and display smaller amplitude, with assimilation than without.

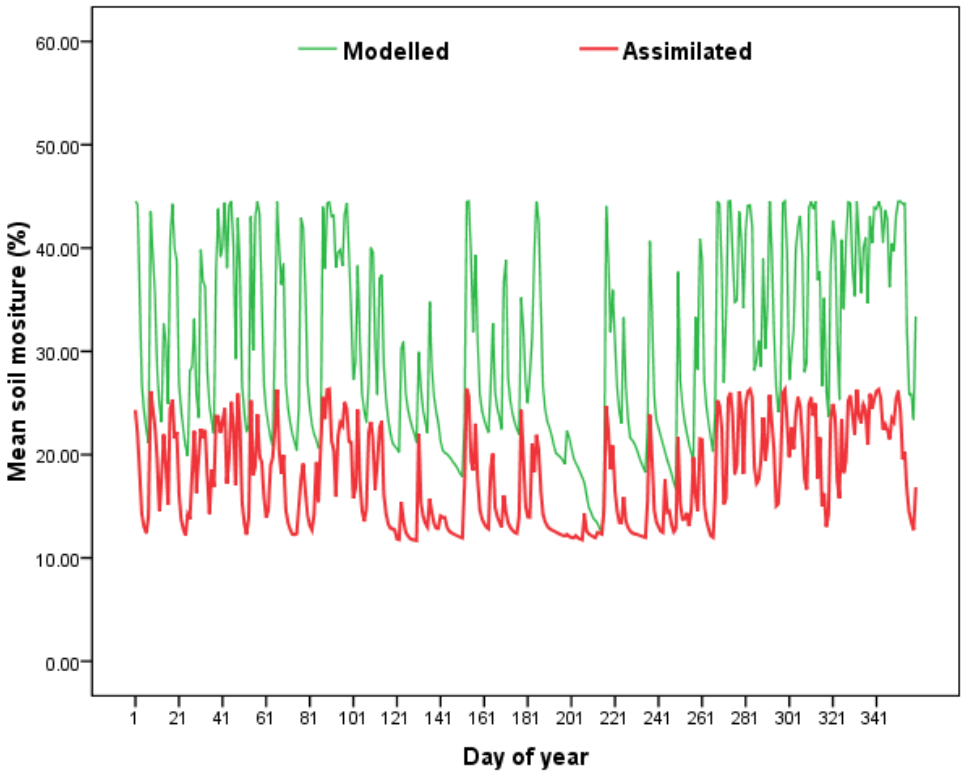

Figure 5.7: Time series of mean soil moisture during 2007 for grid-cells covering the validation landscapes of KNP for both open loop modelling and model simulations following LST assimilation.

When LST is assimilated into the JULES model the predicted FMC shows a strong correlation (r = 0.826, P > 0.01; N=231) with the field measurements acquired from the three KNP landscapes (Figure 5.8), with a higher coefficient of determination (0.683) than without data assimilation (0.609). Furthermore, the RMSE for simulated FMC with respect to the field measurements was reduced from 33.1% to 23.3% with LST data assimilation compared with open loop modelling. Despite these encouraging results,

figure 5.8 does show a tendency for the model to over-estimate the field measurements, particularly for lower values of FMC; although, this over-estimation would be more pronounced without data assimilation due to higher soil moisture estimates in equation (27).

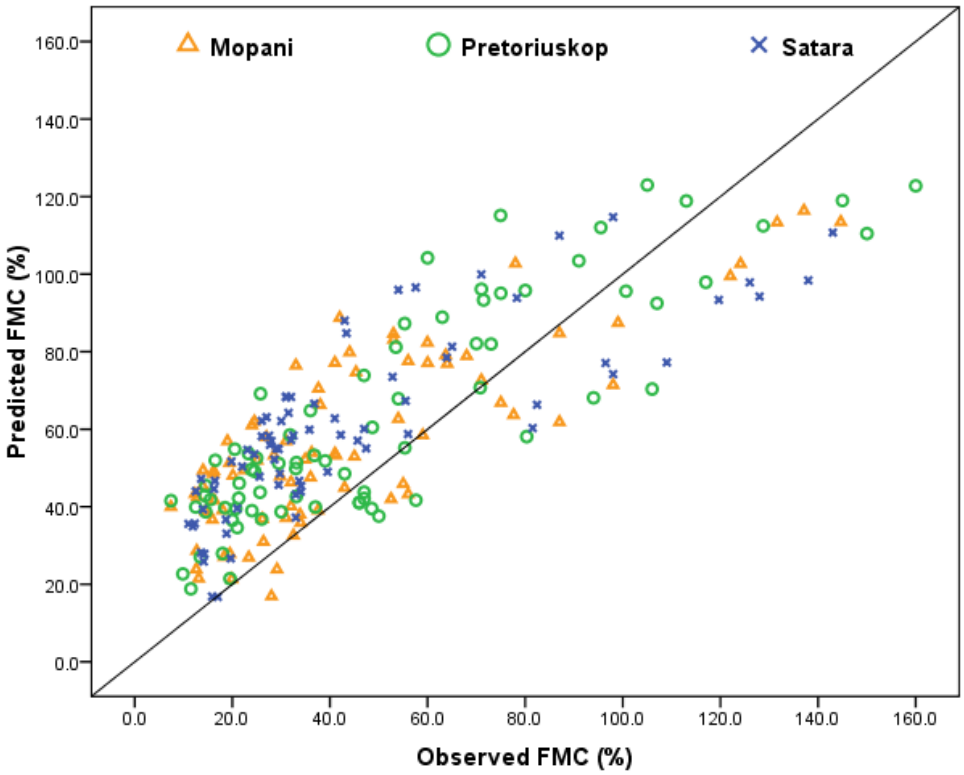

Figure 5.8: Predicted FMC as simulated by the JULES model vs. in situ observations acquired from EBPs within three landscapes of KNP: Mopani, Pretoriuskop and Satara from 2001 to 2009 inclusive. The field measurements, which can be considered as independent datasets, were collected by SANParks and made available courtesy of Scientific Services, Skukuza.

These r^2 values are comparable with previous attempts to derive a FMC index. For example, in the study over central Spain by Aguado *et al.* (2007) values between 0.44 and 0.57 were produced when derivation of dead FMC using MDIs were validated. In another study, a variety of remotely sensed vegetation and water indices were tested against field measurements of FMC from the same EBPs in the KNP (Verbesselt *et al.*,

2007), resulting in r^2 values which ranged between 0.25 and 0.75. While the attempt described in this chapter to develop a predictor for FMC has not resulted in better estimations in terms of r^2 values, what it does represent is a robust technique which can estimate total FMC (both dead and live) unhindered by cloud conditions or satellite instrumentation problems, enabling a first map of daily FMC over a wide geographical region to be produced.

Figure 5.9 illustrates the mean daily FMC for the four quarters of 2007, where daily FMC is determined at local noon. When applying the model over the northern hemisphere savannahs the highest values were simulated in the 3rd quarter of the year, whereas over the southern hemisphere savannahs the highest values were simulated in the 1st quarter. These periods correspond to the height of the wet season in the respective regions. Conversely, the lowest values were simulated during the height of the respective dry seasons – the 1st quarter in the northern hemisphere, and the 3rd quarter in the southern hemisphere.

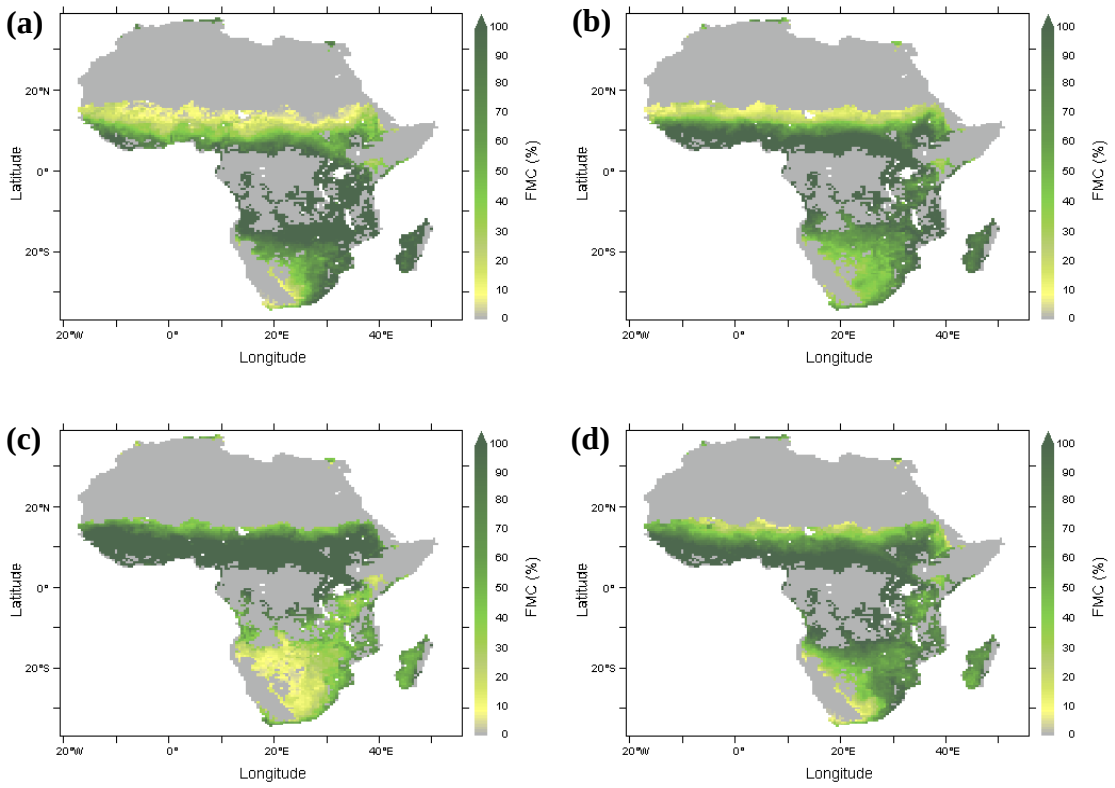

Figure 5.9: Mean daily FMC simulated at 0.5° over the mixed tree/grass landscapes of Africa during 2007: 1st Quarter (a); 2nd Quarter (b); 3rd Quarter (c); 4th Quarter (d).

5.4. Discussion

FMC is an important characteristic in vegetation fires. Part of the energy required to start a fire and to ignite adjacent fuels is used to evaporate water; hence FMC is inversely related to the probability of ignition and propagation (Chuvieco *et al.*, 2002). Indeed, if the fuel is too moist (greater than the 'moisture of extinction') the rate of spread of the fire front passing through the fuel bed can be reduced to zero, since all the energy is consumed in the process of evaporation (Thonicke *et al.*, 2001). Fire intensity is also a property of a fire that is dependent on the moisture content of the fuel. This displays seasonality, with the most intense fires occurring late in the dry season when the fuel bed is at its driest and combustion is more efficient (van Wilgen *et al.*, 2004; Govender *et al.*, 2006). Flaming combustion dominates when FMC is low, with a higher fraction of carbon emitted as CO_2; whereas when FMC is high smouldering combustion

dominates, and the emissions of trace gases are proportionally higher (Andreae and Merlet, 2001). Although the burning of savannahs is not a net source of carbon due to subsequent vegetation re-growth, biomass burning is a significant source of radiatively active aerosols and trace gases, such as methane and carbon monoxide (Andreae and Merlet, 2001). Reducing uncertainty is therefore an important mission, with the improvement in FMC prediction a crucial prerequisite.

Fire is often neglected in land surface models, with estimates of biomass burning emissions thus absent (Williams *et al.*, 2007). Where fire is included, its derivation often depends simply on prescribed loss rates or simple empirical algorithms. Where a fire model is more complex, FMC is often based on simple surrogates such as soil moisture (Venevsky *et al.*, 2002; Arora and Boer, 2005). Even the latest fire models, such as SPITFIRE (Thonicke *et al.*, 2010) which relies on a combination of MDI - such as the Nesterov Index - to derive dead FMC, and soil moisture to derive live FMC, may benefit from a more representative process-based approach. Previous studies (Chuvieco *et al.*, 2004b; Verbesselt *et al.*, 2007) have attempted to utilise remote sensing to estimate live FMC. While there is justification in this approach – since it overcomes many of the limitations of both field based methodology and MDIs - it fails to account for presence of dead fuel and is constrained by both the availability of cloud-free images and the operational reliability of the satellite sensor. The approach taken in this study minimises these limitations by overcoming the reliance on usable retrievals, while ensuring the capability to capture moisture content changes at a high temporal resolution at regional or even global scales.

Findings indicate that the methodology developed here to derive total herbaceous FMC can provide a robust alternative to the use of MDIs or straightforward reliance on satellite-derived data; with strong correlation between modelled and *in situ* observations

when validated across numerous plots within the KNP. The landscapes of the KNP are classified differently in terms of biotic and abiotic controls; and since figure 5.8 illustrates the FMC within each of these to be modelled by JULES with a similar predictability, the implication is that FMC over different tree/grass landscapes across the continent of Africa could potentially be adequately mapped on a daily basis. As a matter of fact, a first daily record of FMC covering the African savannahs was produced; the seasonal differences (Figure 5.9) would appear to be realistic and thus encouraging for the credibility of the methodology. What is more, the implementation has been seamless and it facilitates continuous derivation due to time-interpolation of NDVI and internal calculation of LST from the surface energy balance equation. In addition, this investigation has provided an appropriate case study for illustrating the impact of assimilating LST into the model.

Despite these encouraging results the methodology presented here is subject to a number of assumptions. Firstly, the Skukuza string is considered an outlier in terms of the variability across the site in the texture and sodium content of the soil (Navashni Govender, personal communication), which are key determinants of the vegetation structure and composition. This choice of string however, was determined as a matter of logistics, as it was the most conveniently located in terms of access from the road network and hence the rest camp. Moreover, figure 5.8 provides evidence that the soil at Skukuza does not preclude a generalisation of the method. Secondly, by taking measurements around solar noon the inference is that maximum daily LST is a predictor of FMC, and thus a diurnal trajectory of the moisture content of the fuel is not a viable outcome. There is though validity in this assumption, since diurnal variability is negligible in comparison to seasonal variability (Verbesselt *et al.*, 2007). Thirdly, the derivation of FMC is based on a combination of instantaneous conditions and those

which have exerted an influence over a longer time period, such as soil moisture. It may be, that a more appropriate representation of the moisture content of the fuel could have been achieved by only considering longer memory effects, such as the mean humidity and mean solar radiation since the last precipitation event for example; this could be worthy of future investigation.

The final, and perhaps most fundamental, assumption relates to the scaling inconsistency when comparing modelled FMC with field measurements acquired from Mopani, Pretoriuskop and Satara. The field measurements correspond to mean FMC over designated EBPs, which have an average size of approximately seven hectares; the modelled FMC is derived for grid-boxes of 0.5°. However, neither meteorological input variables nor soil moisture were available at an equivalent fine spatial resolution to the respective burn plots. Conversely, flux tower locations across the continent could not be considered as potential validation sites since FMC measurements have not been compiled at any of these. As such, this constraint to the methodology for validating the modelled FMC remains a caveat to any interpretation of these findings.

Savannahs exhibit strong wet and dry seasonality, and are some of the most frequently burnt ecosystems; yet considerable uncertainty exists in determining climate change in these environments (Williams *et al.*, 2007). With climate scenarios predicting warmer and windier conditions, the implication is for an increase in drying and accumulation of fuel, thereby increasing fire frequency, intensity, and thus emissions (Hoffmann *et al.*, 2002). Signatories to the United Nations Framework Convention on Climate Change (UNFCCC) are required to provide emission estimates; this underlines the need to develop more accurate procedures for calculating emissions from biomass burning. Here, an alternative method for deriving the critical fire variable – FMC - has been presented; with potential for interfacing this model output with a designated fire

model to reduce the uncertainty in modelling fire dynamics, and resultant emissions. Indeed, the SPITFIRE model is scheduled for inclusion in the JULES model. Although the timing of this is indeterminable, the possibility exists to utilise the modelling approach for determining FMC in this coupling.

5.5. Conclusions

The purpose of this investigation was to act as a case study for examining the application of model skill developed previously. Specifically, a first modelled dataset of FMC over the mixed tree/grass environments of the African continent. FMC is a challenging determinant of biomass burning to quantify, being influenced by plant physiology and climatic conditions. This study offers a novel approach to meet this challenge, with two questions posed to assess its success: i) can fuel moisture content be satisfactorily estimated across the savannah landscapes of Africa using a land surface modelling approach; and ii) can this approach be enhanced by utilising data assimilation of satellite-derived LST.

To summarise the findings, it has been shown that a land surface model, such as JULES, is capable of successfully generating a daily record of FMC over large geographical regions, in this case the mixed tree/grass landscapes of Africa. These predictions were improved, in terms of the coefficient of determination, by utilising the assimilation technique developed in chapter 4; and a reduction of almost thirty percent in RMSE between modelled and *in situ* values was found with data assimilation. This method has advantages over traditional and remote sensing methods; an important one is the potential for a seamless delivery of predictions from the land surface model into a coupled fire model.

Although further validation may be warranted, this study provides sufficient evidence to suggest that biophysical modelling combined with satellite data represents a

viable option to adequately predict FMC over continental scales at high temporal resolution, and is thus a strong alternative to traditional methods. Improved fuel prediction can optimise the quantification of fire disturbance in the land surface models that play an integral role in reducing the uncertainty of the African carbon cycle and the associated feedbacks with the global climate system.

Chapter 6

Conclusions and further work

We are now in a position to review the gathered evidence in order to test the overarching research question. Conclusions will be summarised in relation to the scientific questions raised in each of the previous chapters, and general limitations of the research project will be addressed together with recommendations for further investigation. The contribution of this study to current scientific knowledge will also be reiterated.

6.1. Conclusions

The findings from **chapter 2**, which provided an evaluation of the biophysical processes and parameterisation of the JULES model for Africa, confirm the credibility of the model in simulating land surface processes relating to the terrestrial carbon cycle of the continent. Specifically, in answer to the questions posed earlier:

i) NPP magnitude, distribution, and IAV simulated by JULES were comparable with the other participating land surface models of the CAMIC project, and also with previously published estimates.

ii) ENSO is a primary driver of climate variability in Africa, with the associated variability in moisture and long-wave radiation explaining, for the most part, NPP variability.

iii) Monthly NPP growth rate was also significantly correlated to the growth rate in atmospheric CO_2 concentration. Although this finding may appear contrary to the overall downward trend in NPP over the 25-year modelling period, this can be consolidated by the fact that months with negative CO_2 anomalies are associated with larger negative NPP

anomalies than the contrasting situation for positive CO_2 anomalies. A note of caution though, is that atmospheric CO_2 growth rate anomalies are influenced by terrestrial carbon fluxes, which may be the primary cause of the correlation.

iv) Large NPP variability, in comparison to R_h variability, is primarily responsible for variability in NEP, and although Africa has fluctuated between a source and sink of carbon between 1982 and 2006, in the last few years of this period it has consistently behaved as a source of carbon.

In **chapter 3**, modelled estimates of LST were evaluated with respect to *in situ* measurements and retrievals from EO satellites. In the context of the questions posed earlier:

i) JULES LST displayed the largest uncertainty with respect to the measurements taken at the Skukuza field site, with evidence from this experiment indicating that both AATSR and SEVIRI are retrieving LST over a mixed tree/grass landscape within their respective target accuracies, whereas MODIS is not.

ii) For the continental intercomparison, findings indicate JULES LST was systematically underestimated with respect to AATSR and SEVIRI, which was most striking over barren or sparsely vegetated landscapes, although a re-parameterisation of its soil properties brought about a considerable reduction in this underestimation.

The development of a data assimilation scheme within the JULES model, as described in **chapter 4**, provided an opportunity to assess whether surface energy and water fluxes could be constrained by directly manipulating LST. To satisfy the two questions posed:

i) When sensible and latent heat fluxes derived with data assimilation were compared with corresponding Eddy Covariance measurements acquired from four African flux towers, RMSEs were less than the equivalent obtained without data assimilation.

ii) Simulations of soil moisture with data assimilation were more comparable with SSM data derived from ERS scatterometers for an area of strong land/atmosphere coupling in West Africa, than simulations without data assimilation, which implies open loop modelling was overestimating soil moisture in this region.

The investigation described in **chapter 5** provides satisfactory evidence to accept the premise that the combination of biophysical modelling and EO data represents a viable alternative to both traditional methods and remote sensing methods for predicting daily FMC at a continental scale. With respect to the two questions posed:

i) A daily record of FMC over the mixed tree/grass landscapes of Africa was generated by JULES in combination with MODIS NDVI data, with the temporal signatures of FMC consistent with the wet and dry seasonality of these regions, and where values were strongly correlated with field measurements acquired from three independent locations in the KNP.

ii) Predictions were improved with LST data assimilation than without, in terms of both the coefficient of determination and RMSE, with respect to the field measurements from the three independent locations in the KNP.

The overall research question which asks: "**can land-surface modelling accurately simulate land/atmosphere interactions in African savannahs given the highly heterogeneous nature of these landscapes?**" can now be answered, in the case

of the JULES model, with respect to the evidence described above. For instance, estimates of terrestrial carbon fluxes for Africa are comparable both with other land surface models and previously published values. In the case of LST, estimates are broadly comparable with both remotely sensed retrievals and *in situ* measurements. The application of a data assimilation scheme furthermore resulted in tangible improvements in heat fluxes and soil moisture with respect to independent data sources.

6.2. Contribution to knowledge

Firstly, an insight into the recent carbon balance of the African continent has been disseminated, whereby a strong correlation between NPP and ENSO was calculated for Africa. Indeed, the trajectories of NPP and R_h offer evidence that in recent years Africa has been acting as a source of carbon, and current trends suggest this situation may be more frequent in the future. This is a strong finding even though it pertains to a single land surface model, albeit a well established one. The carbon balance of Africa is highly uncertain (Williams *et al.*, 2007) even following the efforts of the CARBOAFRICA project (Bombelli *et al.*, 2009); the findings of this study can therefore significantly contribute to current thinking.

Secondly, this study offers a unique evaluation into the derivation of the surface energy balance as simulated by JULES, which includes a first attempt at comparing both model and satellite-derived LST with *in situ* measurements from an African savannah; and a first known integration of the EnKF into the JULES model, even though separately both model and assimilation scheme have been extensively used elsewhere. The principle purpose here was to better understand the dynamics of heat and water fluxes, and to investigate whether the integration of EO data would be beneficial in estimating key land/atmosphere interactions. It should not therefore be

viewed as a production-ready development, but does however offer the JULES management committee an outline for potential further development.

Finally, the production of a first known mapping over Africa of FMC - one the most important fuel components – is a significant contribution to the field of fire modelling; since optimisation in the derivation of fuel properties is a prerequisite for reducing the large uncertainty in biomass burning (van der Werf *et al.*, 2006). This contribution is particularly relevant if utilised in the future coupling of the JULES model to SPITFIRE.

In summary, this investigation represents an innovative approach to understanding key land surface processes in African savannahs in the framework of an important and established land surface model, affording an insight into some of the challenges in modelling these ecosystems. Indeed, with Africa being under-represented in climate modelling research, the findings presented here represent a significant contribution to the emerging literature on land/atmosphere interactions in African savannahs.

6.3. Research limitations and further work

Numerous assumptions and limitations with this study have been discussed in detail in the respective chapters with recommendations for further research; but a few general points are worth considering with regards to land surface modelling of African savannahs. For instance, most models neglect any disturbance regime, particularly herbivory. The JULES model however, is currently being developed by a community of modellers, whereby TRIFFID will be replaced by an Ecosystem Demography (ED) DGVM which will simulate succession in the context of size and age of PFTs since the most recent disturbance, and the aforementioned SPITFIRE fire model will be incorporated into a new ED-JULES-SPITFIRE amalgamation. A worthwhile exercise

then would be to re-examine the findings of this study under the new model framework; once it is available.

The majority of land surface models, JULES included, are limited in their representation of savannahs, since they are not designed to simulate horizontal heterogeneity beneath the woody canopies of these mixed tree/grass ecosystems. Micro-scale variations in carbon, water and heat fluxes are known to result from strong between-tree gradients in surface temperature, light availability and soil moisture (Caylor *et al.*, 2005). This complex array of factors determining the carbon allocation, hydrology, and radiative properties of savannahs can only comprehensively be modelled by representing fine-scale processes. Indeed, misrepresentation of these tree/grass dynamics in land surface models will amplify the uncertainty in simulating land/atmosphere interactions in these systems.

A current restriction to fine-scale sub-daily land surface modelling is the lack of available fine-scale precipitation data at sufficiently high temporal resolutions. A more realistic representation of savannahs, and a better understanding of their contribution to the African carbon balance, nevertheless remains crucial to accurately determining whether Africa is likely to be a mean source or sink of carbon in the future; despite the promising findings presented here. A focus on more representative processes, which account for the structure, function and distribution of trees and grass in African savannahs, thus remains a priority.

Bibliography

Aguado, I., Chuvieco, E., Boren, R., and Nieto, H., 2007. Estimation of dead fuel moisture content from meteorological data in Mediterranean areas. Applications in fire danger assessment. *International Journal of Wildland Fire,* **16**, 390-397.

Alo, C. A., and Wang, G. L., 2008. Potential future changes of the terrestrial ecosystem based on climate projections by eight general circulation models. *Journal of Geophysical Research-Biogeosciences,* **113**, G01004.

Alton, P., Mercado, L., and North, P., 2007a. A sensitivity analysis of the land-surface scheme JULES conducted for three forest biomes: Biophysical parameters, model processes, and meteorological driving data. *Global Biogeochemical Cycles,* **20**.

Alton, P. B., North, P. R., and Los, S. O., 2007b. The impact of diffuse sunlight on canopy light-use efficiency, gross photosynthetic product and net ecosystem exchange in three forest biomes. *Global Change Biology,* **13**, 776-787.

Andreae, M. O., and Merlet, P., 2001. Emission of trace gases and aerosols from biomass burning. *Global Biogeochemical Cycles,* **15**, 955-966.

Annan, J. D., Hargreaves, J. C., Edwards, N. R., and Marsh, R., 2005. Parameter estimation in an intermediate complexity Earth System Model using an ensemble Kalman filter. *Ocean Modelling,* **8**, 135–154.

Anyamba, A., Tucker, C. J., and Mahoney, R., 2002. From El Nino to La Nina: Vegetation response patterns over East and southern Africa during the 1997-2000 period. *Journal of Climate,* **15**, 3096-3103.

Archibald, S., Bond, W. J., Stock, W. D., and Fairbanks, D. H. K., 2005. Shaping the landscape: Fire-grazer interactions in an African savanna. *Ecological Applications,* **15**, 96-109.

Archibald, S., Nickless, A., Scholes, R. J., and Schulze, R., 2010. Methods to determine the impact of rainfall on fuels and burned area in southern African savannas. *International Journal of Wildland Fire,* **19**, 774-782.

Archibald, S., Roy, D. P., van Wilgen, B. W., and Scholes, R. J., 2009. What limits fire? An examination of drivers of burnt area in Southern Africa. *Global Change Biology,* **15**, 613-630.

Archibald, S., and Scholes, R. J., 2007. Leaf green-up in a semi-arid African savanna – separating tree and grass responses to environmental cues. *Journal of Vegetation Science,* **18**, 583-594.

Arora, V. K. and Boer, G. J., 2005. Fire as an interactive component of dynamic vegetation models. *Journal of Geophysical Research-Biogeosciences,* **110**, G02008.

Baldocchi, D., Falge, E., Gu, L. H., Olson, R., Hollinger, D., Running, S., Anthoni, P., Bernhofer, C., Davis, K., Evans, R., Fuentes, J., Goldstein, A., Katul, G., Law, B., Lee, X. H., Malhi, Y., Meyers, T., Munger, W., Oechel, W., Paw, K. T., Pilegaard, K., Schmid, H. P., Valentini, R., Verma, S., Vesala, T., Wilson, K., and Wofsy, S., 2001. FLUXNET: A new tool to study the temporal and spatial variability of ecosystem-scale carbon dioxide, water vapor, and energy flux densities. *Bulletin of the American Meteorological Society,* **82**, 2415– 2434.

Baldridge, A. M., Hook, S. J., Grove, C. I., and Rivera, G., 2009. The ASTER Spectral Library Version 2.0. *Remote Sensing of Environment*, **113**, 711-715.

Bartalis, Z., Scipal, K., and Wagner, W., 2006. Azimuthal anisotropy of scatterometer measurements over land. *IEEE Transactions on Geoscience and Remote Sensing*, **44**, 2083–2092.

Barton, J. M., Bristow, J. W., and Venter, F. J., 1986. A summary of the Precambrian Granitoid rocks of the Kruger National Park. *Koedoe*, **29**, 39-44.

Becker, F., and Li, Z. -L., 1990. Towards a local split-window method over land surfaces. *International Journal of Remote Sensing*, **11**, 369–394.

Biggs, R., Biggs, H. C., Dunne, T. T., Govender, N., and Potgieter, A.L.F., 2003. Experimental burn plot trial in the Kruger National Park: history, experimental design and suggestions for data analysis. *Koedoe*, **46**, 1–15.

Boden, T. A., Marland, G., and Andres, R. J. 2009. *Global, Regional, and National Fossil-Fuel CO2 Emissions.* Carbon Dioxide Information Analysis Center, Oak Ridge National Laboratory, U.S. Department of Energy, Oak Ridge, Tenn., U.S.A.

Bombelli, A., Henry, M., Castaldi, S., Adu-Bredu, S., Arneth, A., de Grandcourt, A., Grieco, E., Kutsch, W. L., Lehsten, V., Rasile, A., Reichstein, M., Tansey, K., Weber, U., and Valentini, R., 2009. An outlook on the Sub-Saharan Africa carbon balance. *Biogeosciences,* **6**, 2193-2205.

Bosilovich, M. G., 2006. A comparison of MODIS land surface temperature with in situ observations. *Geophysical Research Letters,* **33**, L20112.

Bosilovich, M. G., Radakovich, J. D., da Silva, A., Todling, R., and Verter, F., 2007. Skin temperature analysis and bias correction in a coupled land-atmosphere data assimilation system. *Journal of the Meteorological Society of Japan,* **85A**, 205-228.

Bowman, D. M. J. S., Balch, J. K., Artaxo, P., Bond, W. J., Carlson, J. M., Cochrane, M. A., D'Antonio, C. M., DeFries, R. S., Doyle, J. C., Harrison, S. P., Johnston, F. H., Keeley, J. E., Krawchuk, M. A., Kull, C. A., Marston, J. B., Moritz, M. A., Prentice, I. C., Roos, C. I., Scott, A. C., Swetnam, T. W., van der Werf, G. R., and Pyne, S. J., 2009. Fire in the Earth System. *Science,* **324**, 481-484.

Brutsaert, W., Hsu, A., and Schmugge, T. J., 1993. Parameterization of surface heat fluxes above forest with satellite thermal sensing and boundary-layer soundings. *Journal of Applied Meteorology,* **32**, 909–917.

Bucini, G., and Hanan, N. P., 2007. A continental-scale analysis of tree cover in African savannas. *Global Ecology and Biogeography,* **16**, 593–605.

Burgers, G., van Leeuwen, P. J., and Evensen, G., 1998. Analysis scheme in the ensemble Kalman Filter. *Monthly Weather Review,* **126**, 1719–1724.

Byrne, G. F., Begg, J. E., Fleming, P. M., and Dunin, F. X., 1979. Remotely sensed land cover temperature and soil-water status - brief review. *Remote Sensing of Environment*, **8**, 291-305.

Campbell, B., and Norman, J., 1998. *Environmental Biophysics.* Springer, New York.

Cao, M. K., Zhang, Q. F., and Shugart, H. H., 2001. Dynamic responses of African ecosystem carbon cycling to climate change. *Climate Research,* **17**, 183-193.

Caylor, K. K., Shugart, H. H., and Rodriguez-Iturbe, I., 2005. Tree Canopy Effects on Simulated Water Stress in Southern African Savannas. *Ecosystems,* **8**, 17–32.

Ceballos, A., Scipal, K., Wagner, W., and Martinez-Fernandez, J., 2005. Validation and downscaling of ERS Scatterometer derived soil moisture data over the central part of the Duero Basin, Spain. *Hydrological Processes*, **19**, 1549-1566.

Charney, J. G., Stone, P. H., and Quirk W. J., 1975. Drought in the Sahara: A biogeophysical feedback mechanism. *Science,* **187**, 434–435.

Chuvieco, E., Aguado, I., Cocero, D., and Riano, D., 2003. Design of an empirical index to estimate fuel moisture content from NOAA-AVHRR images in forest fire danger studies. *International Journal of Remote Sensing,* **24**, 1621-1637.

Chuvieco, E., Aguado, I., and Dimitrakopoulos, A. P., 2004a. Conversion of fuel moisture content values to ignition potential for integrated fire danger assessment. *Canadian Journal of Forest Research-Revue Canadienne De Recherche Forestiere,* **34**, 2284-2293.

Chuvieco, E., Cocero, D., Riano, D., Martin, P., Martinez-Vega, J., de la Riva, J. and Perez, F., 2004b. Combining NDVI and surface temperature for the estimation of live fuel moisture content in forest fire danger rating. *Remote Sensing of Environment,* **92**, 322-331.

Chuvieco, E., Riano, D., Aguado, I., and Cocero, D., 2002. Estimation of fuel moisture content from multitemporal analysis of Landsat Thematic Mapper reflectance data: applications in fire danger assessment. *International Journal of Remote Sensing,* **23**, 2145-2162.

Ciais, P., Piao, S. -L., Cadule, P., Friedlingstein, P., and Chedin, A., 2009. Variability and recent trends in the African terrestrial carbon balance. *Biogeosciences,* **6**, 1935-1948.

Clapp, R., and Hornberger, G., 1978. Empirical equations for some soil hydraulic properties. *Water Resources Research,* **14**, 601-604.

Cochrane, M. A., 2003. Fire science for rainforests. *Nature,* **421**, 913–919.

Coll, C., Caselles, V., Galve, J. M., Valor, E., Niclos, R., Sanchez, J. M., and Rivas, R., 2005. Ground measurements for the validation of land surface temperatures derived from AATSR and MODIS data. *Remote Sensing of Environment,* **97**, 288-300.

Coll, C., Caselles, V., Galve, J. M., Valor, E., Niclos, R., and Sanchez, J. M., 2006. Evaluation of split-window and dual-angle correction methods for land surface temperature retrieval from Envisat/Advanced Along Track Scanning Radiometer (AATSR) data. *Journal of Geophysical Research-Atmospheres*, **111**, D12105.

Collatz, G. J., Ball, J. T., Grivet, C., and Berry, J. A., 1991. Physiological and environmental-regulation of stomatal conductance, photosynthesis and transpiration - a model that includes a laminar boundary-layer. *Agricultural and Forest Meteorology,* **54**, 107-136.

Collatz, G. J., Ribas-Carbo, M., and Berry, J. A., 1992. Coupled photosynthesis-stomatal conductance model for leaves of C4 plants. *Australian Journal of Plant Physiology,* **19**, 519-538.

Cox, P. M. 2001. *Description of the TRIFFID Dynamic Global Vegetation Model. Technical Note 24.* Hadley Centre, Met Office, UK.

Cox, P. M., Betts, R. A., Bunton, C. B., Essery, R. L. H., Rowntree, P. R., and Smith, J., 1999. The impact of new land surface physics on the GCM simulation of climate and climate sensitivity. *Climate Dynamics*, **15**, 183-203.

Cox, P., Betts, R., Jones, C., Spall, S., and Totterdell I., 2000. Acceleration of global warming due to carbon-cycle feedbacks in a coupled climate model. *Nature*, **408**, 184–187.

Cramer, W., Bondeau, A., Woodward, F. I., Prentice, I. C., Betts, R. A., Brovkin, V., Cox, P. M., Fisher, V., Foley, J. A., Friend, A. D., Kucharik, C., Lomas, M. R., Ramankutty, N., Sitch, S., Smith, B., White, A., and Young-Molling, C., 2001. Global response of terrestrial ecosystem structure and function to CO2 and climate change: results from six dynamic global vegetation models. *Global Change Biology*, **7**, 357-373.

Cramer, W., Kicklighter, D. W., Bondeau, A., Moore, B., Churkina, C., Nemry, B., Ruimy, A., Schloss, A. L. and Participants Potsdam, N. P. P. M. I., 1999. Comparing global models of terrestrial net primary productivity (NPP): overview and key results. *Global Change Biology*, **5**, 1-15.

Crow, W. T., and Wood, E. F., 2003. The assimilation of remotely sensed soil brightness temperature imagery into a land surface model using Ensemble Kalman filtering: a case study based on ESTAR measurements during SGP97. *Advances in Water Resources*, **26**, 137-149.

Crow, W. T., and Zhan, X., 2007. Continental-scale evaluation of remotely sensed soil moisture products. *IEEE Geoscience and Remote Sensing Letters*, **4**, 451–455.

Daley, R., 1991. *Atmospheric data analysis*. Cambridge University Press , New York.

Dash, P., Gottsche, F. M., Olesen, F. S., and Fischer, H., 2002. Review article: Land surface temperature and emissivity estimation from passive sensor data: theory and practice - current trends. *International Journal of Remote Sensing*, **23**, 2563–2594.

Dee, D. P., and da Silva, A., 1998. Data assimilation in the presence of forecast bias. *Quarterly Journal of the Royal Meteorological Society*, **124**, 269–295.

de Rosnay, P., Drusch, M., Boone, A., Balsamo, G., Decharme, B., Harris, P., Kerr, Y., Pellarin, T., Polcher, J., and Wigneron, J. P., 2009. AMMA Land Surface Model Intercomparison Experiment coupled to the Community Microwave Emission Model: ALMIP-MEM, *Journal of Geophysical Research*, **114**, D05108.

Drake, B. G., GonzalezMeler, M. A., and Long, S. P., 1997. More efficient plants: A consequence of rising atmospheric CO2? *Annual Review of Plant Physiology and Plant Molecular Biology*, **48**, 609-639.

Drusch, M., Wood, E. F., and Gao, H., 2005. Observation operators for the direct assimilation of TRMM microwave imager retrieved soil moisture. *Geophysical Research Letters*, **32**, L15403.

Dunderdale, M., Muller, J. P., and Cox, P. M. 1999. Sensitivity of the Hadley Centre climate model to different earth observation and cartographically derived land surface data-sets. *The Contribution of POLDER and New Generation Spaceborne Sensors to Global Change Studies.* Meribel, France.

Essery, R. L. H., Best, M. J., Betts, R. A., Cox, P. M., and Taylor, C. M., 2003. Explicit representation of subgrid heterogeneity in a GCM land-surface scheme. *Journal of Hydrometeorology,* **4**, 530-545.

Essery, R. L. H., Best, M. J., and Cox, P. M. 2001. *MOSES 2.2 Technical Documentation. Technical Note 30.* Hadley Centre, Met Office, UK.

Evensen, G., 1994. Sequential data assimilation with a nonlinear quasi-geostrophic model using monte-carlo methods to forecast error statistics. *Journal of Geophysical Research-Oceans,* **99**, 10143-10162.

Evensen, G., 2003. The Ensemble Kalman Filter: theoretical formulation and practical implementation. *Ocean Dynamics,* **53**, 343-367.

Fang, J., Piao, S., Tang, Z., Peng, C. and Ji, W., 2001. Interannual variability in net primary production and precipitation. *Science,* **293**, 1723.

Fekete, B. M., Vorosmaty, C. J., Roads, J. O., and Willmott, C. J., 2004. Uncertainties in precipitation and their impacts on runoff estimates. *Jounal of Climate,* **17**, 294–304.

Field, C. B., Jackson, R. B. and Mooney, H. A., 1995. Stomatal responses to increased CO_2: implications from the plant to the global scale. *Plant, Cell and Environment,* **18**, 1214-1225.

Francey, R. J., Tans, P. P., Allison, C. E., Enting, I. G., White, J. W. C. and Trolier, M., 1995. Changes in oceanic and terrestrial carbon uptake since 1982. *Nature,* **373**, 326-330.

Friedlingstein, P., Bopp, L., Ciais, P., Dufresne, J. L., Fairhead, L., LeTreut, H., Monfray, P., and Orr, J., 2001. Positive feedback between future climate change and the carbon cycle. *Geophysical Research Letters,* **28**, 1543-1546.

Ge, J., Qi, J., and Lofgren, B., 2008. Use of vegetation properties from EOS observations for land-climate modeling in East Africa. *Journal of Geophysical Research-Atmospheres,* **113**, D15101.

Gelb, A., 1974. *Applied Optimal Estimation.* The MIT Press, Cambridge, MA.

Ghent, D., Balzter, H., and Kaduk, J., 2009. Assimilation of land-surface temperature in the land-surface model JULES, *in Proceedings of the RSPSoc 2009.* Leicester, 8–11 September 2009.

Ghent, D., Kaduk, J., Remedios, J., Ardo, J., and Balzter, H., 2010. Assimilation of land-surface temperature into the land surface model JULES with an Ensemble Kalman Filter. *Journal of Geophysical Research,* **115**, D19112.

Ghent, D., Kaduk, J., Remedios, J., and Balzter, H., (in press). Data assimilation into land-surface models: the implications for climate feedbacks. *International Journal of Remote Sensing*.

Global Soil Data Task, 2000. *Global Gridded Surfaces of Selected Soil Characteristics (IGBPDIS), International Geosphere-Biosphere Programme - Data and Information Services.* http://www.daac.ornl.gov/ ORNL Distributed Active Archive Center, Oak Ridge National Laboratory, Oak Ridge, Tennessee, U.S.A.

Govender, N., Trollope, W. S. W., and van Wilgen, B. W., 2006. The effect of fire season, fire frequency, rainfall and management on fire intensity in savanna vegetation in South Africa. *Journal of Applied Ecology*, **43**, 748-758.

Goward, S. N., Xue, Y., and Czajkowski, K. P., 2002. Evaluating land surface moisture conditions from the remotely sensed temperature/vegetation index measurements. An exploration with the simplified simple biosphere model. *Remote Sensing of Environment*, **79**, 225-242.

Hamill, T. M., Whitaker, J. S., and Snyder, C., 2001. Distance-dependent filtering of background error covariance estimates in an ensemble Kalman filter. *Monthly Weather Review*, **129**, 2776–2790.

Hao, X. J. and Qu, J. J., 2007. Retrieval of real-time live fuel moisture content using MODIS measurements. *Remote Sensing of Environment*, **108**, 130-137.

Hashimoto, H., Dungan, J. L., White, M. A., Yang, F., Michaelis, A. R., Running, S. W., and Nemani, R. R., 2008. Satellite-based estimation of surface vapor pressure deficits using MODIS land surface temperature data. *Remote Sensing of Environment,* **112**, 142-155.

Hashimoto, H., Nemani, R. R., White, M. A., Jolly, W. M., Piper, S. C., Keeling, C. D., Myneni, R. B., and Running, S. W., 2004. El Niño-Southern Oscillation-induced variability in terrestrial carbon cycling. *Journal of Geophysical Research,* **109**, D23110.

Hely, C., Bremond, L., Alleaume, S., Smith, B., Sykes, M. T. and Guiot, J., 2006. Sensitivity of African biomes to changes in the precipitation regime. *Global Ecology and Biogeography,* **15**, 258-270.

Hely, C., Dowty, P. R., Alleaume, S., Caylor, K. K., Korontzi, S., Swap, R. J., Shugart, H. H. and Justice, C. O., 2003. Regional fuel load for two climatically contrasting years in southern Africa. *Journal of Geophysical Research-Atmospheres,* **108**.

Hoffmann, W. A., Schroeder, W., and Jackson, R. B., 2002. Positive feedbacks of fire, climate, and vegetation and the conversion of tropical savanna. *Geophysical Research Letters,* **29**, 2052.

Houldcroft, C. J., Grey, W. M. F., Barnsley, M., Taylor, C. M., Los, S. O., and North, P. R. J., 2009. New vegetation albedo parameters and global fields of soil background albedo derived from MODIS for use in a climate model. *Journal of Hydrometeorology,* **10**, 183-198.

Houtekamer, P., and Mitchell, H., 2001. A sequential ensemble Kalman filter for atmospheric data assimilation. *Monthly Weather Review,* **129**, 123-137.

Huang, C. L., Li, X., and Lu., L., 2008. Retrieving soil temperature profile by assimilating MODIS LST products with ensemble Kalman filter. *Remote Sensing of Environment,* **112**, 1320-1336.

Hughes, J. K., Valdes, P. J., and Betts, R., 2006. Dynamics of a global-scale vegetation model. *Ecological Modelling,* **198**, 452-462.

Hulme, M., Doherty, R., Ngara, T., New, M., and Lister, D., 2001. African climate change: 1900-2100. *Climate Research,* **17**, 145-168.

Ichii, K., Hashimoto, H., Nemani, R., and White, M., 2005. Modeling the interannual variability and trends in gross and net primary productivity of tropical forests from 1982 to 1999. *Global and Planetary Change,* **48**, 274-286.

Intergovernmental Panel on Climate Change, 2007. *Climate Change 2007: Synthesis Report, Fourth Assessment Report of the Intergovernmental Panel on Climate Change.* Cambridge University Press, New York.

Jin, M., Dickinson, R. E., and Vogelmann, A. M., 1997. A comparison of CCM2-BATS skin temperature and surface-air temperature with satellite and surface observations. *Journal of Climate,* **10**, 1505-1524.

Kabsch, E., Olesen, F. S., and Prata, F., 2008. Initial results of the land surface temperature (LST) validation with the Evora, Portugal ground-truth station measurements. *International Journal of Remote Sensing*, **29**, 5329-5345.

Kalnay, E., Kanamitsu, M., Kistler, R., Collins, W., Deaven, D., Gandin, L., Iredell, M., Saha, S., White, G., Woollen, J., Zhu, Y., Chelliah, M., Ebisuzaki, W., Higgins, W., Janowiak, J., Mo, K. C., Ropelewski, C., Wang, J., Leetmaa, A., Reynolds, R., Jenne, R., and Joseph, D., 1996. The NCEP/NCAR 40-year reanalysis project. *Bulletin of the American Meteorological Society*, **77**, 437-471.

Keeley, J. E., and Rundel, P. W., 2003. Evolution of CAM and C_4 carbon-concentration mechanisms. *International Journal of Plant Sciences*, **164**, S55-S77.

Keeling, C. D., Whorf, T. P., Wahlen, M. and Vanderplicht, J., 1995. Interannual extremes in the rate of rise of atmospheric carbon-dioxide since 1980. *Nature*, **375**, 666-670.

Kerr, Y. H., Lagouarde, J. P., and Imbernon, J., 1992. Accurate land surface temperature retrieval from AVHRR data with use of an improved split window algorithm. *Remote Sensing of Environment*, **41**, 197-209.

Knorr, W., and Heimann, M., 2001. Uncertainties in global terrestrial biosphere modeling: 1. A comprehensive sensitivity analysis with a new photosynthesis and energy balance scheme. *Global Biogeochemical Cycles*, **15**, 207-225.

Kondratyev, K. Y., 1969. *Radiation in the Atmosphere*. New York Academic Press.

Koster, R. D., Dirmeyer, P., Guo, Z., Bonan, G., Chan, E., Cox, P., Gordon, C. T., Kanae, S., Kowalczyk, E., Lawrence, D., Liu, P., Lu, C.-H., Malyshev, S., McAvaney, B., Mitchell, K., Mocko, D., Oki, T., Oleson, K., Pitman, A., Sud, Y. C., Taylor, C. M., Verseghy, D., Vasic, R., Xue, Y., and Yamada, T., 2004. Regions of strong coupling between soil moisture and precipitation. *Science*, **305**, 1138–1140.

Krinner, G., Viovy, N., de Noblet-Ducoudre, N., Ogee, J., Polcher, J., Friedlingstein, P., Ciais, P., Sitch, S., and Prentice, I. C., 2005. A dynamic global vegetation model for studies of the coupled atmosphere-biosphere system. *Global Biogeochemical Cycles*, **19**, GB1015.

Kummerow, C., Barnes, W., Kozu, T., Shiue, J., and Simpson, J., 1998. The Tropical Rainfall Measuring Mission (TRMM) sensor package. *Journal of Atmospheric and Oceanic Technology*, **15**, 809-817.

Kustas, W. P., and Norman, J. M., 1996. Use of remote sensing for evapotranspiration monitoring over land surfaces. *Hydrological Sciences*, **41**, 495–515.

Kutsch, W. L., Hanan, N., Scholes, B., McHugh, I., Kubheka, W., Eckhardt, H., and Williams, C., 2008. Response of carbon fluxes to water relations in a savanna ecosystem in South Africa. *Biogeosciences,* **5**, 1797-1808.

Lehsten, V., Tansey, K., Balzter, H., Thonicke, K., Spessa, A., Weber, U., Smith, B., and Arneth, A., 2009. Estimating carbon emissions from African wildfires. *Biogeosciences,* **6**, 349–360.

Le Page, Y., Pereira, J. M. C., Trigo, R., Da Camara, C., Oom, D., and Mota, B., 2008. Global fire activity patters (1996-2006) and climatic influence: an analysis using the World Fire Atlas. *Atmospheric Chemistry and Physics,* **8**, 1911-1924.

Lewis, S. L., Lopez-Gonzalez, G., Sonke, B., Affum-Baffoe, K., Baker, T. R., Ojo, L. O., Phillips, O. L., Reitsma, J. M., White, L., Comiskey, J. A., Djuikouo, M. N., Ewango, C. E. N., Feldpausch, T. R., Hamilton, A. C., Gloor, M., Hart, T., Hladik, A., Lloyd, J., Lovett, J. C., Makana, J. R., Malhi, Y., Mbago, F. M., Ndangalasi, H. J., Peacock, J., Peh, K. S. H., Sheil, D., Sunderland, T., Swaine, M. D., Taplin, J., Taylor, D., Thomas, S. C., Votere, R., and Woll, H., 2009. Increasing carbon storage in intact African tropical forests. *Nature,* **457**, 1003-1006.

Li, F., Kustas, W. P., Prueger, J. H., Neale, C. M. U., and Jackson, T. J., 2005. Utility of remote sensing-based two-source energy balance model under low- and high-vegetation cover conditions. *Journal of Hydrometeorology*, **6**, 878-891.

Lillesand, T. M., and Kiefer, R. W., 1987. *Remote sensing and image interpretation*. Wiley, New York.

Llewellyn-Jones, D., Edwards, M. C., Mutlow, C. T., Birks, A. R., Barton, I. J., and Tait, H., 2001. *AATSR: Global-Change and Surface-Temperature Measurements from Envisat*. ESA bulletin February 2001, pp. 11–21.

Los, S. O., Weedon, G. P., North, P. R. J., Kaduk, J. D., Taylor, C. M., and Cox, P. M., 2006. An observation-based estimate of the strength of rainfall-vegetation interactions in the Sahel. *Geophysical Research Letters*, **33**, L16402.

Loveland, T. R., Reed, B. C., Brown, J. F., Ohlen, D. O., Zhu, J, Yang, L., and Merchant, J. W., 2001. Development of a Global Land Cover Characteristics Database and IGBP DISCover from 1-km AVHRR Data. *International Journal of Remote Sensing*, **21**, 1303-1330.

Low, A. B., and Rebelo, A. G. (eds), 1996. *Vegetation of South Africa, Lesotho and Swaziland*. Department of Environmental Affairs and Tourism, Pretoria, South Africa.

Madeira, C., Dash, P., Olesen, F., and Trigo, I. F., 2005. Intercomparison of Meteosat-8 derived LST with MODIS and AATSR similar products, *in Proceedings of the 2005 EUMETSAT Meteorological Satellite Conference.* Dubrovnik, Croatia, September 2005.

Margulis, S. A. and Entekhabi, D., 2003. Variational assimilation of radiometric surface temperature and reference-level micrometeorology into a model of the atmospheric boundary layer and land surface. *Monthly Weather Review*, **131**, 1272-1288.

McGuire, A. D., Melillo, J. M., Joyce, L. A., Kicklighter, D. W., Grace, A. L., Moore, B., and Vorosmarty, C. J., 1992. Interactions between carbon and nitrogen dynamics in estimating net primary productivity for potential vegetation in North America *Global Biogeochemical Cycles*, **6**, 101-124.

McGuire, A. D., Sitch, S., Clein, J. S., Dargaville, R., Esser, G., Foley, J., Heimann, M., Joos, F., Kaplan, J., Kicklighter, D. W., Meier, R. A., Melillo, J. M., Moore, B., Prentice, I. C., Ramankutty, N., Reichenau, T., Schloss, A., Tian, H., Williams, L. J., and Wittenberg, U., 2001. Carbon balance of the terrestrial biosphere in the twentieth century: Analyses of CO2, climate and land use effects with four process-based ecosystem models. *Global Biogeochemical Cycles*, **15**, 183-206.

McNally, A. P., Watt, P. D., Smith, J. A., Engelen, R., Kelly, G. A., Thepaut, J. N., and Matricardi, M., 2006. The assimilation of AIRS radiance data at ECMWF. *Quarterly Journal of the Royal Meteorological Society*, **132**, 935-957.

Melillo, J. M., McGuire, A. D., Kicklighter, D. W., Moore, B., Vorosmarty, C. J. and Schloss, A. L., 1993. Global climate-change and terrestrial net primary production. *Nature*, **363**, 234-240.

Mellilo., J. M., Steudler, P. A., Aber, J. D., Newkirk, K., Lux, H., Bowles, F. P., Catricala, C., Magill, A., Ahrens, T., and Morrisseau, S., 2002. Soil warming and carbon-cycle feedbacks to the climate system. *Science*, **298**, 2173-2176.

Mercado, L. M., Huntingford, C., Gash, J. H. C., Cox, P. M., and Jogireddy, V., 2007. Improving the representation of radiation interception and photosynthesis for climate model applications. *Tellus Series B-Chemical and Physical Meteorology*, **59**, 553-565.

Mitchell, T. D. and Jones, P. D., 2005. An improved method of constructing a database of monthly climate observations and associated high-resolution grids. *International Journal of Climatology*, **25**, 693-712.

Moran, M. S., and Jackson, R. D., 1991. Assessing the spatial-distribution of evapotranspiration using remotely sensed inputs. *Journal of Environmental Quality*, **20**, 725–737.

Naeimi, V., Scipal, K., Bartalis, Z., Hasenauer, S., and Wagner, W., 2009. An improved soil moisture retrieval algorithm for ERS and METOP scatterometer observations. *IEEE Transactions on Geoscience and Remote Sensing*, **47**, 1999-2013.

Nemani, R. R., Keeling, C. D., Hashimoto, H., Jolly, W. M., Piper, S. C., Tucker, C. J., Myneni, R. B. and Running, S. W., 2003. Climate-driven increases in global terrestrial net primary production from 1982 to 1999. *Science*, **300**, 1560-1563.

Nepstad, D. C., Verissimo, A., Alencar, A., Nobre, C., Lima, E., Lefebvre, P., Schlesinger, P., Potter, C., Moutinho, P., Mendoza, E., Cochrane, M., and Brooks, V., 1999. Large-scale impoverishment of Amazonian forests by logging and fire. *Nature,* **398**, 505-508.

Nicholson, S. E., and Kim, E., 1997. The relationship of the El Nino Southern oscillation to African rainfall. *International Journal of Climatology,* **17**, 117–135.

Nicholson, S. E., and Selato, J. C., 2000. The influence of La Nina on African rainfall. *International Journal of Climatology,* **20**, 1761-1776.

Norman, J. M., Kustas, W. P., and Humes, K. S., 1995. Source approach for estimating soil and vegetation energy fluxes in observations of directional radiometric surface temperature. *Agricultural and Forest Meteorology,* **77**, 263-293.

Notaro, M., 2008. Statistical identification of global hot spots in soil moisture feedbacks among IPCC AR4 models. *Journal of Geophysical Research-Atmospheres,* **113**, D09101.

Noyes, E., Good, S., Corlet, G., Kong, X., Remedios, J., and Llewellyn-Jones, D., 2006. AATSR LST product validation, *in Proceedings of the Second Working Meeting on MERIS and AATSR Calibration and Geophysical Validation (MAVT-2006).* ESRIN, Frascati, Italy.

Noyes, E., Soria, G., Sobrino, J. A., Remedios, J. J., Llewellyn-Jones, D. T., and Corlett, G. K., 2007. AATSR land surface temperature product algorithm verification over a WATERMED site. *Advances in Space Research,* **39***,* 171-178.

Papale, D., Reichstein, M., Aubinet, M., Canfora, E., Bernhofer, C., Kutsch, W., Longdoz, B., Rambal, S., Valentini, R., Vesala, T., and Yakir, D., 2006. Towards a standardized processing of Net Ecosystem Exchange measured with eddy covariance technique: algorithms and uncertainty estimation. *Biogeosciences,* **3**, 571-583.

Pellarin, T., Calvet, J. C., and Wagner, W., 2006. Evaluation of ERS scatterometer soil moisture products over a half degree region in southwestern France. *Geophysical Research Letters,* **33**, L17401

Peres, L. F., and DaCamara, C. C., 2005. Emissivity maps to retrieve land-surface temperature from MSG/SEVIRI. *IEEE Transactions on Geoscience and Remote Sensing*, **43**, 1834–1844.

Pinheiro, A. C. T., Mahoney, R., Privette, J. L., and Tucker, C. J., 2006a. Development of a daily long term record of NOAA-14 AVHRR land surface temperature over Africa. *Remote Sensing of Environment,* **103**, 153-164.

Pinheiro, A. C. T., Privette, J. L., and Guillevic, P., 2006b. Modeling the observed angular anisotropy of land surface temperature in a savanna. *IEEE Transactions on Geoscience and Remote Sensing*, **44**, 1036-1047.

Pinheiro, A. C. T., Privette, J. L., Mahoney, R., and Tucker, C. J., 2004. Directional effects in a daily AVHRR land surface temperature dataset over Africa. *IEEE Transactions on Geoscience and Remote Sensing*, **42**, 1941-1954.

Pipunic, R. C., Walker, J. P., and Western, A., 2008. Assimilation of remotely sensed data for improved latent and sensible heat flux prediction: A comparative synthetic study. *Remote Sensing of Environment*, **112**, 1295-1305.

Potter, C. S., 1999. Terrestrial biomass and the effects of deforestation on the global carbon cycle - Results from a model of primary production using satellite observations. *Bioscience*, **49**, 769-778.

Potter, C., Klooster, S., Myneni, R., Genovese, V., Tan, P.-N., and Kumar, V., 2003. Continental-scale comparisons of terrestrial carbon sinks estimated from satellite data and ecosystem modeling 1982–1998. *Global and Planetary Change*, **39**, 201-213.

Prata, A. J., 1993. Land surface temperature derived from the advanced very high resolution radiometer and the along-track scanning radiometer: 1. Theory. *Journal of Geophysical Research*, **98**, 16,689–16,702.

Prata, A. J., 1994. Land surface temperature derived from the advanced very high resolution radiometer and the along-track scanning radiometer: 2. Experimental results and validation of AVHRR algorithms. *Journal of Geophysical Research* **99**, 13,025–13,058.

Quaife, T., Lewis, P., De Kauwe, M., Williams, M., Law, B. E., Disney, M., and Bowyer, P., 2008. Assimilating canopy reflectance data into an ecosystem model with an Ensemble Kalman Filter. *Remote Sensing of Environment,* **112**, 1347-1364.

Raich, J. W., and Schlesinger, W. H., 1992. The global carbon dioxide flux in soil respiration and its relationship to vegetation and climate. *Tellus Series B-Chemical and Physical Meteorology,* **44**, 81-99.

Raich, J. W., Potter, C. S., and Bhagawati, D., 2002. Interannual variability in global soil respiration, 1980-94. *Global Change Biology,* **8**, 800-812.

Randerson, J. T., Chapin, F. S., Harden, J. W., Neff, J. C., and Harmon, M. E., 2002. Net ecosystem production: A comprehensive measure of net carbon accumulation by ecosystems. *Ecological Applications,* **12**, 937-947.

Rastetter, E. B., Williams, M., Griffin, K. L., Kwiatkowski, B. L., Tomasky, G., Potosnak, M. J., Stoy, P. C., Shaver, G. R., Stieglitz, M., Hobbie, J. E., and Kling, G. W., 2010. Processing arctic eddy-flux data using a simple carbon-exchange model embedded in the ensemble Kalman filter. *Ecological Applications,* **20**, 1285-1301.

Reichle, R. H., and Koster, R. D., 2003. Assessing the Impact of Horizontal Error Correlations in Background Fields on Soil Moisture Estimation. *Journal of Hydrometeorology,* **4**, 1229-1242.

Reichle, R. H., and Koster, R. D., 2004. Bias reduction in short records of satellite soil moisture. *Geophysical Research Letters*, **31**, L19501.

Reichle, R. H., Walker, J. P., Koster, R. D., and Houser, P. R., 2002. Extended versus ensemble Kalman filtering for land data assimilation. *Journal of Hydrometeorology*, **3**, 728-740.

Rhoads, J., Dubayah, R., Lettenmaier, D., O'Donnell, G., and Lakshmi, V., 2001. Validation of land surface models using satellite-derived surface temperature. *Journal of Geophysical Research*, **106**, 20,085–20,099.

Ridgwell, A., Hargreaves, J. C., Edwards, N. R., Annan, J. D., Lenton, T. M., Marsh, R., Yool, A., and Watson, A., 2007. Marine geochemical data assimilation in an efficient Earth System Model of global biogeochemical cycling. *Biogeosciences*, **4**, 87-104.

Rosenzweig, M. L., 1968. Net primary productivity of terrestrial communities: prediction from climatological data. *American Naturalist*, **102**, 67-74.

Roy, D. P., Boschetti, L., Justice, C. O., and Ju, J., 2008. The collection 5 MODIS burned area product – Global evaluation by comparison with the MODIS active fire product. *Remote Sensing of Environment*, **112**, 3690-3707.

Sandholt, I., Rasmussen, K., and Andersen, J., 2002. A simple interpretation of the surface temperature/vegetation index space for assessment of surface moisture status. *Remote Sensing of Environment*, **79**, 213-224.

Sankaran, M., Hanan, N. P., Scholes, R. J., Ratnam, J., Augustine, D. J., Cade, B. S., Gignoux, J., Higgins, S. I., Le Roux, X., Ludwig, F., Ardo, J., Banyikwa, F., Bronn, A., Bucini, G., Caylor, K. K., Coughenour, M. B., Diouf, A., Ekaya, W., Feral, C. J., February, E. C., Frost, P. G. H., Hiernaux, P., Hrabar, H., Metzger, K. L., Prins, H. H. T., Ringrose, S., Sea, W., Tews, J., Worden, J. and Zambatis, N., 2005. Determinants of woody cover in African Savannas. *Nature*, **438**, 846–849.

Sankaran, M., Ratnam, J., and Hanan, N., 2008. Woody cover in African savannas: the role of resources, fire and herbivory. *Global Ecology and Biogeography*, **17**, 236-245.

Schaadlich, S., Gottsche, F. M., and Olesen, F. S., 2001. Influence of land parameters and atmosphere on Meteosat brightness temperatures and generation of land surface temperature maps by temporally and spatially interpolating atmospheric correction. *Remote Sensing of Environment*, **75**, 39–46.

Schaphoff, S., Lucht, W., Gerten, D., Sitch, S., Cramer, W. and Prentice, I. C., 2006. Terrestrial biosphere carbon storage under alternative climate projections. *Climatic Change*, **74**, 97-122.

Schloss, A. L., Kicklighter, D. W., Kaduk, J., and Wittenberg, U., 1999. Comparing global models of terrestrial net primary productivity (NPP): comparison of NPP to climate and the Normalized Difference Vegetation Index (NDVI). *Global Change Biology,* **5**, 25-34.

Scholes, R. J., and Archer, S. R., 1997. Tree-grass interactions in savannas. *Annual Review of Ecology and Systematics,* **28**, 517-544.

Scholes, R. J., Gureja, N., Giannecchinni, M., Dovie, D., Wilson, B., Davidson, N., Piggott, K., McLoughlin, C., van der Velde, K., Freeman, A., Bradley, S., Smart, R., and Ndala, S., 2001. The environment and vegetation of the flux measurement site near Skukuza, Kruger National Park. *Koedoe,* **44**, 73-83.

Scholes, R. J., Ward, D. E., and Justice, C. O., 1996. Emissions of trace gases and aerosol particles due to vegetation burning in southern hemisphere Africa. *Journal of Geophysical Research-Atmospheres,* **101**, 23677-23682.

Schultz, M. G., Heil, A., Hoelzemann, J. J., Spessa, A., Thonicke, K., Goldammer, J. G., Held, A. C., Pereira, J. M. C., and van het Bolscher, M., 2008. Global wildland fire emissions from 1960 to 2000. *Global Biogeochemical Cycles,* **22**, GB2002.

Schulze, E. D., and Heimann, M., 1998. Carbon and water exchange of terrestrial ecosystems. In Galloway, J., and Melillo, J. M. (ed.) *Asian change in the context of global change.* Cambridge University Press, UK 145-161.

Sellers, P. J., Berry, J. A., Collatz, G. J., Field, C. B., and Hall, F. G., 1992. Canopy reflectance photosynthesis and transpiration, III. A reanalysis using enzyme kinetics — electron transport models of leaf physiology. *Remote Sensing of Environment,* **42**, 187-216.

Sellers, P. J., Dickinson, R. E., Randall, D. A., Betts, A. K., Hall, F. G., Berry, J. A., Collatz, G. J., Denning, A. S., Mooney, H. A., Nobre, C. A., Sato, N., Field, C. B., and Henderson-Sellers, A., 1997. Modeling the exchanges of energy, water, and carbon between continents and the atmosphere. *Science,* **275**, 502– 509.

Sellers, P. J., Mintz, Y., Sud, Y. C., and Dalcher, A., 1986. A simple biosphere model (SiB) for use within general circulation models. *Journal of the Atmospheric Sciences,* **43**, 505-531.

Seneviratne, S. I., Luthi, D., Litschi, M., and Schar, C., 2006. Land-atmosphere coupling and climate change in Europe. *Nature,* **443**, 205– 209

Shea, R. W., Shea, B. W., Kauffman, J. B., Ward, D. E., Haskins, C. I., and Scholes, M. C., 1996. Fuel biomass and consumption factors associated with fires in savanna ecosystems of South Africa and Zambia. *Journal of Geophysical Research*, **101**, 23551–23568.

Sheffield, J., Goteti, G., and Wood, E. F., 2006. Development of a 50-year high resolution global dataset of meteorological forcings for land surface modeling. *Journal of Climate,* **19**, 3088-3110.

Shukla, J. and Mintz, Y., 1982. Influence of land-surface evapotranspiration on the earth's climate, *Science*, **215**, 1498–1501.

Sims, D. A., Rahman, A. F., Cordova, V. D., El-Masri, B. Z., Baldocchi, D. D., Bolstad, P. V., Flanagan, L. B., Goldstein, A. H., Hollinger, D. Y., Misson, L., Monson, R. K., Oechel, W. C., Schmid, H. P., Wofsy, S. C., and Xu, L., 2008. A new model of gross primary productivity for North American ecosystems based solely on the enhanced vegetation index and land surface temperature from MODIS. *Remote Sensing of Environment*, **112**, 1633-1646.

Sitch, S., Smith, B., Prentice, I. C., Arneth, A., Bondeau, A., Cramer, W., Kaplan, J. O., Levis, S., Lucht, W., Sykes, M. T., Thonicke, K., and Venevsky, S., 2003. Evaluation of ecosystem dynamics, plant geography and terrestrial carbon cycling in the LPJ dynamic global vegetation model. *Global Change Biology*, **9**, 161-185.

Smith, B., Prentice, I. C., and Sykes, M. T., 2001. Representation of vegetation dynamics in the modelling of terrestrial ecosystems: comparing two contrasting approaches within European climate space. *Global Ecology and Biogeography*, **10**, 621-637.

Smith, R. N. B., Blyth, E. M., Finch, J. W., Goodchild, S., Hall, R. L., and Madry, S., 2006. Soil state and surface hydrology diagnosis based on MOSES in the Met Office Nimrod nowcasting system. *Meteorological Applications*, **13**, 89-109.

Snyder, R. L., Spano, D., Duce, P., Baldocchi, D., Xu, L. K., and Kyaw, T. P. U., 2006. A fuel dryness index for grassland fire-danger assessment. *Agricultural and Forest Meteorology*, **139**, 1-11.

Sobrino, J. A., El-Kharraz, J., and Li, Z. -L., 2003. Surface temperature and water vapour retrieval from MODIS data. *International Journal of Remote Sensing*, **24**, 5161−5182.

Sobrino, J. A., and Raissouni, N., 2000. Toward remote sensing methods for land cover dynamic monitoring: application to Morocco. *International Journal of Remote Sensing*, **21**, 353–366.

Sobrino, J. A., and Romaguera, M., 2004. Land surface temperature retrieval from MSG1-SEVIRI data. *Remote Sensing of Environment*, **92**, 247-254.

Soria G., and Sobrino, J. A., 2007. ENVISAT/AATSR derived land surface temperature over a heterogeneous region. *Remote Sensing of Environment*, **111**, 409-422.

Still, C. J., Berry, J. A., Collatz, G. J., and DeFries, R. S., 2003. Global distribution of C3 and C4 vegetation: Carbon cycle implications. *Global Biogeochemical Cycles*, **17**, 1006.

Sun, J., and Mahrt, L., 1995. Determination of surface fluxes from the surface radiative temperature. *Journal of Atmospheric Science*, **52**, 1096–1106.

Taylor, C. J. M., Harris, P. P., and Parker, D. J., 2010. Impact of soil moisture on the development of a Sahelian mesoscale convective system: A case-study from the AMMA Special Observing Period. *Quarterly Journal of the Royal Meteorological Society*, **136**, 456–470.

Tempel, P., Batjes, N. H., Collaty, G. J., and van Engelen, V. W. P. 1996. *IGBP-DIS soil data set for pedotransfer function development, Working paper and Reprint 96/05*. International Soil Reference and Information Centre (ISRIC), Wageningen.

Thonicke, K., Spessa, A., Prentice, I. C., Harrison, S. P., Dong, L., and Carmona-Moreno, C., 2010. The influence of vegetation, fire spread and fire behaviour on biomass burning and trace gas emissions: results from a process-based model. *Biogeosciences*, **7**, 1991-2011.

Thonicke, K., Venevsky, S., Sitch, S., and Cramer, W., 2001. The role of fire disturbance for global vegetation dynamics: coupling fire into a Dynamic Global Vegetation Model. *Global Ecology and Biogeography*, **10**, 661-677.

Trigo, I. F., Monteiro, I. T., Olesen, F., and Kabsch, E., 2008a. An assessment of remotely sensed land surface temperature. *Journal of Geophysical Research-Atmospheres*, **113**, 12.

Trigo, I. F., Peres, L. F., DaCarnara, C. C., and Freitas, S. C., 2008b. Thermal land surface emissivity retrieved from SEVIRI/meteosat. *IEEE Transactions on Geoscience and Remote Sensing*, **46**, 307-315.

Uppala, S. M., Kallberg, P. W., Simmons, A. J., Andrae, U., Bechtold, V. D., Fiorino, M., Gibson, J. K., Haseler, J., Hernandez, A., Kelly, G. A., Li, X., Onogi, K., Saarinen, S., Sokka, N., Allan, R. P., Andersson, E., Arpe, K., Balmaseda, M. A., Beljaars, A. C. M., Van De Berg, L., Bidlot, J., Bormann, N., Caires, S., Chevallier, F., Dethof, A., Dragosavac, M., Fisher, M., Fuentes, M., Hagemann, S., Holm, E., Hoskins, B. J., Isaksen, L., Janssen, P. A. E. M., Jenne, R., McNally, A. P., Mahfouf, J. F., Morcrette, J. J., Rayner, N. A., Saunders, R. W., Simon, P., Sterl, A., Trenberth, K. E., Untch, A., Vasiljevic, D., Viterbo, P., and Woollen, J., 2005. The ERA-40 re-analysis. *Quarterly Journal of the Royal Meteological Soc*iety, **131**, 2961−3012.

van der Werf, G. R., Randerson, J. T., Giglio, L., Collatz, G. J., Kasibhatla, P. S. and Arellano, A. F., 2006. Interannual variability in global biomass burning emissions from 1997 to 2004. *Atmospheric Chemistry and Physics*, **6**, 3423-3441.

van Wilgen, B. W., Govender, N., Biggs, H. C., Ntsala, D., and Funda, X. N., 2004. Response of Savanna fire regimes to changing fire-management policies in a large African National Park. *Conservation Biology*, **18**, 1533-1540.

Venevsky, S., Thonicke, K., Sitch, S., and Cramer, W., 2002. Simulating fire regimes in human-dominated ecosystems: Iberian Peninsula case study. *Global Change Biology*, **8**, 984-998.

Verbesselt, J., Jonsson, P., Lhermitte, S., van Aardt, J., and Coppin, P., 2006. Evaluating satellite and climate data-derived indices as fire risk indicators in savanna ecosystems. *IEEE Transactions on Geoscience and Remote Sensing*, **44**, 1622-1632.

Verbesselt, J., Somers, B., Lhermitte, S., Jonckheere, I., van Aardt, J., and Coppin, P., 2007. Monitoring herbaceous fuel moisture content with SPOT VEGETATION time-series for fire risk prediction in savanna ecosystems. *Remote Sensing of Environment*, **108**, 357-368.

Vivoy, N., Francois, C., Bondeau, A., Krinner, G., Polcher, J., Kergoat, L., Dedieu, G., De Noblet, N., Ciais, P., and Friedlingstein, P., 2001. Assimilation of remote sensing measurements into the ORCHIDEE/STOMATE DGVM biosphere model, *in Proceedings: 8th International Symposium Physical Measurements & Signatures in Remote Sensing*. Aussois, France.

Wagner, W., Lemoine, G., and Rott, H., 1999. A Method for Estimating Soil Moisture from ERS Scatterometer and Soil Data. *Remote Sensing of Environment*, **70**, 191-207.

Wagner, W., Scipal, K., Pathe, C., Gerten, D., Lucht, W., and Rudolf, B., 2003. Evaluation of the agreement between the first global remotely sensed soil moisture data with model and precipitation data. *Journal of Geophysical Research – Atmospheres*, **108**, 4611.

Wan, Z., 2008. New refinements and validation of the MODIS landsurface temperature/emissivity products. *Remote Sensing of Environment,* **112**, 59- 74.

Wan, Z., and Dozier, J., 1996. A generalized split-window algorithm for retrieving land surface temperature from space. *IEEE Transactions on Geoscience and Remote Sensing,* **34**, 892–905.

Wan, Z., Zhang, Y., Zhang, Y, Q., and Li, Z. L., 2002. Validation of the land-surface temperature products retrieved from Terra Moderate Resolution Imaging Spectroradiometer data. *Remote Sensing of Environment,* **83**, 163–180.

Wan, Z., Zhang, Y., Zhang, Y. Q., and Li, Z. L., 2004. Quality assessment and validation of the MODIS global land surface temperature. *International Journal of Remote Sensing*, **25**, 261- 274.

Weber, U., Jung, M., Reichstein, M., Beer, C., Braakhekke, M., Lehsten, V., Ghent, D., Kaduk, J., Viovy, N., Ciais, P., Gobron, N., and Rodenbeck, C., 2009. The inter-annual variability of Africa's ecosystem productivity: a multi-model analysis. *Biogeosciences,* **6**, 285-295.

Williams, C. A., Hanan, N. P., Baker, I., Collatz, G. J., Berry, J. A., and Denning, A. S., 2008. Interannual variability of photosynthesis across Africa and its attribution. *Journal of Geophysical Research-Atmospheres,* **113**, G04015.

Williams, C. A., Hanan, N. P., Neff, J. C., Scholes, R. J., Berry, J. A., Denning, A. S., and Baker, D. F., 2007. Africa and the global carbon cycle. *Carbon Balance Management,* **2**, 3.

Williams, M., Richardson, A. D., Reichstein, M., Stoy, P. C., Peylin, P., Verbeeck, H., Carvalhais, N., Jung, M., Hollinger, D. Y., Kattge, J., Leuning, R., Luo, Y., Tomelleri, E., Trudinger, C. M., and Wang, Y. P., 2009. Improving land surface models with FLUXNET data. *Biogeosciences*, **6**, 1341−1359.

Williams, M., Schwarz, P. A., Law, B. E., Irvine, J., and Kurpius, M. R., 2005. An improved analysis of forest carbon dynamics using data assimilation. *Global Change Biol*ogy, **11**, 89−105.

Wolter, K. and Timlin, M. S., 1998. Measuring the strength of ENSO events: How does 1997/1998 rank? *Weather,* **53**, 315-324.

Zeng, N., Neelin, J. D., Lau, W. K. M., and Tucker, C. J., 1999. Enhancement of interdecadal climate variability in the Sahel by vegetation interaction. *Science,* **286**, 1537–1540.

Zhang, J., Wang, W. C., and Wei, J., 2008. Assessing land-atmosphere coupling using soil moisture from the Global Land Data Assimilation System and observational precipitation. *Journal of Geophysical Research – Atmospheres,* **113**, D17119.